



Search for supersymmetry in pp collisions at $\sqrt{s} = 7$ TeV in events with a single lepton, jets, and missing transverse momentum

The CMS Collaboration*

Abstract

Results are reported from a search for new physics processes in events containing a single isolated high-transverse-momentum lepton (electron or muon), energetic jets, and large missing transverse momentum. The analysis is based on a 4.98 fb^{-1} sample of proton-proton collisions at a center-of-mass energy of 7 TeV, obtained with the CMS detector at the LHC. Three separate background estimation methods, each relying primarily on control samples in the data, are applied to a range of signal regions, providing complementary approaches for estimating the background yields. The observed yields are consistent with the predicted standard model backgrounds. The results are interpreted in terms of limits on the parameter space for the constrained minimal supersymmetric extension of the standard model, as well as on cross sections for simplified models, which provide a generic description of the production and decay of new particles in specific, topology based final states.

Submitted to the European Physical Journal C

1 Introduction

This paper reports results from an updated and improved search for new physics processes in proton-proton collisions at a center-of-mass energy of 7 TeV, focusing on the signature with a single isolated lepton (electron or muon), multiple energetic jets, and large missing momentum transverse to the beam direction (\cancel{E}_T). The data sample was collected by the Compact Muon Solenoid (CMS) experiment during 2011 at the Large Hadron Collider (LHC) and corresponds to an integrated luminosity of 4.98 fb^{-1} , roughly one hundred times larger than the sample used for our previous search [1].

The lepton + jets + \cancel{E}_T signature is prominent in models based on supersymmetry (SUSY) [2–7]. In R -parity-conserving models [8], SUSY particles are produced in pairs, and their decay chains end with the lightest supersymmetric particle (LSP). In some scenarios, the LSP is a neutralino ($\tilde{\chi}^0$), a heavy, electrically neutral, weakly interacting particle with the properties of a dark-matter candidate [9]. The presence of two such LSPs in each SUSY event typically leads to a large missing transverse momentum, depending on the details of the SUSY mass spectrum. The isolated lepton indicates a weak decay of a heavy particle, such as a W boson or a chargino ($\tilde{\chi}^\pm$). Multiple jets can be produced in complex decay chains of SUSY particles. This signature arises in many SUSY models, including the constrained minimal supersymmetric extension of the standard model (CMSSM) [10, 11], and in simplified models [12–15], which are based on simplified mass spectra and decays of new particles. Both of these frameworks are used to interpret the results. Searches in this or similar channels have been reported by CMS [1, 16] and ATLAS [17–19].

Searches for SUSY particles are complicated by the presence of standard model (SM) backgrounds that can share many of the features of signal events. In the single-lepton final state, backgrounds arise primarily from the production of $t\bar{t}$ and W +jets events, with smaller contributions from Z +jets, single-top quark production, and QCD multijet events. In the event topology studied here, a large observed value of \cancel{E}_T in a standard model event is usually genuine, resulting from the production of one or more high-momentum neutrinos. A smaller contribution to events in the high- \cancel{E}_T tail in this search can arise from the mismeasurement of jets in high cross section processes such as QCD multijet events. To determine the contributions from these backgrounds, we use methods that are primarily based on control samples in data, sometimes in conjunction with specific information from simulated event samples or from additional measurements that provide constraints on the background processes.

Three complementary methods are used to analyze the data, providing valuable cross-checks and probing different signal regions. The *Lepton Spectrum (LS) method* was used in the CMS single-lepton [1] and opposite-sign dilepton [20] SUSY searches performed using the 2010 data sample. It uses the observed lepton transverse momentum (p_T) spectrum and other control samples to predict the \cancel{E}_T distribution associated with the dominant SM backgrounds. This method is sensitive to SUSY models in which the \cancel{E}_T distribution is decoupled from the lepton p_T spectrum, as is the case when two undetected LSPs produce a large missing transverse momentum. The *Lepton-Projection Variable (L_P) method* uses the L_P variable, which was developed for the CMS measurement of the W polarization in W +jets events [21]. This variable, described in Section 6, is correlated with the helicity angle of the lepton in the W -boson rest frame. Both the L_P and the LS methods take advantage of well-understood properties of the W polarization in $t\bar{t}$ and W +jets events for the background determination. The methods are complementary in that they rely on significantly different approaches to determining the backgrounds, based on different kinematic variables and different signal regions. The *ANN method* uses an artificial neural network discriminant built from several kinematic quantities. The ANN discriminant is

then used in conjunction with \cancel{E}_T to define signal and sideband regions, from which the background yield is determined. A key variable in the ANN is M_T , an approximate invariant mass of the system comprising the lepton and the \cancel{E}_T , computed with the momentum components transverse to the beam direction. Background events usually have $M_T < M(W)$, where $M(W)$ is the W boson mass, because the observed \cancel{E}_T is associated with the neutrino from $W \rightarrow \ell\bar{\nu}$ decay.

This paper is organized as follows. Sections 2 and 3 describe the CMS detector and the event samples. The event preselection requirements that are common to all methods are discussed in Section 4. Sections 5, 6, and 7 describe the LS, L_P , and ANN methods, respectively, for obtaining SM background estimates from control samples in data. The observed yields in data are compared with the background estimate obtained for each method. Systematic uncertainties are described in Section 8. Finally, the results, interpretation, and conclusions of the analysis are presented in Sections 9 and 10.

2 The CMS detector

The CMS detector, described in detail in Ref. [22], is a multipurpose apparatus designed to study high- p_T physics processes in proton-proton collisions, as well as a broad range of phenomena in heavy-ion collisions. The central element of CMS is a 3.8 T superconducting solenoid, 13 m in length and 6 m in diameter. Within the magnet are (in order of increasing distance from the beam pipe) high-precision silicon pixel and silicon strip detectors for charged particle tracking; a lead-tungstate crystal electromagnetic calorimeter for measurements of photons, electrons, and the electromagnetic component of jets; and a hadron calorimeter, constructed from scintillating tiles and brass absorbers, for jet energy measurements. Beyond the magnet is the muon system, comprising drift tube, cathode strip, and resistive-plate detectors interleaved with steel absorbers. Most of the detector systems are divided into subsystems that cover the central (barrel) and forward (endcap) regions. The first level of the CMS trigger consists of custom hardware processors that use information from the calorimeter and the muon system to select up to 100 kHz of the most interesting events. These events are then analyzed in the High Level Trigger (HLT) processor farm, which uses information from all CMS detector systems to reduce the event rate to about 300 Hz.

In describing the angular distribution of particles and the acceptance of the detector, we frequently make use of the pseudorapidity, $\eta = -\ln[\tan(\theta/2)]$, where the polar angle θ of the particle's momentum vector is measured with respect to the z axis of the CMS coordinate system. The z axis points along the direction of the counterclockwise-moving proton beam; the azimuthal angle ϕ is measured in a plane perpendicular to this axis. The separation between two momentum vectors in η - ϕ space is characterized by the quantity $\Delta R = \sqrt{(\Delta\eta)^2 + (\Delta\phi)^2}$, which is approximately invariant under Lorentz boosts along the z axis.

3 Data and simulated event samples

The data samples used in the analysis were selected using triggers based on \cancel{E}_T , lepton p_T , and the transverse momenta (p_T^j) of the observed jets j . The overall level of jet activity was measured with the quantity $H_T^{\text{trigger}} = \sum_j p_T^j$, the scalar sum of jet transverse momenta satisfying $p_T^j > 40$ GeV. The missing transverse momentum $\cancel{E}_T^{\text{trigger}}$ was computed in the trigger using particle-flow algorithms [23, 24]. To maintain an acceptable trigger rate, the thresholds on $\cancel{E}_T^{\text{trigger}}$, lepton p_T , and H_T^{trigger} , were raised as the LHC luminosity increased over the course of

the data collection period. The highest thresholds applied in the muon trigger selection were $E_T^{\text{trigger}} > 50$ GeV, muon $p_T > 15$ GeV, and $H_T^{\text{trigger}} > 300$ GeV. For electron triggers, the highest thresholds applied were $E_T^{\text{trigger}} > 50$ GeV, electron $p_T > 15$ GeV and $H_T^{\text{trigger}} > 250$ GeV; a loose electron isolation requirement was also applied to help control the rate. The offline analysis requirements for both muon and electron events are more restrictive than those used in the trigger.

The analysis procedures are designed using simulated event samples. Except for certain scans of the SUSY parameter space discussed later, the detector simulation is performed using the GEANT4 package [25]. A variety of Monte Carlo (MC) event generators are used to model the backgrounds. The QCD multijet samples are generated with the PYTHIA 6.4.22 [26] MC generator with tune Z2 [27]. The dominant background, $t\bar{t}$, is studied with a sample generated using MADGRAPH 5.1.1.0 [28]. The W+jets and Z+jets processes are also simulated with MADGRAPH. Single-top (s -channel, t -channel, and tW) production is simulated with POWHEG [29]. To model the effect of multiple pp interactions per beam crossing (pileup), simulated events are generated with a nominal distribution of multiple vertices, then reweighted to match the distribution of the number of collision vertices per bunch crossing as measured in data.

Event samples for SUSY benchmark models are generated with PYTHIA. As example CMSSM scenarios, we use LM3 and LM6, which are among the standard benchmarks [30] used in CMS. The CMSSM benchmarks are described by the universal scalar mass parameter m_0 , the universal gaugino mass parameter $m_{1/2}$, the universal trilinear soft-SUSY-breaking parameter A_0 , the ratio of the two Higgs-doublet vacuum expectation values $\tan\beta$, and the sign of the Higgs mixing parameter μ . The LM3 (LM6) benchmark is described by $m_0 = 330$ GeV (85 GeV), $m_{1/2} = 240$ GeV (400 GeV), $A_0 = 0$ GeV (0 GeV), $\tan\beta = 20$ (10), and $\mu > 0$ (0). For LM3, the masses of the gluino and squarks are very similar (≈ 600 GeV), except for $m(\tilde{t}) \approx 440$ GeV, while the mass of the LSP is $m(\tilde{\chi}_1^0) = 94$ GeV. The LM6 spectrum is heavier, with $m(\tilde{g}) \approx 930$ GeV, $m(\tilde{q}) \approx 800$ GeV, $m(\tilde{t}) \approx 650$ GeV, and $m(\tilde{\chi}_1^0) \approx 160$ GeV. The next-to-leading-order (NLO) cross sections for these models are approximately 4.8 pb (LM3), and 0.4 pb (LM6).

The ANN method uses the LM0 model [30] to train the neural network. Because of its large cross section (54.9 pb at NLO), LM0 has already been excluded [1], but its kinematic distributions still provide a reasonably generic description of SUSY behavior with respect to the variables used in the neural network. The parameters for LM0 are $m_0 = 200$ GeV, $m_{1/2} = 160$ GeV, $A_0 = -400$ GeV, $\tan\beta = 10$, and $\mu > 0$.

The results are interpreted in two ways: (i) as constraints on CMSSM parameter space and (ii) as constraints on cross sections for event topologies described in the framework of simplified models. In both cases, a large number of simulated event samples are required to scan over the relevant space of model parameters. For this reason, the scans are performed with the CMS fast simulation package [31], which reduces the time associated with the detector simulation.

Both the LS and L_P background determination methods rely on knowledge of the W-boson polarization in W+jets and in $t\bar{t}$ events. The polarization effects are well modeled in simulated event samples, which are used in conjunction with control samples in data. The angular distribution of the (positively) charged lepton in the W^+ rest frame can be written as:

$$\frac{dN}{d\cos\theta_\ell^*} = f_{+1} \frac{3}{8} (1 + \cos\theta_\ell^*)^2 + f_{-1} \frac{3}{8} (1 - \cos\theta_\ell^*)^2 + f_0 \frac{3}{4} \sin^2\theta_\ell^*, \quad (1)$$

where f_{+1} , f_{-1} , and f_0 denote the polarization fractions associated with the W-boson helicities +1, -1, and 0, respectively. The angle θ_ℓ^* is the polar angle of the charged lepton in the W^+ rest frame, measured with respect to a z axis that is aligned with the momentum direction of

the W^+ in the top-quark rest frame. The polarization fractions thus determine the angular distribution of the lepton in the W rest frame and, together with the Lorentz boosts, control the p_T distributions of the lepton and the neutrino in the laboratory frame.

The W polarization fractions in top-quark decays have been calculated [32] with QCD corrections to next-to-next-to-leading order (NNLO), and the polarization is predominantly longitudinal. For $t \rightarrow bW^+$ these fractions are $f_0 = 0.687 \pm 0.005$, $f_{-1} = 0.311 \pm 0.005$, and $f_{+1} = 0.0017 \pm 0.0001$. These precise calculations reduce the uncertainties associated with the W polarization in $t\bar{t}$ events to a low level. The theoretical values are consistent with measurements from ATLAS [33], which obtained $f_0 = 0.67 \pm 0.03 \pm 0.06$, $f_{-1} = 0.32 \pm 0.02 \pm 0.03$, and $f_{+1} = 0.01 \pm 0.01 \pm 0.04$, expressed for the W^+ polarizations.

The W polarization in W +jets events exhibits a more complex behavior than that in $t\bar{t}$ production. Both CMS [21] and ATLAS [34] have reported measurements of these effects, which are consistent with ALPGEN [35] and MADGRAPH [28] simulations predicting that the W^+ and W^- bosons are both predominantly left-handed in W +jets events at high p_T . An NLO QCD calculation [36] has demonstrated that the predicted polarization fractions are stable with respect to QCD corrections. As discussed in later sections, this detailed knowledge of the W -boson polarization provides key information for measuring the SM backgrounds using control samples in data.

4 Event preselection

Table 1 summarizes the main variables and requirements used in the event preselection, which is designed to be simple and robust. Except where noted, a common set of preselection requirements is used by each of the three analysis methods. Events are required to have at least one good reconstructed primary vertex, at least three jets (L_P method and ANN method) or four jets (LS method), and exactly one isolated muon or exactly one isolated electron. These basic requirements select an event sample that is dominated by genuine, single-lepton events from SM processes.

The primary vertex must satisfy a set of quality requirements, including $|z_{PV}| < 24$ cm and $\rho_{PV} < 2$ cm, where z_{PV} and ρ_{PV} are the longitudinal and transverse distances of the primary vertex with respect to the nominal interaction point in the CMS detector.

Jets are reconstructed offline using the anti- k_T clustering algorithm [37] with a distance parameter of 0.5. The particle four-vectors reconstructed by the CMS particle-flow algorithm [23, 24], are used as inputs to the jet clustering algorithm. The particle-flow algorithm combines information from all CMS sub-detectors to provide a complete list of long-lived particles in the event. Corrections based on simulation are applied to the jet energies to establish a uniform response across the detector and a first approximation to the absolute energy scale [38]. Additional jet energy corrections are applied to the data using measurements of energy balance in dijet and photon + jet control samples in data. These additional corrections take into account residual differences between the jet energy scale in data and simulation. The effect of pileup was significant during much of the data-taking period. Extra energy clustered into jets due to pileup is taken into account with an event-by-event correction to the jet momentum four-vectors. Jet candidates are required to satisfy quality criteria that suppress noise and spurious energy deposits in the calorimeters. The performance of jet reconstruction and the corrections are described in Ref. [38]. In this analysis, reconstructed jets are required to satisfy $p_T > 40$ GeV and $|\eta| < 2.4$. The \cancel{E}_T vector is defined as the negative of the vector sum of the transverse momenta of all the particles reconstructed and identified by the particle-flow algorithm.

Table 1: Main preselection requirements. The term lepton designates either an electron or a muon. Definitions of the quantities and further details are given in the text.

Quantity	Requirement
Primary vertex position	$\rho_{PV} < 2 \text{ cm}, z_{PV} < 24 \text{ cm}$
Jet p_T threshold	$> 40 \text{ GeV}$
Jet η range	$ \eta < 2.4$
Number of jets	≥ 3 (L_P and ANN methods), ≥ 4 (LS method)
Lepton p_T threshold	$> 20 \text{ GeV}$
Muon η range	$ \eta < 2.1$
Muon isolation (relative)	< 0.10
Electron η range	$ \eta < 1.442, 1.56 < \eta < 2.4$
Electron isolation (relative)	< 0.07 (barrel) < 0.06 (endcaps)
Lepton p_T thresh. for veto	$> 15 \text{ GeV}$

In the muon channel, the preselection requires a single muon candidate [39] satisfying $p_T(\mu) > 20 \text{ GeV}$ and $|\eta| < 2.1$. Several requirements are imposed on the elements that form the muon candidate. The reconstructed track must satisfy quality criteria related to the number of hits in the pixel, strip, and muon detectors, and it must have an impact parameter d_0 in the transverse plane with respect to the beam spot satisfying $|d_0| < 0.02 \text{ cm}$ and an impact parameter d_z with respect to the primary vertex along the z direction satisfying $|d_z| < 1.0 \text{ cm}$.

To suppress background in which the muon originates from a semileptonic decay of a hadron containing a bottom or charm quark, we require that the muon candidate be spatially isolated from other energy in the event. A cone of size $\Delta R = 0.3$ is constructed around the initial muon momentum direction in η - ϕ space. The muon combined isolation variable, $I^{\text{comb}} = \sum_{\Delta R < 0.3} (E_T + p_T)$, is defined as the sum of the transverse energy E_T (as measured in the electromagnetic and hadron calorimeters) and the transverse momentum p_T (as measured in the silicon tracker) of all reconstructed objects within this cone, excluding the muon. This quantity is used to compute the combined isolation relative to the muon transverse momentum, $I_{\text{rel}}^{\text{comb}} = I^{\text{comb}} / p_T(\mu)$, which is required to satisfy $I_{\text{rel}}^{\text{comb}} < 0.1$.

Electron candidates [40] are reconstructed by matching energy clusters in the ECAL with tracks in the silicon tracking system. Candidates must satisfy $p_T > 20 \text{ GeV}$ and $|\eta| < 2.4$, excluding the barrel-endcap transition region ($1.442 < |\eta| < 1.56$). Quality and photon-conversion rejection requirements are also imposed. The relative isolation variable, defined in a manner similar to that in the muon channel, must satisfy $I_{\text{rel}}^{\text{comb}} < 0.07$ in the barrel region and $I_{\text{rel}}^{\text{comb}} < 0.06$ in the endcaps. The requirements on d_0 and d_z are the same as those used in the muon channel.

The preselection requirements have a large effect on the sample composition. The lepton isolation requirement is critical for the rejection of QCD multijet processes, which have very large cross sections but are reduced to a low level by the isolation and the other preselection requirements. While many lepton candidates are produced in the semileptonic decays of hadrons containing b or c quarks, from π and K decays in flight, and from misidentification of hadrons, the vast majority of these candidates are either within or near hadronic jets. The background from W +jets events (primarily from $W \rightarrow e\nu$ or $W \rightarrow \mu\nu$, but also $W \rightarrow \tau\nu$) is initially also very large. This contribution is heavily suppressed by the three- or four-jet requirement. Depending on the particular signal region, either $t\bar{t}$ or W +jets production emerges as the largest contribution to the background in the sample of events with moderate to large \cancel{E}_T .

Events with a second isolated-lepton candidate satisfying the criteria listed in Table 1 are vetoed. This requirement not only suppresses SM background, but also minimizes the statistical overlap between the event sample used in this search and those used in multilepton searches. However, $t\bar{t}$ events with dileptons can still be present, and this contribution must be determined, particularly because the presence of two neutrinos in the decay chains can result in large values of \cancel{E}_T . The background involving $W \rightarrow \tau\nu$ decays, both from $t\bar{t}$ events and from direct W production, must also be determined. To help suppress the dilepton background, the requirements on the veto leptons are somewhat looser than those on the signal lepton. For both muons and electrons, the p_T threshold is $p_T > 15$ GeV, the isolation requirement is $I_{\text{rel}}^{\text{comb}} < 0.15$, and the impact parameter requirement is $|d_0| < 0.1$ cm (the d_z requirement is kept the same as for the signal lepton). In addition, some of the quality requirements for both the muon and electron are loosened.

Further event selection requirements are used in the individual background estimation methods described in Sections 5, 6, and 7. The methods use the quantity H_T , which is defined as the scalar sum of the transverse momenta of particle-flow jets j with $p_T^j > 40$ GeV and $|\eta^j| < 2.4$,

$$H_T = \sum_j p_T^j. \quad (2)$$

The three background determination methods presented in the following three sections use different approaches to estimating the SM backgrounds using control samples in data. In Section 9, we compare the results of the different methods and make some observations about their features.

5 Lepton Spectrum method

5.1 Overview of the Lepton Spectrum method

This section describes the Lepton Spectrum (LS) method, which is named for the technique used to determine the dominant background source: genuine, single-lepton processes. Such processes account for about 75% of the total SM background in the signal regions and arise primarily from $t\bar{t}$, single-top, and W +jets events. Their contribution to the \cancel{E}_T distribution is estimated by exploiting the fact that, when the lepton is produced in W -boson decay, the \cancel{E}_T distribution is fundamentally related to the lepton p_T spectrum, unlike the \cancel{E}_T for many SUSY models. A more detailed description of the Lepton Spectrum method is given in the references [1, 41].

Non-single-lepton backgrounds are also determined using control samples in the data. Such events arise mainly from (i) $t\bar{t}$ dilepton events, in which zero, one, or both of the leptons is a τ and (ii) $t\bar{t}$ and W +jets events with a single $\tau \rightarrow (\mu, e)$ decay. Background from QCD multijet events is expected from simulation to be very small. However, the uncertainties in such simulations are difficult to quantify, because the QCD multijet background in the phase space relevant to this analysis arises from extreme tails of processes with very large cross sections. We therefore use control samples in data to measure the QCD multijet background. Simulated event samples are used for the determination of the Z +jets contribution, which is estimated with sufficient precision to be below one event for most of the signal regions.

The signal regions are defined with three thresholds in H_T ($H_T \geq 500$ GeV, $H_T \geq 750$ GeV, and $H_T \geq 1000$ GeV) and four bins in \cancel{E}_T ($250 \leq \cancel{E}_T < 350$ GeV, $350 \leq \cancel{E}_T < 450$ GeV, $450 \leq \cancel{E}_T < 550$ GeV, and $\cancel{E}_T > 550$ GeV).

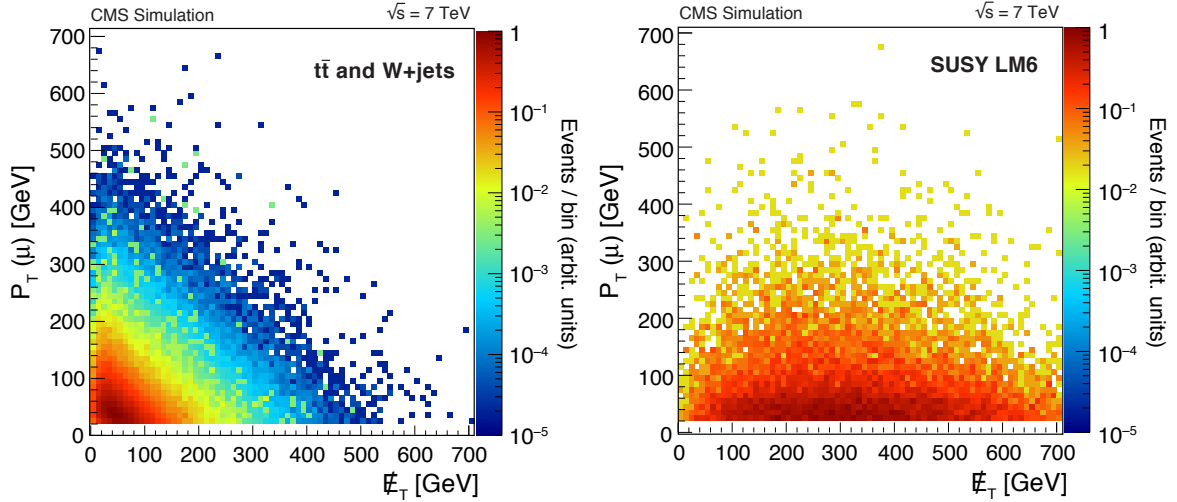


Figure 1: Distributions of muon p_T vs. E_T in the μ channel for simulated $t\bar{t}$ and W +jets events (left) and for the LM6 SUSY benchmark model (right).

5.2 Estimation of single-lepton backgrounds

The physical foundation of the Lepton Spectrum method is that, when the lepton and neutrino are produced together in two-body W decay (either in $t\bar{t}$ or in W +jets events), the lepton p_T spectrum is directly related to the E_T spectrum. The lepton and the neutrino share a common Lorentz boost from the W rest frame to the laboratory frame. As a consequence, the lepton spectrum reflects the p_T distribution of the W , regardless of whether the lepton was produced in a top-quark decay or in a W +jets event. With suitable corrections, discussed below, the lepton p_T spectrum can therefore be used to predict the E_T spectrum for SM single-lepton backgrounds.

The E_T distribution in many SUSY models is dominated by the presence of two LSPs. In contrast to the SM backgrounds, the E_T and lepton p_T distributions in SUSY processes are therefore nearly decoupled. The E_T distribution for such models extends to far higher values than the lepton spectrum. Figure 1 shows the relationship between the lepton- p_T and E_T distributions in the laboratory frame for two simulated event samples: (i) the predicted SM mixture of $t\bar{t}$ and W +jets events and (ii) the SUSY LM6 benchmark model. When taken from data, the upper-left region in Fig. 1 (left) provides the key control sample of high- p_T leptons from SM processes. This region typically has very little contamination from SUSY events, which populate the high- E_T region but have relatively low lepton p_T values.

The lepton p_T spectrum is measured with a muon control sample defined by the preselection criteria and the H_T requirements. Unlike the signal region, no E_T requirement is applied, because even a modest one ($E_T > 25$ GeV) would bias the high end of the lepton p_T spectrum, which is critical for making the background prediction. Only muon events are used as a control sample, because the QCD multijet background is significant in the low- E_T region of the electron sample. The number of events that are common to both the control sample and the signal region is small. For example, the overlap as measured in simulated $t\bar{t}$ events is 3.6% for $H_T \geq 750$ GeV, $E_T \geq 250$ GeV, and $p_T \geq 250$ GeV. Because no E_T requirement is placed on the muon control sample, a small amount of QCD background remains and must be measured and subtracted. The scaling from the muon to the electron samples is obtained by fitting their ratio in the data over the range $60 \leq E_T \leq 250$ GeV, with systematic uncertainties evaluated by varying the fit range. The resulting correction factor is $N(e)/N(\mu) = 0.88 \pm 0.03 \pm 0.03$, where the uncertainties are statistical and systematic, respectively.

To use the lepton spectrum to predict the \cancel{E}_T spectrum in single-lepton SM background processes, three main issues must be understood: (i) the effect of the W -boson polarization in both $t\bar{t}$ and W +jets events, (ii) the effect of the applied lepton p_T threshold, and (iii) the difference between the experimental resolutions on the measurements of lepton p_T and \cancel{E}_T .

The status of theoretical and experimental knowledge of W -boson polarization in $t\bar{t}$ and in W +jets events is discussed in Section 3. The helicity zero polarization state results in a forward-backward symmetric angular distribution of the lepton and the neutrino in the W rest frame (with respect to the W momentum direction), leading to identical lepton and neutrino spectra in the laboratory frame. In contrast, the helicity ± 1 states result in angular asymmetries that lead to somewhat different lepton and neutrino p_T spectra in the laboratory frame. These effects are taken into account by applying correction factors obtained from simulation to the measured lepton spectrum, with uncertainties as described in Section 8.

The second key issue in the Lepton Spectrum method is the effect of the threshold ($p_T > 20$ GeV) applied to the leptons in both the signal and control samples. Because of the anti-correlation between the lepton p_T and the \cancel{E}_T arising from non-zero W -boson helicity states, the threshold requirement removes SM background events in the high- \cancel{E}_T signal region but not the events in the control sample with high- p_T muons that are used to predict the high tail of the \cancel{E}_T spectrum. For the $t\bar{t}$ background, this effect partially compensates for the bias from the W polarization. For W +jets events, in contrast, the polarization effects for W^+ and W^- approximately cancel, but the lepton p_T threshold shifts the predicted yield upward. Correction factors from simulation are used to account for these effects (as well as for polarization effects), which are well defined and understood.

Finally, the resolution on the reconstructed \cancel{E}_T is poorer than that for the lepton p_T , so the \cancel{E}_T spectrum is somewhat broadened with respect to the prediction from the lepton spectrum. We measure \cancel{E}_T resolution functions in the data using QCD multijet events obtained with a set of single-jet triggers spanning the range from $E_T \geq 30$ GeV to $E_T \geq 370$ GeV. These resolution functions, or templates, quantify the \cancel{E}_T resolution as a function of the number of jets and the H_T of the event. These templates are used to smear the measured lepton momenta. Because the templates are taken from data, they include not only the intrinsic detector resolutions, but also acceptance effects. The overall effect of the smearing is modest, changing the background prediction by 5–15%, depending on the \cancel{E}_T threshold applied.

The raw background predictions for the single-lepton background are corrected to account for the effects described above, as well as for the small contamination of the single-lepton control sample arising from dilepton and single- τ events with high- p_T leptons. These backgrounds are measured separately, as described below. The overall correction factor is defined such that the single-lepton prediction in a given signal region in simulation matches the yield from single-lepton processes.

The predicted single-lepton background yield varies from about 150 events for the signal region with $250 \leq \cancel{E}_T < 350$ GeV and $H_T \geq 500$ GeV to about 3 events for the region with $\cancel{E}_T \geq 550$ GeV and $H_T \geq 1000$ GeV. These predictions, as well as the expectations from simulation, are presented in Tables 2, 3, and 4 and discussed in more detail in Section 5.4.

5.3 Estimation of non-single-lepton backgrounds

The non-single-lepton backgrounds include dilepton events in several categories, events with $W \rightarrow \tau\nu$ followed by $\tau \rightarrow \ell$ decays (in either $t\bar{t}$ or W +jets events), and QCD multijet processes. These subdominant backgrounds are estimated using control samples in data, in conjunction

Table 2: Event yields for the Lepton Spectrum method for $H_T \geq 500$ GeV. The upper part of the table gives the background predictions that are based on simulated (MC) event samples and the yield for the SUSY signal points LM3 and LM6. The lower part gives the backgrounds predicted using control samples in the data (data-driven prediction). The actual yield observed in data is given at the bottom, with the separate muon and electron yields given in parentheses (N_μ, N_e) after the total yield. The uncertainties on the background predictions are statistical and systematic. The MC yields are not used in setting limits and are included only for reference. The uncertainties on the MC yields are statistical only.

\cancel{E}_T range [GeV]	[250, 350)	[350, 450)	[450, 550)	≥ 550
MC yields				
1 ℓ	146.7 ± 2.1	34.8 ± 1.1	8.5 ± 0.6	2.9 ± 0.3
Dilepton	19.9 ± 0.5	3.8 ± 0.2	0.7 ± 0.1	0.3 ± 0.1
1 τ	30.6 ± 0.9	7.9 ± 0.5	2.1 ± 0.3	0.8 ± 0.2
Z+jets	1.3 ± 0.8	< 0.1	< 0.1	< 0.1
Total (MC)	198.6 ± 2.5	46.5 ± 1.2	11.3 ± 0.6	4.0 ± 0.4
SUSY LM3 (MC)	266.3 ± 3.7	91.0 ± 2.2	23.3 ± 1.1	9.9 ± 0.7
SUSY LM6 (MC)	23.4 ± 0.3	20.0 ± 0.3	13.4 ± 0.2	10.8 ± 0.2
Data-driven prediction				
1 ℓ	$109 \pm 13 \pm 18$	$32.0 \pm 7.5 \pm 5.8$	$3.9 \pm 2.7 \pm 1.2$	$3.1 \pm 2.3 \pm 1.0$
Dilepton	$15.8 \pm 1.9 \pm 1.8$	$3.0 \pm 0.9 \pm 0.5$	$0.5 \pm 0.3 \pm 0.2$	$0.1 \pm 0.2 \pm 0.2$
1 τ	$33.0 \pm 1.8 \pm 1.7$	$8.9 \pm 1.0 \pm 0.5$	$2.1 \pm 0.5 \pm 0.2$	$1.1 \pm 0.3 \pm 0.2$
QCD	$0.0 \pm 1.0 \pm 1.2$	$0.0 \pm 1.0 \pm 1.2$	$0.0 \pm 1.0 \pm 1.2$	$0.0 \pm 1.0 \pm 1.2$
Z+jets (MC)	$1.3 \pm 0.8 \pm 1.3$	< 0.1	< 0.1	< 0.1
Total (predicted)	$159 \pm 14 \pm 18$	$44.0 \pm 7.7 \pm 6.0$	$6.6 \pm 2.9 \pm 1.7$	$4.3 \pm 2.6 \pm 1.6$
Data (observed)	163 (84, 79)	46 (21, 25)	9 (8, 1)	2 (1, 1)

Table 3: Event yields for the Lepton Spectrum method for $H_T \geq 750$ GeV. Further details are given in the Table 2 caption.

\cancel{E}_T range [GeV]	[250, 350)	[350, 450)	[450, 550)	≥ 550
MC yield				
1 ℓ	47.3 ± 1.2	14.9 ± 0.7	5.4 ± 0.4	2.7 ± 0.3
Dilepton	8.2 ± 0.4	2.3 ± 0.2	0.6 ± 0.1	0.3 ± 0.1
1 τ	9.2 ± 0.5	3.0 ± 0.3	1.2 ± 0.2	0.7 ± 0.2
Z+jets	0.7 ± 0.6	< 0.1	< 0.1	< 0.1
Total (MC)	65.4 ± 1.5	20.2 ± 0.8	7.2 ± 0.5	3.6 ± 0.4
SUSY LM3 (MC)	114.6 ± 2.5	47.1 ± 1.6	16.1 ± 0.9	8.6 ± 0.7
SUSY LM6 (MC)	14.9 ± 0.3	13.8 ± 0.2	10.3 ± 0.2	9.8 ± 0.2
Data-driven prediction				
1 ℓ	$41.7 \pm 8.7 \pm 5.4$	$11.7 \pm 5.0 \pm 1.9$	$2.6 \pm 2.3 \pm 0.6$	$3.1 \pm 2.4 \pm 0.8$
Dilepton	$5.9 \pm 1.1 \pm 0.7$	$1.3 \pm 0.5 \pm 0.2$	$0.5 \pm 0.2 \pm 0.1$	$0.1 \pm 0.1 \pm 0.3$
1 τ	$9.6 \pm 0.9 \pm 0.6$	$3.1 \pm 0.6 \pm 0.3$	$1.1 \pm 0.3 \pm 0.2$	$0.8 \pm 0.2 \pm 0.1$
QCD	$0.0 \pm 0.2 \pm 0.4$	$0.0 \pm 0.2 \pm 0.4$	$0.0 \pm 0.2 \pm 0.4$	$0.0 \pm 0.2 \pm 0.4$
Z+jets (MC)	$0.7 \pm 0.6 \pm 0.7$	< 0.1	< 0.1	< 0.1
Total (predicted)	$57.9 \pm 8.9 \pm 5.6$	$16.2 \pm 5.0 \pm 2.0$	$4.2 \pm 2.4 \pm 0.8$	$4.0 \pm 2.4 \pm 1.0$
Data (observed)	48 (27, 21)	16 (7, 9)	5 (4, 1)	2 (1, 1)

Table 4: Event yields for the Lepton Spectrum method for $H_T > 1000$ GeV. Further details are given in the Table 2 caption.

\cancel{E}_T range [GeV]	[250, 350)	[350, 450)	[450, 550)	≥ 550
MC yield				
1 ℓ	13.4 ± 0.6	4.8 ± 0.4	2.1 ± 0.3	1.3 ± 0.2
Dilepton	2.7 ± 0.2	1.0 ± 0.1	0.3 ± 0.1	0.2 ± 0.1
1 τ	2.1 ± 0.2	0.7 ± 0.1	0.5 ± 0.1	0.4 ± 0.1
Z+jets	0.5 ± 0.5	< 0.1	< 0.1	< 0.1
Total (MC)	18.8 ± 0.9	6.4 ± 0.5	2.9 ± 0.3	1.9 ± 0.2
SUSY LM3 (MC)	38.1 ± 1.4	18.3 ± 1.0	7.0 ± 0.6	5.5 ± 0.5
SUSY LM6 (MC)	7.0 ± 0.2	6.0 ± 0.2	4.6 ± 0.1	5.2 ± 0.2
Data-driven prediction				
1 ℓ	$11.7 \pm 4.6 \pm 1.8$	$5.5 \pm 3.6 \pm 1.0$	$2.0 \pm 2.2 \pm 0.6$	$3.1 \pm 2.3 \pm 1.0$
Dilepton	$1.2 \pm 0.6 \pm 0.1$	$0.4 \pm 0.4 \pm 0.1$	$0.2 \pm 0.2 \pm 0.1$	$0.1 \pm 0.2 \pm 0.2$
1 τ	$3.0 \pm 0.5 \pm 0.5$	$0.9 \pm 0.3 \pm 0.2$	$0.4 \pm 0.2 \pm 0.2$	$0.8 \pm 0.2 \pm 0.2$
QCD	$0.0 \pm 0.1 \pm 0.1$	$0.0 \pm 0.1 \pm 0.1$	$0.0 \pm 0.1 \pm 0.1$	$0.0 \pm 0.1 \pm 0.1$
Z+jets (MC)	$0.5 \pm 0.5 \pm 0.5$	< 0.1	< 0.1	< 0.1
Total (predicted)	$16.4 \pm 4.7 \pm 1.9$	$6.8 \pm 3.6 \pm 1.0$	$2.6 \pm 2.2 \pm 0.6$	$4.0 \pm 2.4 \pm 1.0$
Data (observed)	14 (7, 7)	4 (1, 3)	0 (0, 0)	2 (1, 1)

with information from simulation. The contribution from Drell-Yan and Z+jets is very small and is estimated directly from simulation.

Dilepton background events (including the τ as one of the leptons) contain at least two neutrinos, so these events can be important in the tails of the \cancel{E}_T distributions. These backgrounds are divided into the following categories: (i) 2ℓ events with one lost or ignored lepton ($\ell = e, \mu$), (ii) $\ell + \tau$ events with $\tau \rightarrow$ hadrons, and (iii) $\ell + \tau$ events with $\tau \rightarrow$ lepton. A lost lepton is one that is either not reconstructed or is out of the detector acceptance. An ignored lepton is one that is reconstructed but fails either the lepton-identification requirements (including isolation) or the p_T threshold requirement.

To estimate the background from dilepton events with lost or ignored leptons, we compute the ratio of the combined yield of dilepton events in the ee , $e\mu$, and $\mu\mu$ channels in data to the corresponding combined yield in simulated event samples. This ratio, which is 0.91 ± 0.07 for $H_T \geq 500$ GeV, 0.93 ± 0.15 for $H_T \geq 750$ GeV, and 0.87 ± 0.37 for $H_T \geq 1000$ GeV, is used to rescale the \cancel{E}_T distribution of dilepton events that appear in the signal region in simulation. (Events within 20 GeV of the nominal Z mass are excluded in the e^+e^- and $\mu^+\mu^-$ channels.) This approach is used because the dilepton control sample in data is small, and using it to obtain the shapes of \cancel{E}_T distributions would result in large statistical uncertainties. For all \cancel{E}_T bins above 250 GeV, the predicted yield from this background contribution is less than 6 events, and for all \cancel{E}_T bins above 350 GeV, the yield is at or below 1 event. The \cancel{E}_T distribution associated with the reconstructed dilepton events in data is well described by the simulation.

Dilepton events can also involve τ decays, either $\tau \rightarrow$ hadrons or $\tau \rightarrow \ell$. The \cancel{E}_T distributions in the dilepton events in data, when suitably modified to reflect the presence of a leptonic or hadronic τ decay, provide an accurate description of the shape of the \cancel{E}_T distribution of these backgrounds. Thus, to estimate the shape from the $\tau \rightarrow$ hadrons background, we effectively replace a lepton in a reconstructed dilepton event with a hadronic τ jet. Both hadronic and leptonic τ response functions are used, providing a probability distribution for a τ to produce a jet or a lepton with a given fraction $p_T(\text{jet})/p_T(\tau)$ or $p_T(\ell)/p_T(\tau)$. These response functions,

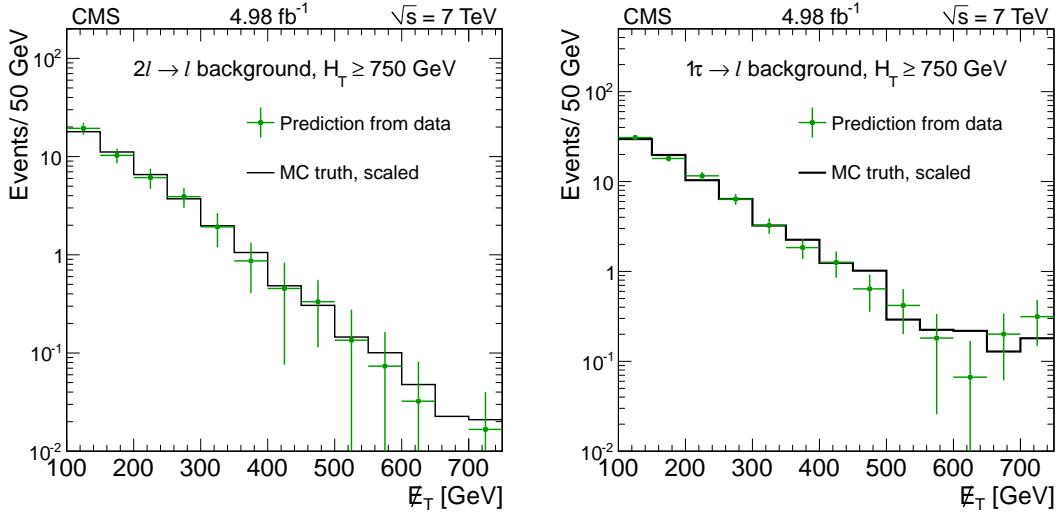


Figure 2: Predictions for dilepton and $\tau \rightarrow \ell$ backgrounds after requiring $H_T \geq 750$ GeV: control samples in data (green points with error bars) vs. MC predictions (black solid histogram) for (left) dilepton background and (right) $\tau \rightarrow \ell$ background. The MC prediction has been scaled to the integral of the data prediction.

obtained from simulation, are computed in bins of $p_T(\tau)$. This procedure can change the total number of jets above threshold in the event, as well as other properties such as H_T and \cancel{E}_T , which are recalculated. Simulated event samples are used to determine, for each of these processes i , the ratio $r_i = N_{\text{feed}}^i / N_{\text{control}}$ of the number of events observed in the single-lepton channel to the number of events in the control sample, as a function of \cancel{E}_T . This procedure effectively normalizes all such contributions to the control samples in data. For all \cancel{E}_T bins above 250 GeV, the number of dilepton events with a $\tau \rightarrow$ hadrons decay is predicted to be about 7 events or less and is much smaller in the higher \cancel{E}_T bins. The number of dilepton events with a $\tau \rightarrow \ell$ decay is predicted to be less than 3 events for all \cancel{E}_T bins above 250 GeV and is much smaller in the higher \cancel{E}_T bins.

Estimates for the $\tau \rightarrow \ell$ single-lepton backgrounds from $t\bar{t}$ and W +jets processes are based on a procedure similar to that used for the dilepton backgrounds, but in this case the single-lepton sample itself is used as the control sample. The \cancel{E}_T distribution obtained by applying the $\tau \rightarrow \ell$ response function to the data is rescaled by a ratio from simulation that gives the yield of $\tau \rightarrow \ell$ background events divided by the yield of events in the single-lepton control sample, as a function of \cancel{E}_T . The number of background events from the single $\tau \rightarrow \ell$ contribution falls from 33 for $H_T \geq 500$ GeV and $250 \leq \cancel{E}_T < 350$ GeV to 1.1 event for $H_T \geq 500$ GeV and $\cancel{E}_T \geq 550$ GeV.

The background predictions in data are shown in Fig. 2, where the expectation based on simulation is shown for comparison. The total predicted dilepton plus single $\tau \rightarrow \ell$ background yield ranges from about 50 events for $H_T \geq 500$ GeV and $250 \leq \cancel{E}_T < 350$ GeV to about 1 event for $H_T \geq 1$ TeV and $\cancel{E}_T \geq 550$ GeV. All of these predictions, as well as the expectations from simulation, are presented in Tables 2, 3, and 4, which are discussed in more detail in Section 5.4.

Background from QCD multijet events is suppressed to a level well below 1 event in nearly all signal regions, as shown in Tables 2, 3, and 4. The QCD multijet background is determined by first defining a control sample with small missing transverse momentum ($\cancel{E}_T < 50$ GeV) and with a lepton impact parameter relative to the beam spot $|d_0| > 0.02$ cm. These requirements

select a sample with little contamination from other SM processes such as $t\bar{t}$ and W +jets processes. Using this control sample, we measure the shape of the distribution in the combined relative isolation variable, $I_{\text{rel}}^{\text{comb}}$ (see Section 4). The shape of this distribution has very little correlation to \cancel{E}_T or to the lepton impact parameter (d_0), and so can be applied in the high- \cancel{E}_T signal regions. For each signal region in the data, we determine the background at low values of $I_{\text{rel}}^{\text{comb}}$ by first scaling the measured QCD multijet background shape in the relative isolation variable to the high- $I_{\text{rel}}^{\text{comb}}$ sideband of the signal region. The shape is then used to extrapolate the yield to the low- $I_{\text{rel}}^{\text{comb}}$ signal region. In the high- \cancel{E}_T signal regions, some non-QCD SM background can be present at high $I_{\text{rel}}^{\text{comb}}$, where the QCD background shape is normalized. We therefore subtract the estimated background from $t\bar{t}$, W +jets, and Z +jets from this region. These yields are taken from simulation, with systematic uncertainties determined from a comparison with a control region in the data.

5.4 Results from the Lepton Spectrum method

Tables 2, 3, and 4 compare the background yields predicted from the control samples in data with the yields obtained directly from simulation for $H_T \geq 500$ GeV, $H_T \geq 750$ GeV, and $H_T \geq 1000$ GeV, respectively. We observe that the single-lepton background is the dominant contribution in all regions. The various sources of uncertainties associated with these background determinations are discussed in Section 9. Finally, the yields observed in the signal regions in the data, which are listed at the bottom of each table, are consistent with the total background predictions based on the control samples. Thus, we observe no evidence for any excess of events in the data above the SM contributions.

Figure 3 shows the \cancel{E}_T distributions in data for the combined muon and electron channels, with all of the selection requirements, except that on \cancel{E}_T itself. The distributions are shown for $H_T \geq 500$ GeV, $H_T \geq 750$ GeV, and $H_T \geq 1000$ GeV, on both linear and logarithmic scales. The predicted \cancel{E}_T distribution (green-bar histogram) is a sum over three sources: single-lepton backgrounds (from $t\bar{t}$, single-top, and W +jets events), dilepton background from $t\bar{t}$, and single- τ events (from both $t\bar{t}$ and W +jets processes). The vertical span of the green bar corresponds to the statistical uncertainty on the background prediction. (The systematic uncertainties are computed in wider bins used for setting the limits and are given in Tables 2, 3, and 4.) In each signal region, the blue histogram shows the contribution from the dilepton and single- τ backgrounds only. It is evident that the single-lepton background is dominant in all cases. The \cancel{E}_T distributions for the SUSY benchmark models LM3 and LM6 are overlaid (not summed) for comparison. Systematic uncertainties and the interpretation are presented in Section 9.

6 Lepton Projection method

6.1 Overview of the Lepton Projection method

The Lepton-Projection (LP) method uses the difference between SM and SUSY processes in the correlation of the lepton transverse momentum and the missing transverse momentum. As previously discussed, in the SM processes the \cancel{E}_T corresponds to the neutrino in the decay of the W boson, either in W +jets or in $t\bar{t}$ events. The kinematics of W decays are dictated by the $V-A$ nature of the W coupling to leptons and the helicity of the W boson, as discussed in Section 3. Since W bosons that are produced with high transverse momentum in W +jets events exhibit a sizable left-handed polarization, there is a significant asymmetry in the p_T spectra of the neutrino and charged lepton. A smaller asymmetry is expected in W bosons from t quark (\bar{t} antiquark) decays, which yield W bosons which are predominantly longitudinally polarized

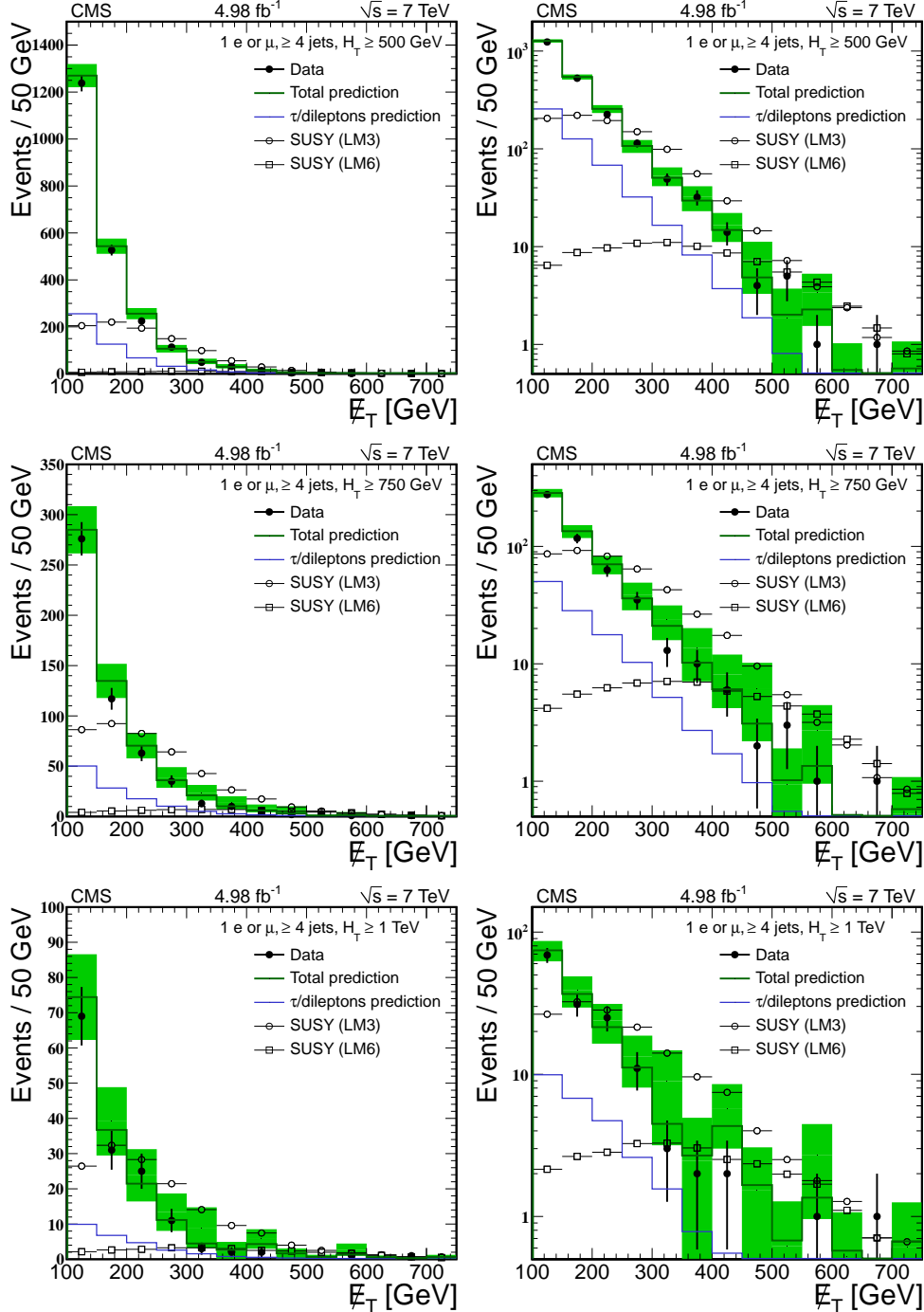


Figure 3: Lepton Spectrum method: observed E_T distributions in data (filled points with error bars) compared with predicted E_T distributions (green bars) in the combined electron and muon channels, on linear (left) and logarithmic (right) scales. Three different H_T thresholds are applied: $H_T \geq 500 \text{ GeV}$ (upper row), $H_T \geq 750 \text{ GeV}$ (middle row), and $H_T \geq 1000 \text{ GeV}$ (lower row).

with smaller left-handed (right-handed) components for W^+ (W^-).

We have measured the fraction of the helicity states of the W boson using an angular analysis of leptonic W decays [21]. Since the total momentum of the W boson in these decays, and therefore its center-of-mass frame, cannot be accurately determined because the momentum of the neutrino along the beam axis cannot be measured, an observable that depends only on transverse quantities is used. A variable that is highly correlated with the cosine of the polar angle in the center-of-mass frame of the W boson is the ‘‘lepton projection variable’’:

$$L_P = \frac{\vec{p}_T(\ell) \cdot \vec{p}_T(W)}{|\vec{p}_T(W)|^2}, \quad (3)$$

where $\vec{p}_T(\ell)$ is the transverse momentum of the charged lepton and $\vec{p}_T(W)$ is the transverse momentum of the W boson. The latter quantity is obtained from the vector sum of the electron transverse momentum and the missing transverse momentum in the event.

Since SUSY decay chains result in large values of \cancel{E}_T , and often result in relatively low values of the lepton momentum as well, the L_P distribution for SUSY events tends to peak near zero, whereas W +jets and $t\bar{t}$ yield a broad range of L_P values. This behavior is illustrated in Fig. 4, which compares the L_P distribution from both SM processes and from two representative SUSY benchmark points (LM3 and LM6).

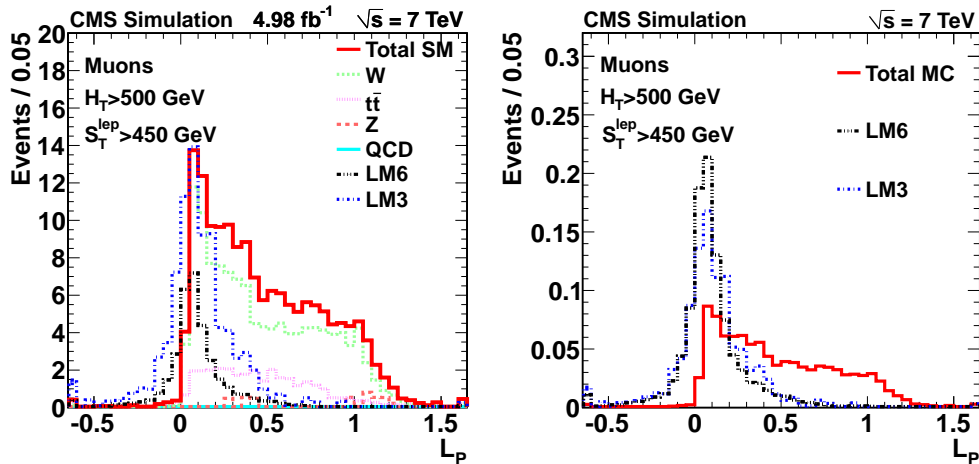


Figure 4: Distribution of L_P in SUSY and standard model processes from simulation. Left: all distributions are normalized to the integrated luminosity. The different contributions from SM processes are shown, whereas for SUSY two benchmark points, LM3 and LM6, are displayed. Right: the same distributions normalized to unity. The SM distribution is the sum of all the individual SM processes shown in the left pane. The quantity $S_T^{\text{lep}} = p_T(\ell) + \cancel{E}_T$ is discussed in the text.

In the L_P method, two regions in L_P are defined: the region with $L_P < 0.15$ is used as the signal region; the region with $L_P > 0.3$ is used as the control region, i.e., a sample that is depleted in the signal expected and is instead dominated by SM processes. These regions are selected using simulated event samples of W +jets, Z +jets, and $t\bar{t}$, that are collectively referred to as electroweak (EWK) processes in what follows, as well as with simulated SUSY events with SUSY particle masses near the region currently under exploration.

6.2 Background estimation in the L_P method

The key ingredient of the analysis is the estimate of the number of events in the signal region from the SM processes. We define a translation factor,

$$R_{CS} = \frac{N_{MC}(L_P < 0.15)}{N_{MC}(L_P > 0.3)}, \quad (4)$$

which is the ratio of the number of events in the signal and control regions for the EWK processes. The translation factor is obtained from MC simulation of the EWK processes, and the uncertainties on this factor are included in the systematic uncertainty of the background estimate. In the case of muons, where the background from QCD multijets is negligible, the total number of events predicted from SM processes in the signal region, $N_{SM}^{\text{pred}}(L_P < 0.15)$, can be determined directly from the number of events observed in the data in the control region, $N_{\text{data}}(L_P > 0.3)$:

$$N_{SM}^{\text{pred}}(L_P < 0.15) = R_{CS} \cdot N_{\text{data}}(L_P > 0.3). \quad (5)$$

In the case of the electrons, the presence of events from QCD multijet processes necessitates an independent evaluation of this background prior to the application of the translation factor for EWK processes.

The number of events estimated with this method is then compared to the number of events observed in the data in the signal region, $N_{\text{data}}(L_P < 0.15)$, for indications of an excess of events over the SM expectation. The analysis is performed in different regions of the event mass scale. To characterize the latter without affecting the correlation of the charged lepton and the neutrino in SM events, the scalar sum of the lepton transverse momentum and the missing transverse momentum, S_T^{lep} , is used: $S_T^{\text{lep}} = p_T(\ell) + \cancel{E}_T$. For W decays, $S_T^{\text{lep}} \approx p_T(W)$ at large values of $p_T(W)$.

In order to make the search optimization less dependent on the unknown energy scale of a new physics signal, the analysis is performed in disjoint ranges of S_T^{lep} and the results in these ranges are combined. In addition, the selection is also binned in a second dimension, the H_T variable, defined in Eq. (2).

As indicated in Table 1, the event selection used in this analysis is slightly different from the corresponding one in the LS analysis. To increase the sensitivity to SUSY decays, this analysis requires three or more jets. While this results in a significant increase in W +jets events, the additional SM background is mostly concentrated in the control region in L_P .

The event yields in the muon and electron channels, as predicted from simulation, are shown in Table 5. As discussed previously, the dominant backgrounds to the lepton plus jets and \cancel{E}_T signature arise from the production and decay of W +jets and $t\bar{t}$. The production of single W bosons in association with jets, and with large transverse momenta, is in general the larger of the two, especially at lower jet multiplicities. The majority of the $t\bar{t}$ background arises from semi-leptonic $t\bar{t}$ decays, with fully leptonic $t\bar{t}$ decays in which a lepton is either ignored or not reconstructed contributing about 20% of the total $t\bar{t}$ background.

A source of background, which is not listed in Table 5, stems from QCD multijet events in which a jet is misreconstructed as a lepton. The simulation indicates that the magnitude of this background is small in the control region and negligible in the signal region. Nevertheless, since the uncertainties in simulating these backgrounds can be significant, we use control data samples to estimate the background in the muon and electron channels.

Table 5: Expected event yields in the signal region ($L_P < 0.15$) from simulation. These yields are for $H_T > 500$ GeV. These MC values are only listed for illustration purposes.

$L_P < 0.15$	Muons: S_T^{lep} range [GeV]			Electrons: S_T^{lep} range [GeV]		
	[250–350]	[350–450]	[450– ∞]	[250–350]	[350–450]	[450– ∞]
$t\bar{t}(\ell)$	50.0 ± 1.0	15.3 ± 0.5	4.8 ± 0.3	37.9 ± 0.8	11.0 ± 0.4	3.6 ± 0.2
$t\bar{t}(\ell\ell)$	12.4 ± 0.4	3.9 ± 0.2	1.2 ± 0.1	10.4 ± 0.4	2.9 ± 0.2	0.8 ± 0.1
W	66.2 ± 2.0	35.6 ± 1.4	26.0 ± 1.2	48.9 ± 1.7	24.2 ± 1.2	20.9 ± 1.1
Z	2.1 ± 1.0	0.4 ± 0.4	0.0 ± 0.2	1.4 ± 0.8	0.0 ± 0.2	0.0 ± 0.2
Total MC	130.8 ± 2.4	55.3 ± 1.6	32.0 ± 1.3	98.6 ± 2.1	38.1 ± 1.3	25.3 ± 1.1
LM3	136.8 ± 3.8	89.1 ± 3.1	53.9 ± 2.4	111.7 ± 3.4	70.8 ± 2.7	47.0 ± 2.2
LM6	8.4 ± 0.2	11.0 ± 0.2	24.9 ± 0.3	6.7 ± 0.2	8.5 ± 0.2	20.5 ± 0.3

To estimate the background from QCD multijets in the muon final state, we use the relative combined isolation, $I_{\text{comb}}^{\text{rel}}$, of the muon. Multijet events are expected to populate the region at high values of $I_{\text{comb}}^{\text{rel}}$, whereas muons from SUSY decays are isolated and thus have low values of $I_{\text{comb}}^{\text{rel}}$. We employ an additional control data sample, which is specially selected to be enriched in QCD multijets, to determine the ratio of multijet events at low values of the relative isolation. Using this ratio and the number of multijet events expected in the control region of the sample passing the preselection requirements, we estimate the background from multijet events in the signal region to be always smaller than 1% of the EWK backgrounds. This level of background is negligible and is thus ignored in what follows.

The main sources of electrons in QCD multijet events are misidentified jets and photon conversions. This background is expected to be more substantial than the corresponding one in the muon sample, and its estimate exhibits a large dependence on the details of the simulation. For this reason, we estimate this background from control samples in data. The method relies on the inversion of one or more of the electron identification requirements in order to obtain a sample of anti-selected events, which is dominated by jets misidentified as electrons. We find that the inversion of the requirements on the spatial matching of the calorimeter cluster and the charged-particle track in pseudorapidity and azimuth leaves the relative fraction of the different background sources in QCD multijets unchanged. Moreover, to increase the number of events in this control sample, the requirements on d_0 and d_z are removed, while the isolation requirement is loosened. These changes to the event selection have a negligible effect on the L_P distribution in the data. In the simulated event samples, it is found that the L_P distribution from the control sample events provides a good description of the corresponding distribution from QCD background passing all selection requirements.

The L_P distribution obtained with this control sample is used as a template to fit, along with the L_P distribution from EWK processes, the L_P distribution in the data. In this fit, the EWK template is taken from simulation. This approach, which provides a template obtained from data for the QCD contamination, was applied in the measurement of the polarization of high- p_T W bosons [21]. The fit is performed in the control region ($L_P > 0.3$), where the possible presence of signal is highly suppressed. The numbers of QCD and EWK events obtained by the fit are used to estimate the total SM contamination in the signal region ($L_P < 0.15$). The method for estimating the number of SM events expected in the signal region is applied in each range of S_T^{lep} and H_T .

The method for estimating the SM expectation in the signal region is checked using two dif-

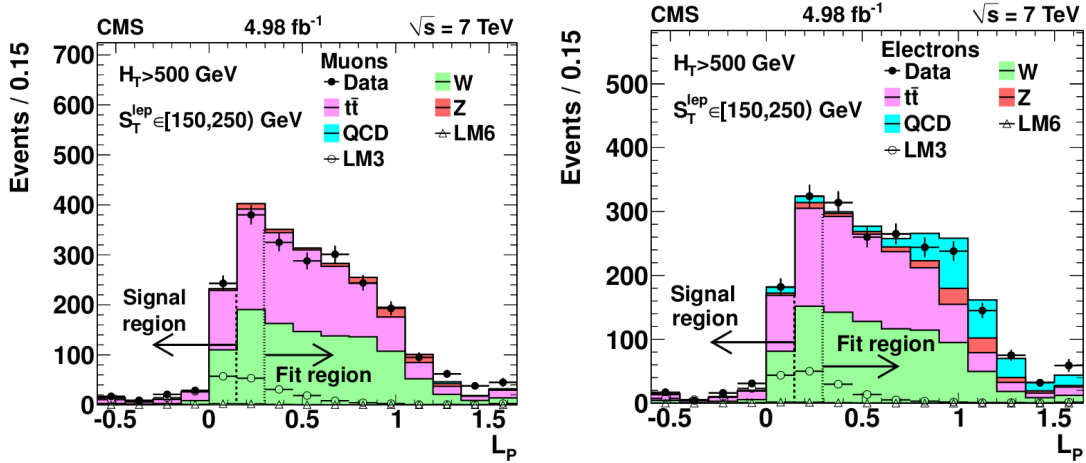


Figure 5: Fit results on data for $150 < S_T^{\text{lep}} < 250$ GeV, in the muon (left) and electron (right) search samples. The fit is performed in the control region ($L_P > 0.3$) and the result is extrapolated into the signal region ($L_P < 0.15$).

ferent control samples, where both the fit and signal regions have a negligible expected SUSY yield. The first sample is defined as all events satisfying the preselection requirements but confined to low values of S_T^{lep} : $150 < S_T^{\text{lep}} < 250$ GeV. The method described above is employed to predict the number of events expected in the signal region for both muons and electrons. This prediction is found to be fully consistent with the number of events observed in the data in signal region. The results of the fits and the yields of QCD and EWK events in the region of low S_T^{lep} (< 250 GeV) are displayed in Fig. 5 for the electron and muon samples. As can be seen in Fig. 5, the QCD contamination in the signal region, $L_P < 0.15$, is negligible, as expected, since low values of L_P favor events with low- p_T leptons and high \cancel{E}_T . The second sample, used only for events with muons, is collected with a separate trigger without any requirements on H_T or \cancel{E}_T . The muon transverse momentum threshold is raised to $p_T(\mu) > 35$ GeV, while the H_T threshold is lowered from 500 GeV to 200 GeV and the jet multiplicity requirement is reversed, to be fewer than three jets. Given these requirements on H_T and on the jet multiplicity, this control sample is dominated by SM processes. It is found that the estimated background agrees well with the number of events seen in the signal region $L_P < 0.15$.

6.3 Results of the L_P method

The L_P distributions in three ranges of S_T^{lep} , are displayed in Fig. 6 for muons (top) and electrons (bottom). Tables 6 and 7 list the numbers of events observed and the number of events expected from all SM processes as presented above, in the signal region, for the muon and electron channels, respectively. The predictions, along with the numbers of events observed in each range of S_T^{lep} and H_T , are also displayed graphically in Fig. 7 for muons and in Fig. 8 for electrons. The uncertainties quoted in Table 7 correspond to the statistical uncertainty of the fit, while the predictions displayed in Fig. 8 include the total statistical and systematic uncertainty.

All estimates of the total contribution expected from SM processes in the various bins in (S_T^{lep}, H_T) are consistent with the numbers of events observed in the data, with no visible excess from a potential SUSY signal. The result is interpreted as a limit in SUSY parameter space in the context of the CMSSM in Section 9.

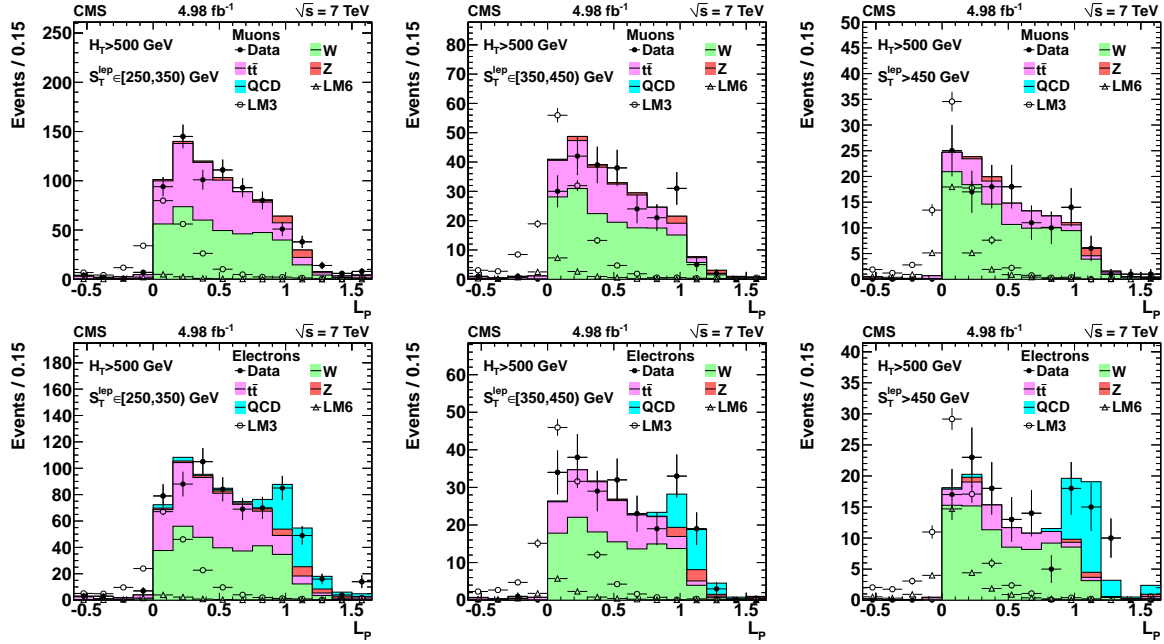


Figure 6: Data and fit results for the predictions for the L_P distribution, for events in the search sample, in different S_T^{lep} regions. Top plots for the muon channel; bottom plots for the electron channel. Left: $250 < S_T^{\text{lep}} < 350$ GeV, center: $350 < S_T^{\text{lep}} < 450$ GeV, and right: $S_T^{\text{lep}} > 450$ GeV.

Table 6: Event yields in data and MC simulation for the muon sample. The results in the columns labelled “Total MC” are listed for reference only. The corresponding uncertainties statistical only.

S_T^{lep} range [GeV]	Total MC Control region ($L_P > 0.3$)	Data	Total MC	SM estimate	Data
$500 < H_T < 750$ GeV					
[150–250)	1465 ± 11	1297	261 ± 3.2	$261 \pm 7 \pm 24$	258
[250–350)	452 ± 5.2	383	99.3 ± 2.1	$84.1 \pm 4.2 \pm 7.3$	78
[350–450)	154 ± 3.1	128	40.2 ± 1.4	$33.3 \pm 3.0 \pm 2.6$	23
≥ 450	59.2 ± 1.8	50	18.6 ± 1.0	$15.7 \pm 2.2 \pm 2.0$	16
$750 < H_T < 1000$ GeV					
[150–250)	280 ± 4.1	218	52.4 ± 1.6	$40.8 \pm 2.9 \pm 3.5$	46
[250–350)	91.9 ± 2.1	88	22.3 ± 0.9	$21.3 \pm 2.3 \pm 2.2$	22
[350–450)	34.6 ± 1.3	25	10.3 ± 0.6	$7.5 \pm 1.5 \pm 1.0$	8
≥ 450	26.7 ± 1.4	18	8.8 ± 0.6	$5.9 \pm 1.4 \pm 0.7$	7
$1000 \text{ GeV} < H_T$					
[150–250)	92.3 ± 2.5	76	20.5 ± 1.0	$16.9 \pm 1.9 \pm 1.7$	15
[250–350)	32.9 ± 1.3	31	8.7 ± 0.8	$8.2 \pm 1.5 \pm 1.0$	8
[350–450)	10.9 ± 0.7	7	4.6 ± 0.4	$2.9 \pm 1.1 \pm 0.6$	1
≥ 450	11.9 ± 0.8	12	4.6 ± 0.5	$4.6 \pm 1.4 \pm 0.7$	2

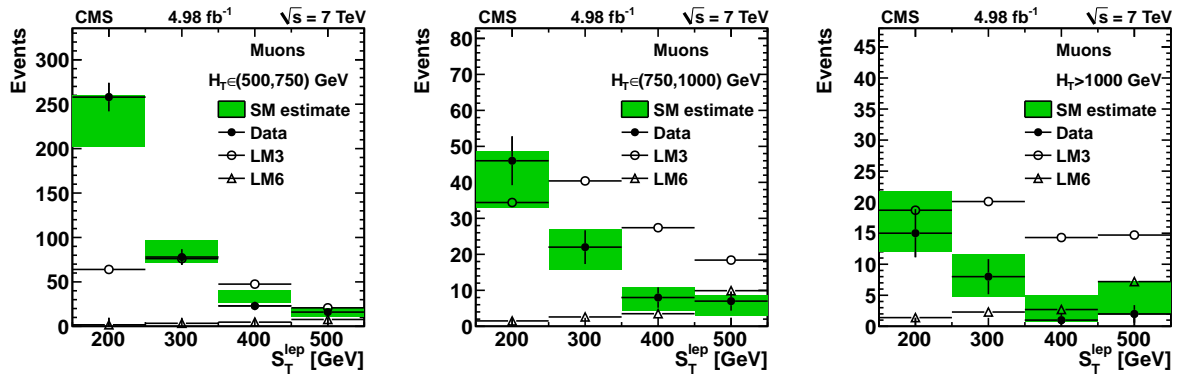


Figure 7: Comparison of the number of events observed in the data and the expectations from the background estimation methods for the muon channel, in the different S_T^{lep} bins. Left: $500 < H_T < 750$ GeV; Center: $750 < H_T < 1000$ GeV; Right: $H_T > 1000$ GeV. The error bars indicate the statistical uncertainty of the data only, while the green band indicates the total statistical and systematic uncertainty on the background estimate.

Table 7: Event yields in data and predictions of the numbers of EWK and QCD events for the electron sample in bins of H_T . The sum of predicted EWK events and predicted QCD events in the control region is constrained to be equal to the total number of data events. The background estimate used in comparing to the yields in the data is the result of the procedure described earlier and is listed in the row labeled “SM estimate”. The uncertainties for the QCD and EWK background estimates are statistical only. The uncertainties shown for the SM estimate are first the statistical uncertainty from the control region fit and second all other systematic uncertainties.

S_T^{lep} range [GeV]	QCD Control region ($L_P > 0.3$)	EWK	Data	QCD	EWK	SM estimate	Data
$500 < H_T < 750$ GeV							
[150–250)	184 ± 33	1122 ± 45	1306	9.1 ± 1.6	170 ± 7	$179 \pm 7 \pm 18$	204
[250–350)	66 ± 15	334 ± 22	400	2.1 ± 0.5	63.3 ± 4.1	$65.3 \pm 4.3 \pm 5.9$	71
[350–450)	26.6 ± 7.6	93 ± 11	120	0.3 ± 0.1	19.2 ± 2.3	$19.4 \pm 2.4 \pm 2.9$	29
≥ 450	17.1 ± 5.1	33.9 ± 6.6	51	0.2 ± 0.0	9.0 ± 1.8	$9.2 \pm 1.9 \pm 1.7$	11
$750 < H_T < 1000$ GeV							
[150–250)	39 ± 15	210 ± 20	249	1.9 ± 0.7	35.1 ± 3.3	$37.0 \pm 3.5 \pm 4.8$	37
[250–350)	5.8 ± 5.5	59.2 ± 9.1	65	0.2 ± 0.2	11.0 ± 1.7	$11.2 \pm 2.0 \pm 1.8$	13
[350–450)	0.0 ± 0.0	26.0 ± 5.1	26	0	6.3 ± 1.2	$6.3 \pm 1.2 \pm 1.5$	5
≥ 450	8.7 ± 3.4	22.3 ± 5.0	31	0.1 ± 0.0	6.7 ± 1.5	$6.8 \pm 1.6 \pm 1.5$	5
$1000 \text{ GeV} < H_T$							
[150–250)	14.9 ± 7.7	62 ± 10	77	0.7 ± 0.4	11.7 ± 1.9	$12.5 \pm 2.2 \pm 2.4$	9
[250–350)	10.4 ± 4.3	20.6 ± 5.4	31	0.3 ± 0.1	4.5 ± 1.2	$4.8 \pm 1.5 \pm 1.1$	8
[350–450)	0.5 ± 1.7	11.5 ± 3.7	12	0.0 ± 0.0	2.6 ± 0.8	$2.6 \pm 1.2 \pm 0.9$	1
≥ 450	4.4 ± 2.5	6.6 ± 2.9	11	0.0 ± 0.0	2.5 ± 1.1	$2.6 \pm 1.3 \pm 0.9$	1

7 The Artificial Neural Network method

7.1 Overview of the method

The Artificial Neural Network (ANN) method uses a multi-variate analysis to combine several event characteristics, other than \cancel{E}_T , into a single variable that distinguishes signal from background. Signal events then preferentially populate a signal region in the two-dimensional

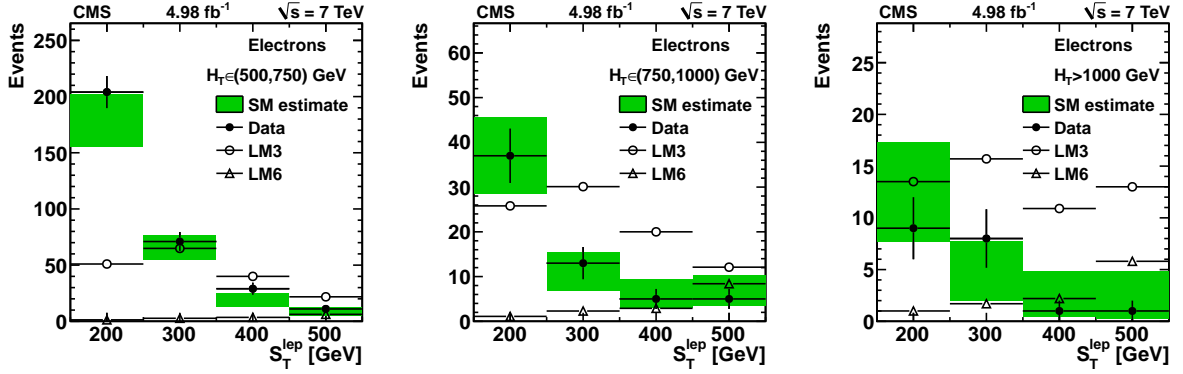


Figure 8: Comparison of the number of events observed in the data and the expectations from the background estimation methods for the electron channel, in the different S_T^{lep} bins. Left: $500 < H_T < 750$ GeV; Center: $750 < H_T < 1000$ GeV; Right: $H_T > 1000$ GeV. The error bars indicate the statistical uncertainty of the data only, while the green band indicates the total statistical and systematic uncertainty on the background estimate.

plane of the ANN output (z_{ANN}) and \cancel{E}_T , and the sidebands in this plane provide an estimate of the residual background.

Four input variables drive the ANN. The first two are n_{jets} , the number of jets with $p_T > 40$ GeV, and H_T , the scalar sum of the p_T of each jet with $p_T > 40$ GeV. The SUSY signal typically has heavy particles decaying via complex cascades, and as such, is likely to produce more jets and larger H_T than SM backgrounds. The third variable is $\Delta\phi(j_1, j_2)$, the angle between the two leading p_T jets in the transverse plane, which makes use of the greater likelihood that the two highest p_T jets are produced back-to-back in SM than in SUSY events. The final variable is M_T , the transverse mass of the lepton and \cancel{E}_T system. In $t\bar{t}$ and W +jets events, the lepton and \cancel{E}_T generally arise from the decay of a W boson, and as a result, M_T peaks near the W boson mass, with larger values arising only when there are additional neutrinos from τ or semileptonic decays. By contrast, in SUSY events, M_T tends to be greater than the W mass because of \cancel{E}_T due to undetected LSPs.

Figure 9 shows the distributions of these variables for simulated SM and SUSY events. The most powerful input variable is M_T ; n_{jets} and H_T also have considerable discriminating power. The $\Delta\phi(j_1, j_2)$ variable is weaker, but it still improves the sensitivity of the search. Lepton p_T also discriminates between the SM and SUSY, but it is not included in the ANN because its strong correlation with \cancel{E}_T in the SM would spoil the background estimate. Additional variables either do little to improve sensitivity or introduce a correlation between z_{ANN} and \cancel{E}_T . The input variables have similar distributions in the muon and electron channels, so we choose to train the ANN on the two channels combined, and use the same ANN for both. In general, the SM simulation describes the data adequately apart from a possible small structure near 130 GeV in the M_T distribution. Reweighting the simulation to match the M_T distribution in data does not affect the results of the analysis.

The ANN infrastructure uses standard ROOT utilities [42]. During training, weights are determined that minimize the root-mean-square deviation of background events from zero and signal events from unity. For the SUSY parameter space under study, our sensitivity depends only mildly on the details of the signal sample that trains the ANN. Specifically, for LM points 0 through 13 [30], the sensitivity is comparable (less than 30% variation) whether the ANN is trained on LM0, LM6 or LM9, even though these three training samples have rather different

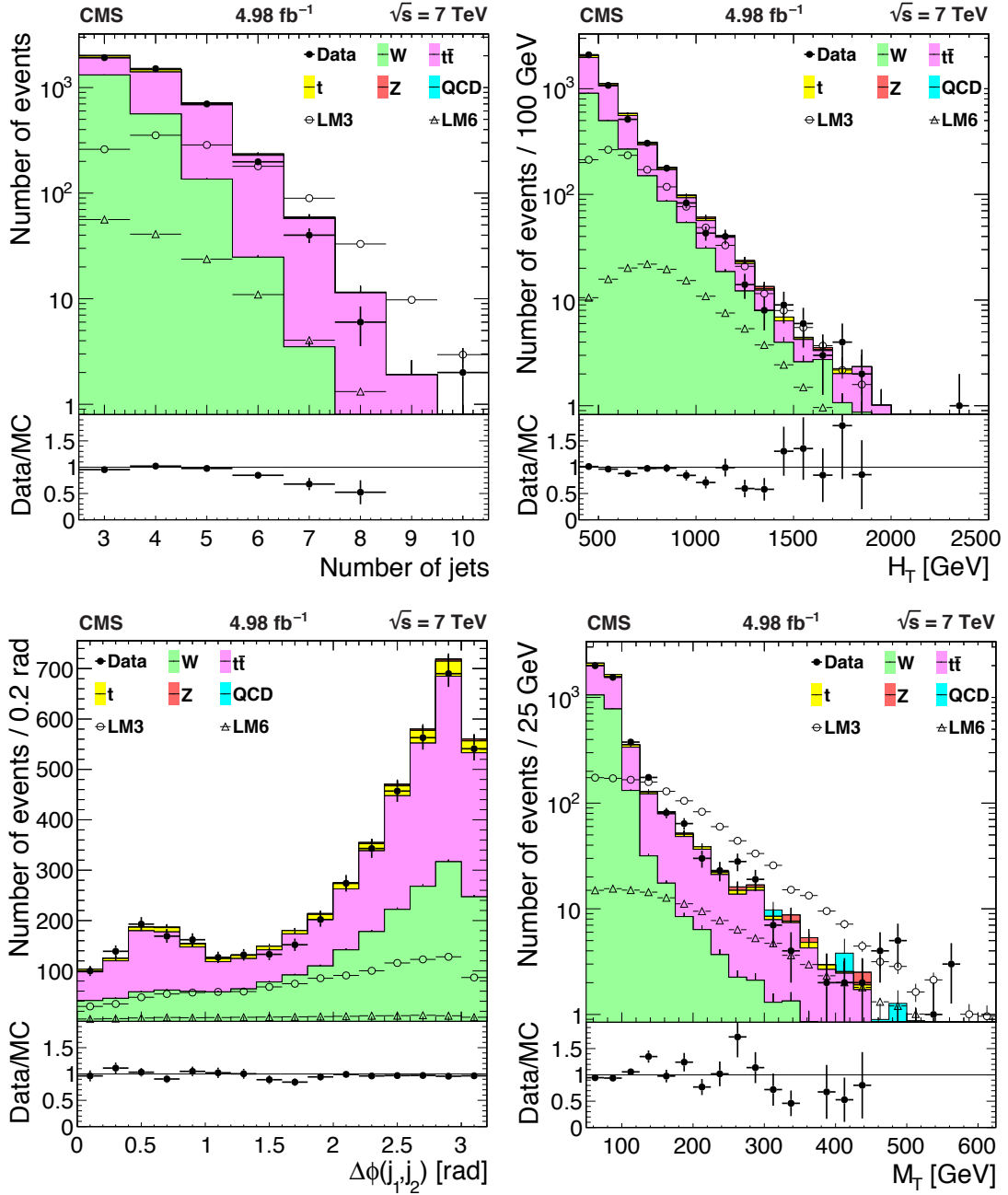


Figure 9: The distributions of n_{jets} , H_T , $\Delta\phi$, and M_T for data (solid circles), simulated SM (stacked shaded histograms), LM3 (open circles), and LM6 (open triangles) events after pre-selection. The small plot beneath each distribution shows the ratio of data to simulated SM yields. The muon and electron channels are combined.

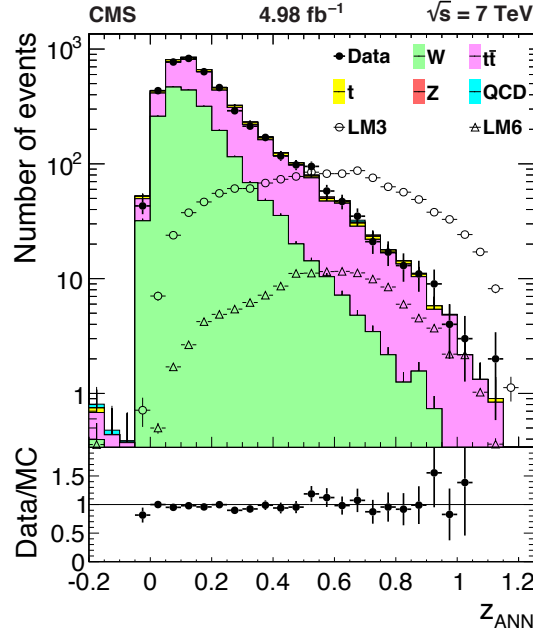


Figure 10: The z_{ANN} distribution of the data (solid circles) and simulated SM (stacked shaded histograms), LM3 (open circles), and LM6 (open triangles) events, after preselection. The small plot beneath shows the ratio of data to simulated SM yields.

characteristics. We select LM0 for training because it gives the best overall performance. The SM simulation provides the background sample.

Figure 10 compares the distributions of z_{ANN} for data and SM simulation for all events surviving the preselection. The two distributions are consistent within the uncertainties. The SM contribution is concentrated at small values of z_{ANN} , while the LM3 and LM6 SUSY distributions, which are also shown, extend to high values of z_{ANN} where the SM is suppressed.

We define two signal regions in the two-dimensional \cancel{E}_T and z_{ANN} plane. One region, referred to as the “low- \cancel{E}_T ” signal region, has $z_{\text{ANN}} > 0.4$ and $350 < \cancel{E}_T < 500$ GeV, while the other, the “high- \cancel{E}_T ” signal region, has the same z_{ANN} range, but $\cancel{E}_T > 500$ GeV. The high- \cancel{E}_T signal region minimizes the probability that the expected background fluctuates up to a LM6 signal when signal contamination is taken into account. We observe 10 events in the low- \cancel{E}_T signal region and 1 event in the high- \cancel{E}_T signal region.

7.2 Background estimation using the ANN sidebands

The sidebands in the two dimensional plane of \cancel{E}_T and z_{ANN} provide a strategy for estimating the background. The signal and sideband regions are shown in Fig. 11 and are denoted A, B, C, and D for the low- \cancel{E}_T signal region and A, B', C, and D' for the high- \cancel{E}_T signal region. The choice of boundaries for the sideband regions balances the competing needs of statistics and insensitivity to signal contamination against preserving similar event compositions in the signal and sideband regions.

The predicted yield in region D is given by

$$N_{\text{D,pred}} = \frac{N_{\text{B}} \times N_{\text{C}}}{N_{\text{A}}}, \quad (6)$$

where N_i is the yield in region i , and the predicted yield in region D' is defined similarly. This

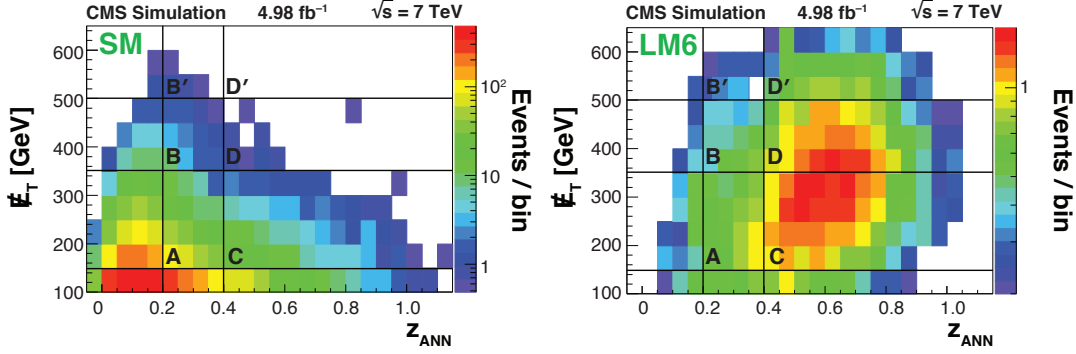


Figure 11: The yields of simulated SM (left) and LM6 (right) events in the E_T versus z_{ANN} plane. The regions D and D' are the low- E_T and high- E_T signal regions. The sideband regions are also indicated.

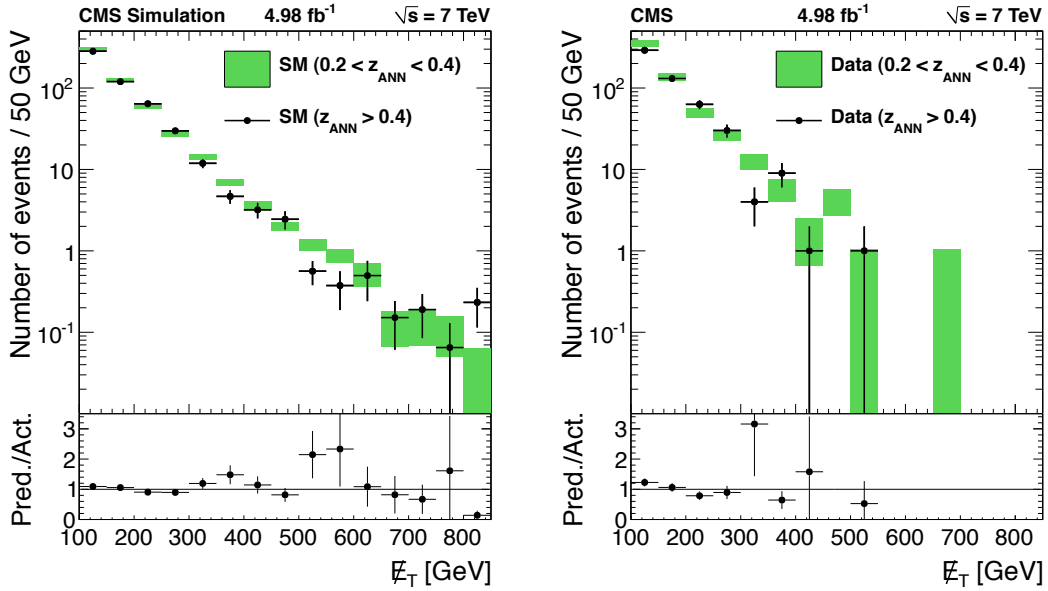


Figure 12: The E_T distributions of events in the z_{ANN} signal region (solid circles) and sideband (green bars) for simulated SM (left) and data (right) events. The distributions are normalized in the E_T sideband, $150 < E_T < 350$ GeV (regions A and C for the two distributions respectively). The rightmost histogram bin includes overflow. The small lower plots show the ratio of normalized sideband to signal yields.

procedure is equivalent to using the E_T distribution of the z_{ANN} sideband regions (A, B, and B') as a template for the E_T distribution of events with high z_{ANN} (C, D and D'), normalized using the yields in regions A and C. We test this estimation procedure using SM simulation: Fig. 12 (left) shows that the E_T distributions for low and high z_{ANN} are similar.

If a signal is present, it enters primarily in the signal regions D and D', but there are also significant contributions relative to the SM in regions B and B', somewhat increasing the predicted backgrounds in D and D'. This effect is accounted for in the final results.

Table 8 summarizes the event yields in the sideband subtraction regions for the various components of the SM background. The W +jets and $t\bar{t}$ dominate in all the regions, though their relative proportion varies. The W +jets events are most important at low z_{ANN} since M_T , which

Table 8: Event yields for the sideband (SB) and signal regions used in the ANN method. The uncertainties listed are statistical only.

Sample type	A	B	B'	C	D	D'
	z_{ANN} SB \cancel{E}_T SB	z_{ANN} SB Low \cancel{E}_T	z_{ANN} SB High \cancel{E}_T	z_{ANN} signal \cancel{E}_T SB	z_{ANN} signal Low \cancel{E}_T	z_{ANN} signal High \cancel{E}_T
$t\bar{t}$ single lepton	210 ± 8	4.8 ± 1.1	0.2 ± 0.2	55 ± 4	1.7 ± 0.7	$0.0^{+0.2}_{-0.0}$
$t\bar{t}$ dilepton (ℓ)	56 ± 4	0.3 ± 0.3	0.01 ± 0.01	109 ± 5	3.6 ± 1.0	0.2 ± 0.2
$t\bar{t}$ dilepton ($\tau \rightarrow \ell$)	3.9 ± 1.1	0.01 ± 0.01	0.3 ± 0.3	4.3 ± 1.0	$0.0^{+0.2}_{-0.0}$	0.2 ± 0.2
$t\bar{t}$ single τ	9.4 ± 1.7	0.3 ± 0.3	$0.0^{+0.2}_{-0.0}$	2.6 ± 0.8	$0.0^{+0.2}_{-0.0}$	$0.0^{+0.2}_{-0.0}$
Total $t\bar{t}$	279 ± 9	5.4 ± 1.2	0.5 ± 0.3	171 ± 7	5.3 ± 1.2	0.4 ± 0.3
W+jets	186 ± 3	20.4 ± 1.1	5.8 ± 0.6	40 ± 2	4.1 ± 0.5	1.6 ± 0.3
Single top quark	20 ± 1	1.5 ± 0.3	0.2 ± 0.1	11 ± 1	0.9 ± 0.2	0.1 ± 0.1
Z+jets	2.1 ± 0.3	$0.07^{+0.12}_{-0.07}$	$0.07^{+0.12}_{-0.07}$	0.8 ± 0.1	$0.03^{+0.05}_{-0.03}$	$0.03^{+0.05}_{-0.03}$
QCD multijet	$0.3^{+0.4}_{-0.3}$	$0.00^{+0.04}_{-0.00}$	$0.00^{+0.04}_{-0.00}$	0.1 ± 0.1	$0.00^{+0.02}_{-0.00}$	$0.00^{+0.02}_{-0.00}$
Total SM	487 ± 9	27.3 ± 1.8	6.6 ± 0.7	224 ± 7	10.3 ± 1.3	2.1 ± 0.4
Data	433	22	2	228	10	1
LM3	164 ± 3	21 ± 1	2.9 ± 0.4	579 ± 6	108 ± 3	17.8 ± 1.1
LM6	11.2 ± 0.3	6.0 ± 0.2	3.9 ± 0.1	44.6 ± 0.5	32.1 ± 0.4	21.0 ± 0.3

largely drives z_{ANN} , tends to peak near the W-boson mass. Because the W bosons (and hence their daughters) can be highly boosted, these events extend to very high values of \cancel{E}_T . As seen in Fig. 10, $t\bar{t}$ events are more likely to have high values of z_{ANN} than are W+jets events; this is because of the presence of dilepton $t\bar{t}$ events, in which both W bosons (from the top quark pair) decay leptonically, but only one lepton is identified (dilepton (ℓ)), giving large M_T . There is also a small contribution from events in which the lepton comes from the decay of a τ produced from a top quark decay, with the other top quark decaying either leptonically (dilepton ($\tau \rightarrow \ell$)) or hadronically (single τ). The remaining small backgrounds come from single-top-quark, QCD multijet and Z+jets events.

There are too few events in the simulated QCD multijet and Z+jets samples to populate the high \cancel{E}_T regions (B, B', D and D'). For the results quoted in Table 8 for QCD multijet and Z+jets events, we employ an extrapolation technique based on loosening the z_{ANN} and \cancel{E}_T requirements. The extrapolated numbers for all the regions are consistent with those obtained from the simulated samples. The simulated yields in the sideband and signal regions indicate that QCD multijet and Z+jets events are negligible.

The total SM simulation yields agree well with data in all regions, suggesting that the data share the main features described above. The z_{ANN} and \cancel{E}_T distributions are shown in Fig. 13.

7.3 Results of the ANN method

Figure 12 (left) shows the results of applying the background estimation method to the SM simulation. We find that the method correctly predicts the background within a factor of $\kappa = D'/D'_{\text{pred}}$ of 0.82 ± 0.12 (stat.) in the low- \cancel{E}_T signal region and 0.69 ± 0.16 (stat.) in the high- \cancel{E}_T signal region. The modest deviation from unity results from a correlation between z_{ANN} and \cancel{E}_T that arises because the W+jets background, which extends to large \cancel{E}_T values, dominates in the z_{ANN} sideband (because it tends to have M_T near the W mass), whereas dileptonic $t\bar{t}$ events, with their somewhat softer \cancel{E}_T spectrum, dominate in the z_{ANN} signal region.

Figure 12 (right) shows the \cancel{E}_T distributions of the data in the high and low z_{ANN} regions, after normalizing in the region $150 < \cancel{E}_T < 350$ GeV (A and C). Because the SM simulation appears to describe the data well, with, for example, consistent exponential decay constants describing

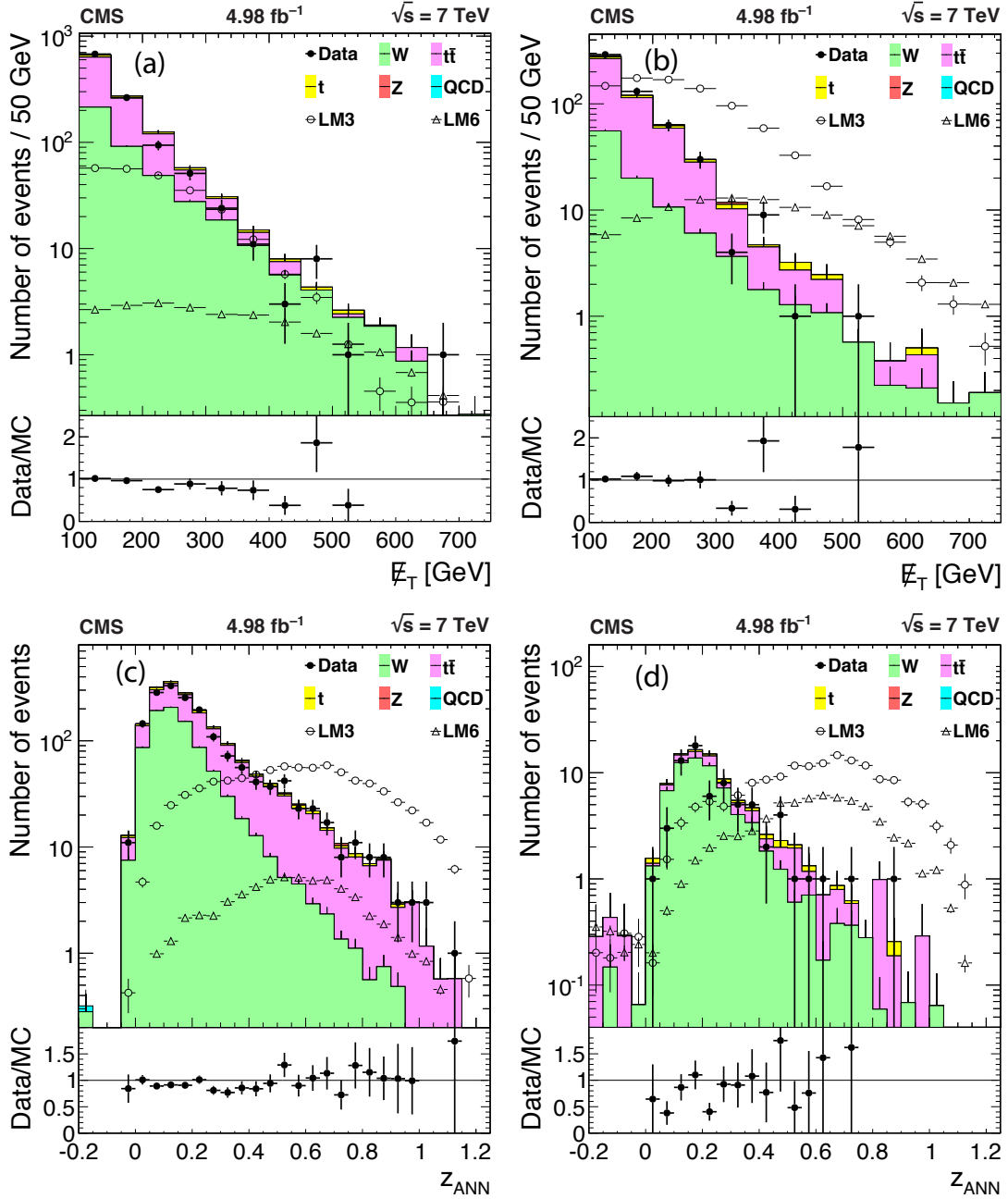


Figure 13: Distributions of E_T for (a) $0.2 < z_{ANN} < 0.4$ and (b) $z_{ANN} > 0.4$, and distributions of z_{ANN} for (c) $150 < E_T < 350$ GeV and (d) $E_T > 350$ GeV. The samples shown are data (solid circles), simulated SM (stacked shaded histograms), LM3 (open circles), and LM6 (open triangles) events. The small plot beneath each distribution shows the ratio of data to simulated SM yields.

the \cancel{E}_T distributions in the ANN sidebands, we choose to scale the background prediction of the data by κ . The uncertainty in the background from the relative cross sections of SM processes and other effects is quantified in Section 8. In the low- \cancel{E}_T signal region, we expect 9.5 ± 2.2 (stat.) events, and in the high- \cancel{E}_T signal region 0.7 ± 0.5 (stat.) events. The observed yields are 10 and 1 events, respectively, consistent with the background prediction.

8 Systematic uncertainties

Systematic uncertainties affect both the background estimates and the signal efficiencies. The sources of systematic uncertainty in the background predictions vary among the three methods, both because the final event selections differ and because the background estimation methods themselves differ. The systematic uncertainties stem from lack of perfect knowledge of the detector response and from uncertainties in the properties of the SM backgrounds. Common uncertainties for all methods are described in Section 8.1, while details that are specific to each method are given in Sections 8.2, 8.3, and 8.4 for the LS, L_P , and ANN methods, respectively. Tables 9, 10, and 11 list the main uncertainties associated with each method. The systematic uncertainties affecting the signal efficiency and luminosity, which are largely common to all methods, are described in Section 8.5.

8.1 Common uncertainties in the background predictions

Table 9: Sources of systematic uncertainties for the LS method and their effects on the background prediction in bins of \cancel{E}_T . The full list of systematic uncertainties is given for $H_T > 750$ GeV, and the total uncertainties are shown for $H_T > 500$ GeV and $H_T > 1000$ GeV. Each uncertainty is expressed as a change in the ratio of the predicted to the true number of events (evaluated with simulation). Uncertainties associated with the dilepton and QCD backgrounds are discussed in the text. The total uncertainty is the individual uncertainties summed in quadrature.

\cancel{E}_T [GeV]:	[250–350]	[350–450]	[450–550]	≥ 550
	(%)	(%)	(%)	(%)
$H_T > 750$ GeV				
Jet and \cancel{E}_T energy scale	11	13	14	16
Lepton efficiency	1	1	1	1
Lepton p_T scale	1	2	6	2
$\sigma(t\bar{t})$ and $\sigma(W)$	1	1	4	4
W polarization in $t\bar{t}$	1	1	1	1
W polarization in W+jets	3	4	12	11
Z+jets background	4	4	4	4
SM simulation statistics (K-factors)	4	7	12	17
Total systematic uncertainty	13	16	24	27
$H_T > 500$ GeV				
Total systematic uncertainty	16	18	29	30
$H_T > 1000$ GeV				
Total systematic uncertainty	15	18	28	32

The jet energy scale (JES) and its effect on \cancel{E}_T in the event can affect the H_T and \cancel{E}_T distributions and can also lead to differences between the lepton p_T spectrum and \cancel{E}_T spectrum. To under-

Table 10: Sources of systematic uncertainties for the L_P method and their effects on the background prediction in bins of S_T^{lep} for the muon and electron channels. The full list of systematic uncertainties are given for the range $500 < H_T < 750$ GeV, and the total uncertainties are shown for the two ranges $750 < H_T < 1000$ GeV and $H_T > 1000$ GeV. The total uncertainty is the individual uncertainties summed in quadrature.

S_T^{lep} range [GeV]:	[150–250)		[250–350)		[350–450)		≥ 450	
	(%)		(%)		(%)		(%)	
Channel	μ	e	μ	e	μ	e	μ	e
$500 < H_T < 750$ GeV								
Jet and \cancel{E}_T energy scale	6	6	4	5	5	9	9	9
Lepton efficiency	5	5	5	2	3	1	1	2
Lepton p_T scale	0	-	1	-	1	-	2	-
$\sigma(t\bar{t})$ and $\sigma(W)$	3	1	1	1	1	2	1	1
W polarization in $t\bar{t}$	0	1	1	1	1	1	1	2
W polarization in W+jets	2	1	2	1	2	3	3	4
\cancel{E}_T resolution	2	2	1	1	1	2	4	4
$t\bar{t}(\ell\ell)$	5	5	5	5	3	3	1	1
SM simulation statistics	1	1	2	2	4	5	6	7
Total systematic uncertainty	11	10	9	8	8	12	13	13
$750 < H_T < 1000$ GeV								
Total systematic uncertainty	9	12	10	11	13	13	12	13
$H_T > 1000$ GeV								
Total systematic uncertainty	10	15	13	15	20	18	16	20

stand the effects of energy-scale variations, we vary the jet energy scale as a function of p_T and η by amounts determined in independent studies of jet energy scale uncertainties [38], and corresponding to 2 GeV or less for jets with $p_T > 40$ GeV, and then recompute H_T and \cancel{E}_T . We also vary the energy scale of “unclustered” calorimeter deposits by 10% to take into account energy not clustered into jets (this effect is very small).

The uncertainty in the lepton efficiency accounts for differences between data and simulation and uncertainties in the trigger efficiencies. The lepton efficiencies are studied using a sample of lepton pairs with invariant mass close to the Z peak, in which one lepton satisfies tight selection criteria, and the second, reconstructed with relaxed criteria, serves as a probe of the tighter reconstruction and isolation requirements (“tag-and-probe” method [43]). Discrepancies between the data and simulation for electrons are maximal at low p_T (10% effect at around 20 GeV), and we reweight events as a function of lepton p_T to quantify the effect. The total lepton efficiency in data is described by simulation with an accuracy of 3%. Studies of the trigger that separately determine the efficiencies of the H_T^{trigger} , $\cancel{E}_T^{\text{trigger}}$, and lepton requirements show that the lepton inefficiencies dominate, and amount to 2% to 3% for leptons that are reconstructed successfully offline. Muon p_T scale uncertainties are obtained from the study of the q/p_T (transverse curvature with sign given by the electric charge q) distribution of muons in Z events in data. By comparing the q/p_T distribution of positive and negative muons it is possible to quantify the amount of bias in the measurement of q/p_T .

The relative amount of $t\bar{t}$ and W+jets background affects each analysis method through corrections obtained from simulation. The contributions from $t\bar{t}$ and W+jet have not been specifically measured in the narrow region of phase space studied in this analysis and their relative contribution must be evaluated. The $t\bar{t}$ cross section is validated using an algorithm based on the

Table 11: Sources of systematic uncertainties for the ANN method and their effects on the background prediction in bins of \cancel{E}_T . The total uncertainty is the individual uncertainties summed in quadrature.

\cancel{E}_T range [GeV]:	[350–500] (%)	≥ 500 (%)
Jet and \cancel{E}_T energy scale	3	4
Lepton p_T scale	3	5
Lepton efficiency	0.3	0.4
$\sigma(t\bar{t})$ and $\sigma(W)$	3	2
W polarization in W+jets	1	3
W boson p_T spectrum in W+jets	10	2
$t\bar{t}(\ell\ell)$	1	7
Other backgrounds	1	1
SM simulation statistics	15	23
Total systematic uncertainty	19	26

reconstructed top-quark masses for both the hadronic and the leptonic top-quark decays. The uncertainty in the $t\bar{t}$ cross section is determined by comparing yields in data and simulation after a selection based on top mass variables. The W+jets cross section is validated by comparing event yields between data and simulation in Z+jets events in a dedicated dilepton event selection with similar kinematics. We assign an uncertainty to the W+jets cross section based on the agreement of the data and simulation in the Z+jets sample. Using the uncertainties obtained for the $t\bar{t}$ and W+jets cross sections, we probe different relative contributions of $t\bar{t}$ and W+jets events in our sample and the effect on our background predictions.

Uncertainties in the polarization fraction for the W boson, either in $t\bar{t}$ or W+jets events, must be taken into account. For the W polarization in $t\bar{t}$ events, the theoretical uncertainties are very small (see Section 3) and have negligible effect on the background predictions. The W polarization in W+jets events, which is described in more detail in Section 3, is more complicated than in $t\bar{t}$ production. In this case, we consider the effect of conservative variations of the helicity fractions in bins of W-boson p_T and η with respect to the theoretical NLO calculations [36].

For the dilepton $t\bar{t}$ background, $t\bar{t}(\ell\ell)$, the uncertainties are evaluated somewhat differently for the different methods. In the L_P and ANN methods this background is evaluated together with the same control sample as for the main single-lepton background prediction. Uncertainties in the prediction can arise from finite detector acceptance, inefficient lepton identification, and cross section uncertainties. In the LS method the dilepton $t\bar{t}$ background is not predicted using the single-lepton background prediction and separate control samples must be used. Thus the uncertainties for the dilepton $t\bar{t}$ background are estimated separately and described in the next section.

The small residual QCD multijet background is probed by inverting the requirement on $I_{\text{rel}}^{\text{comb}}$ or the electron selection criteria to obtain QCD dominated control samples. Contamination from $t\bar{t}$ and W+jet events in these control samples must be considered and the uncertainties on their cross sections are the dominant uncertainty for these methods.

The Z+jets contribution to the signal regions is very small and uncertainties on this background prediction come from lepton efficiency and cross section uncertainties. In addition, for the LS method there is a small Z+jets contamination to the single-lepton control sample, which must be subtracted, and lepton efficiency and cross-section uncertainties are considered for this as well.

8.2 Lepton Spectrum method background prediction uncertainty

For the LS method, the systematic uncertainties for each of the different background predictions from control samples in data (1 ℓ , dilepton, 1 τ , QCD, and Z+jets) are included in Tables 2, 3, and 4. To determine the systematic uncertainties for the largest source of background, 1- ℓ events (arising from $t\bar{t}$, W+jets, and single-top processes), we evaluate deviations for the \cancel{E}_T -dependent correction factor, which is determined from simulation and applied to the 1- ℓ background prediction (see Section 5.2). Table 9 gives a breakdown of the contributions of the systematic uncertainties for the 1- ℓ prediction in bins of \cancel{E}_T and for $H_T > 750$ GeV. The uncertainties in the 1- ℓ prediction for the $H_T > 500$ GeV and $H_T > 1$ TeV signal regions are similar to those listed in Table 9. The largest source of uncertainty arises from the potential difference in the muon p_T and the \cancel{E}_T scales, because the muon p_T spectrum is used to predict the \cancel{E}_T spectrum. The statistical uncertainties in the correction factors (denoted as K-factors in Table 9) for the 1- ℓ method are slightly smaller than the combined systematic uncertainty of the correction factor. Table 9 does not include an uncertainty from jet resolution effects because this is taken into account by the smearing of the lepton p_T spectra by QCD multijet \cancel{E}_T templates (described in Section 5.2). For the purposes of setting limits, the total systematic uncertainty in the 1- ℓ background prediction is treated as correlated across all bins in \cancel{E}_T .

Tables 2, 3, and 4 also list the non-single-lepton backgrounds, which account for about 25% of the total, with a relative uncertainty of 5–10% in the lowest- \cancel{E}_T bin and about 30% in the highest- \cancel{E}_T bin. For the dilepton prediction of lost and ignored leptons (described in Section 5.3) the main sources of systematic uncertainty arise from the lepton reconstruction and identification efficiencies and the top-quark p_T spectrum. The uncertainties on the lepton efficiencies are described in Section 8.1, and the uncertainty associated with the top-quark p_T spectrum is determined from varying the fraction of events in the tail of this distribution in simulation in a manner consistent with the uncertainty in this tail as observed in data. This uncertainty is then propagated through the background determination procedure.

8.3 Lepton Projection method background prediction uncertainty

For the L_P method, the estimate of the total number of events expected from SM processes in the signal region, $N_{SM}^{\text{pred}}(L_P < 0.15)$, relies on the knowledge of the translation factor, R_{CS} , as well as the number of events observed in the control region, subtracted for the QCD background, $N_{\text{data}}(L_P > 0.3)$. There are, therefore, two sources of uncertainty in this estimate: uncertainties in the number of events from EWK processes in the control region and uncertainty in R_{CS} . The relative change on the predicted background from each source of systematic uncertainty is listed in Table 10 for both muons and electrons. The largest uncertainty for high S_T^{lep} bins is the statistical uncertainty in the data in the control region. The second largest uncertainty comes from the JES uncertainty. The effect from the JES uncertainty is larger in the electron channel, since the JES affects also the shape of the L_P distribution used in the fit of the control region. The uncertainty in the resolution of the measurement of the hadronic energy recoiling against the lepton and \cancel{E}_T is evaluated conservatively by smearing the total recoil energy in simulation by an additional 7.5% along the direction of the recoil and by 3.75% in the direction orthogonal to the recoil. This decreases the resolution more than 10% for the high recoils (above 250 GeV) of the signal region and thus covers the difference between data and simulation.

8.4 ANN method background prediction uncertainty

For the ANN method, the systematic uncertainty in the background prediction is dominated by the statistics of the simulation, which probes for bias in the background estimation. Another

important uncertainty comes from the p_T spectrum of the W boson in W +jets events, since it affects the \cancel{E}_T distribution of these events, which preferentially populate the z_{ANN} sideband. To assess the impact, we reweight the p_T spectrum of W boson events, using the differences in the p_T spectra of Z bosons in data and simulation as a guide. This uncertainty is driven by the statistics of the Z +jets sample. The relative proportions of W +jets and $t\bar{t}$ events differ in the z_{ANN} signal and sideband regions so the background prediction depends on their relative cross sections. Those $t\bar{t}$ events with two leptons in the final state, only one of which is observed, have large \cancel{E}_T and are the source of most SM events in the signal region. In addition to the $t\bar{t}$ cross section, this background depends on lepton acceptance and identification inefficiencies. Additional sources of systematic uncertainty are the hadronic and leptonic energy scales. Table 11 summarizes these uncertainties.

8.5 Signal efficiency and other multiplicative uncertainties

The systematic uncertainty in the signal yield arises from the uncertainty in the signal efficiency. In general, this uncertainty is correlated across \cancel{E}_T or S_T^{lep} bins. The JES component of the signal efficiency uncertainty is computed separately for each model point in CMSSM and simplified model parameter space and is correlated with the JES uncertainty in the single-lepton background prediction. The systematic uncertainties in the signal efficiency associated with lepton reconstruction and the trigger amount to 3%. The uncertainty in the integrated luminosity is 2.2% [44]. The systematic uncertainty in the signal efficiency, not including the JES component, is 6% for each of the analyses.

9 Results and interpretation

The LS, L_P , and ANN methods each yield SM background predictions that are consistent with the number of events observed in data. We therefore proceed to set exclusion limits on SUSY model parameters. All limits are computed using the modified-frequentist CLs method [45] with a one-sided profile likelihood test statistic. To interpret the absence of an observed signal, three complementary approaches are used.

9.1 Constraints on CMSSM parameter space

First, we scan over models in the CMSSM and determine whether the number of events predicted at each model point in parameter space can be excluded by the measurements. This procedure relies on the fact that the CMSSM parameter space can be described with just five parameters, and we fix three of them to commonly used values ($A_0 = 0 \text{ GeV}$, $\mu > 0$, $\tan \beta = 10$). Each model point has a complete SUSY particle spectrum and a well defined cross section, which typically involves several production subprocesses. The CMSSM simulated samples are initially generated using leading-order cross sections. At each point in CMSSM parameter space, the predicted yields for each production subprocess (e.g., $gg \rightarrow \tilde{g}\tilde{g}$) are corrected using the NLO cross sections discussed in Ref. [46]. Using the observed yield in data and the predicted background, we determine whether the CMSSM yield for the particular model point can be excluded at the 95% confidence level (CL). This procedure is complicated by the fact that the control regions in data could potentially be contaminated by signal events. This effect is taken into account for each model by removing the expected contribution to the predicted background arising from signal contamination of the control regions.

Figures 14, 15, and 16 show the CMSSM exclusion region [47] for the three background estimation methods, evaluated in the $m_{1/2}$ vs. m_0 plane, with the values of the remaining CMSSM parameters fixed at $\tan \beta = 10$, $A_0 = 0 \text{ GeV}$, and $\mu > 0$. Figure 17 displays all of the results

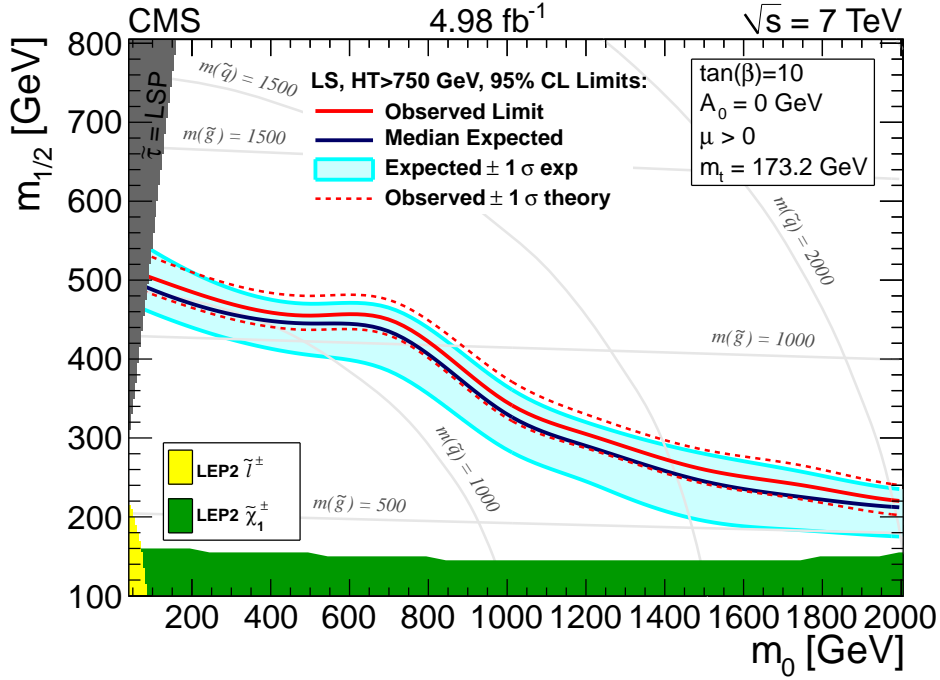


Figure 14: LS method: exclusion region in CMSSM parameter space for the $H_T > 750 \text{ GeV}$ selection.

together. The excluded regions are below the plotted curves, corresponding to SUSY particle masses below certain values. For reference, the plots display curves of constant gluino and squark masses. The lines of constant gluino mass are approximately horizontal with $m(\tilde{g}) \approx 2.5 m_{1/2}$. Lines of constant squark mass are strongly curved in the $m_{1/2}$ vs. m_0 plane. At low m_0 , the analyses exclude gluinos with masses up to about 1.3 TeV, but the sensitivity falls with increasing m_0 . To determine the one standard deviation (σ) theoretical uncertainty on the observed limit, the signal yields are recomputed after changing each of the process-dependent SUSY production cross sections at each model point by $\pm 1\sigma$ of their uncertainty arising from the parton distribution functions and renormalization and factorization scales [46].

9.2 Constraints on simplified model parameter space

The second approach to interpretation is based on the use of simplified models [14, 15], which provide a more generic description of new physics signatures. Such models do not include a full SUSY particle spectrum, but instead include only the states needed to describe a particular set of decay chains of interest. Rather than excluding a model, the procedure is to calculate cross section upper limits on a given topological signature. (Such cross section limits can, however, be converted into limits on particle masses within the assumptions of the particular model.) Because simplified models do not describe a full SUSY spectrum, the number of free parameters is small. Furthermore, the parameters are simply the masses of the SUSY particles, in contrast to the grand-unified-theory-scale parameters used in the CMSSM. An advantage of simplified models is that, as a consequence, certain relationships between particle masses that arise with the CMSSM no longer hold, and the spectra can be much more generic.

We consider the “Topology 3 weakino” (T3w) simplified model, which involves the production of two gluinos and their decay via the mechanism shown in Fig. 18. One gluino is forced to decay into two quark jets plus the LSP ($\tilde{\chi}^0$) via the three-body decay $\tilde{g} \rightarrow q\bar{q}\tilde{\chi}^0$, while the

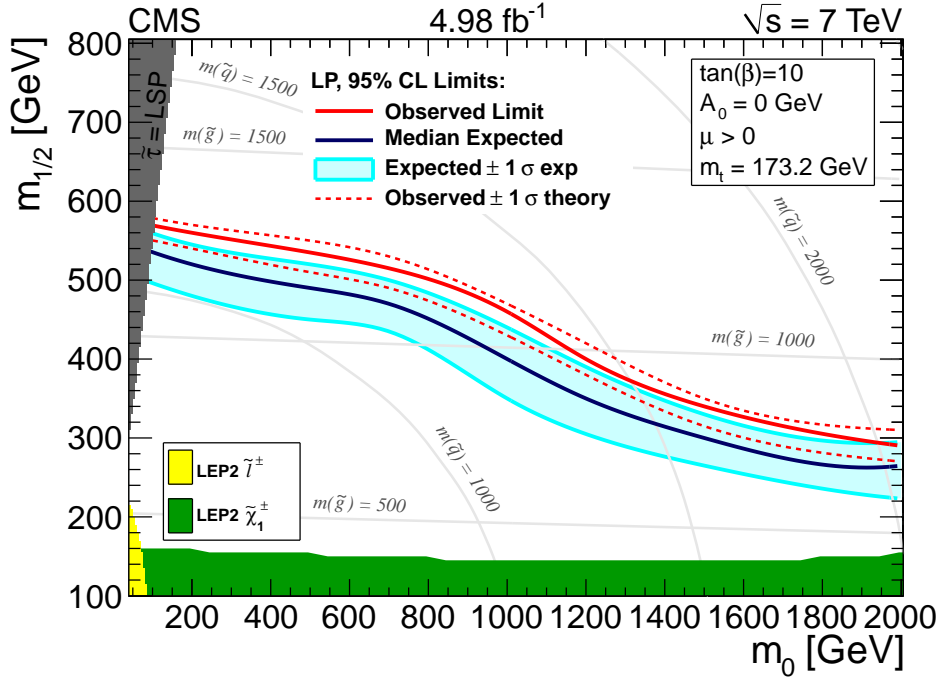


Figure 15: L_P method: exclusion region in CMSSM parameter space for all H_T bins combined.

other gluino decays via $\tilde{g} \rightarrow q\bar{q}'\tilde{\chi}^\pm$, followed by $\tilde{\chi}^\pm \rightarrow W^\pm\tilde{\chi}^0$. The W^\pm boson can then decay leptonically. The T3w model is specified by masses of the gluino, the LSP ($\tilde{\chi}^0$), and an intermediate chargino ($\tilde{\chi}^\pm$). We calculate cross section limits as a function of $M(\tilde{g})$, assuming a fixed value for the LSP mass $M(\tilde{\chi}^0) = 50 \text{ GeV}$ and setting the chargino mass according to $M(\tilde{\chi}^\pm) = 0.5(M(\tilde{\chi}^0) + M(\tilde{g}))$. The nominal production cross section for the gluino pair production mechanism is given in Ref. [46]. Figure 19 shows the cross sections excluded by each method for this model. The limits fluctuate significantly at low $M(\tilde{g})$ because of the low signal efficiency in this region.

9.3 Alternate model exclusions

The data can be interpreted using a third approach, which is applicable to models that do not fall within the scope of either the CMSSM or the simplified model discussed in this section. A model builder can investigate the sensitivity of any one of the three methods presented in this paper to a given signal hypothesis by applying the event selection requirements listed in Table 1, together with the final requirements that define the signal regions. We provide a simple efficiency model for the most important observables used in the event selections. The efficiency model can then be applied to a basic (PYTHIA) simulation of the signal process.

The efficiency model is based on parametrizations of the efficiencies for the event selection requirements with respect to the main reconstruction objects and quantities, such as H_T , \cancel{E}_T , and lepton p_T . The efficiency of the analysis for a given model can be estimated by applying these individual reconstruction efficiencies, which are given as a function of the most important parameter (such as lepton p_T), to the corresponding kinematic distributions in the model. This procedure would then yield an estimate for the number of signal events from the model. Finally, the sensitivity of the analysis to the model can be obtained by comparing the yield of signal events obtained in this manner with the background yields given in this paper. Kinematic correlations (which can be model dependent) are not taken into account, but this approach

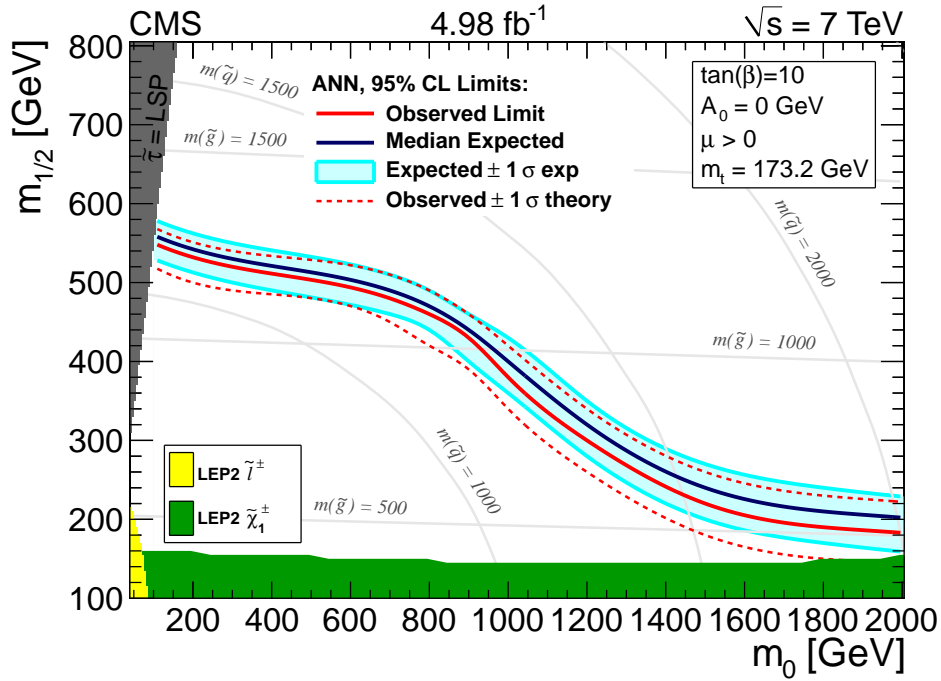


Figure 16: ANN method: exclusion region in CMSSM parameter space.

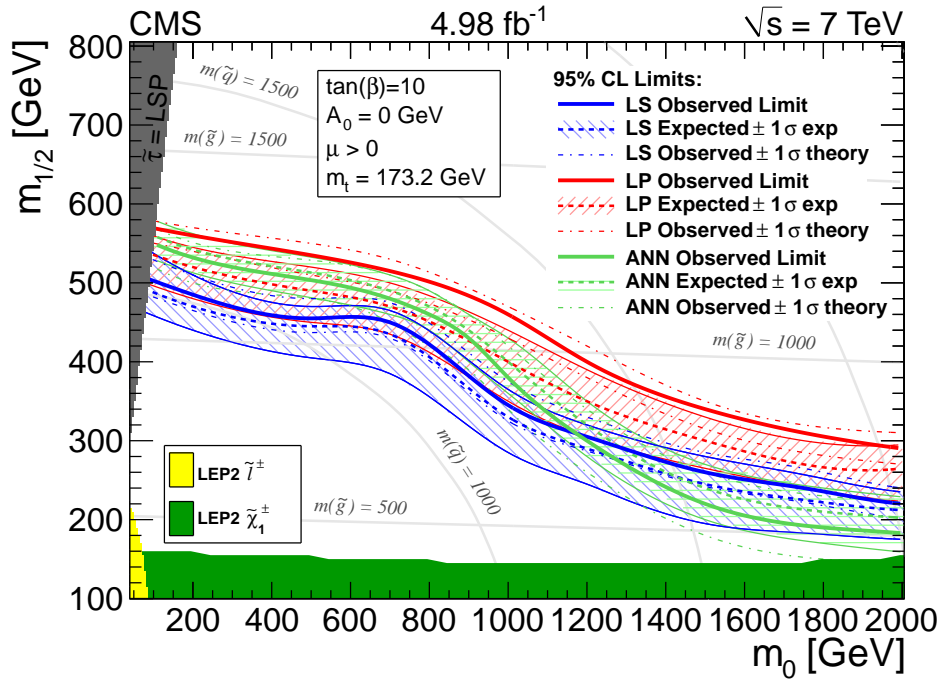


Figure 17: Exclusion region for the LS, L_P , and ANN methods in CMSSM parameter space. Results from the low- and high- E_T signal regions are combined.

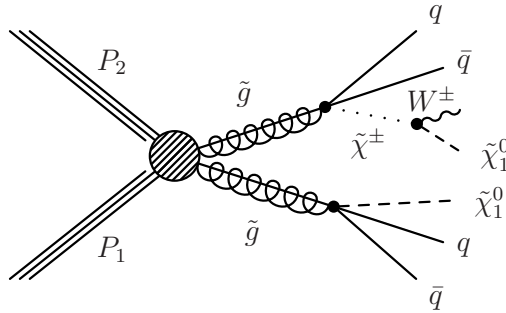


Figure 18: Diagram for production and decay in the T3w simplified model.

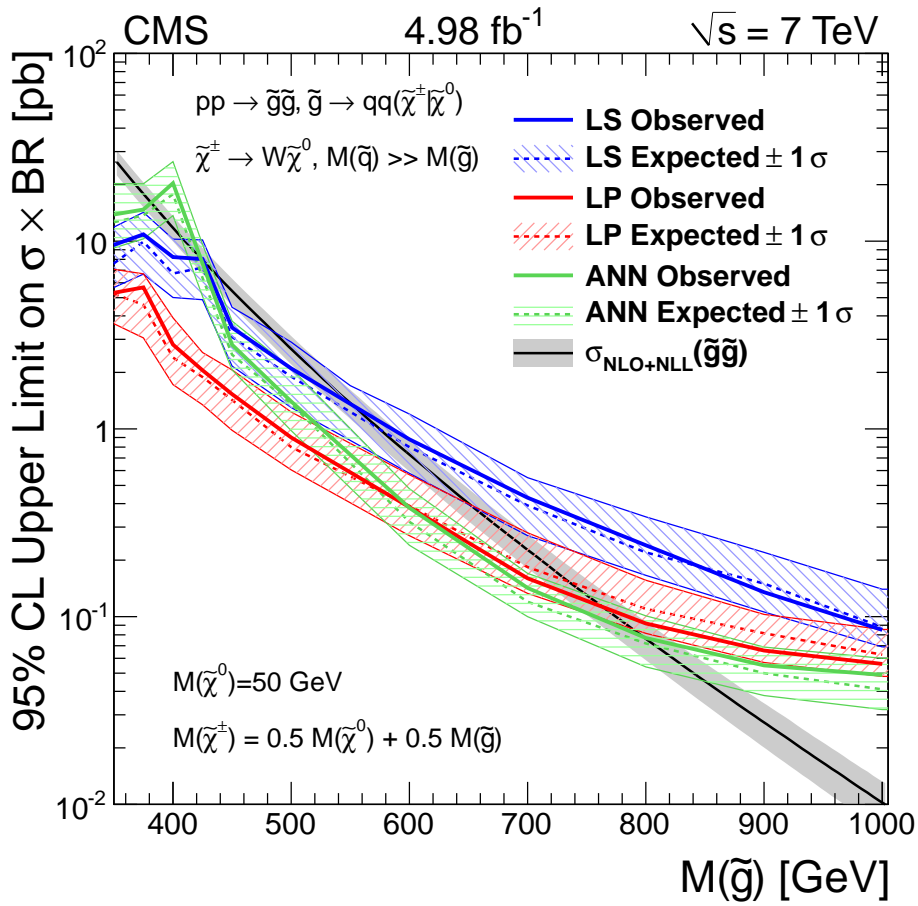


Figure 19: Excluded cross sections for the LS, L_P , and ANN methods for the T3w simplified model.

nonetheless provides a first approximation to the sensitivity.

The efficiencies for each analysis object are described using “turn-on” curves, which are simply error functions,

$$\epsilon(x) = \epsilon_{\text{plateau}} \frac{1}{2} \left[\text{erf}\left(\frac{x - x_{\text{thresh}}}{\sigma}\right) + 1 \right], \quad (7)$$

where x represents the variable most relevant for the reconstruction of the particular object. The error function is parametrized in terms of the plateau efficiency, $\epsilon_{\text{plateau}}$; the turn-on threshold, x_{thresh} ; and the characteristic width of the turn-on region, σ . These parameters are obtained by fitting simulated event samples as a function of the true (generated) value.

The selection efficiency associated with the lepton reconstruction, identification, and isolation requirements is estimated as a function of lepton p_T by considering muons and electrons (including those from τ decay) generated in the PYTHIA-simulated hard-scattering process. The lepton isolation requirement has a large effect on the efficiency, which consequently depends on the number of jets in the event. To reduce the model dependence arising from this effect, two categories of leptons are considered. First, we assign zero efficiency to leptons that are within $\Delta R < 0.4$ of a quark or gluon with $p_T > 40$ GeV in the hard-scattering process. The efficiency for the remaining leptons is described by a turn-on curve whose parameters are listed in Table 12. The efficiencies are specified for both the lepton selection and for the lepton veto.

Table 12: Efficiency-model parameters for lepton efficiencies as a function of $x \equiv p_T$. The leptons are required to lie within the fiducial region and must satisfy the p_T thresholds specified in Table 1.

Lepton	$\epsilon_{\text{plateau}}$	$x_{\text{thresh}}[\text{GeV}]$	$\sigma [\text{GeV}]$
Muon (signal)	0.86	2.7	65
Muon (veto)	0.90	-17	75
Electron (signal)	0.74	20	61
Electron (veto)	0.83	2.3	54

The number of jets and the resulting H_T value for each event are computed using information available at the generator level. The same clustering algorithm used to reconstruct jets in the data is applied to the generator-level particles. The resulting generator-level jets are required to satisfy $\Delta R > 0.3$ with respect to the leptons described above. The \cancel{E}_T variable is estimated at the generator level from the transverse momenta of neutrinos and any new weakly interacting particles, such as the $\tilde{\chi}^0$. The parametrizations of the efficiency turn-on curves for the H_T and \cancel{E}_T requirements are listed in Tables 13 and 14, respectively. For the requirements used with the LS method, the information given in these tables generally reproduces the efficiency from full simulation to within about 15%.

In the L_P method, the variables L_P and S_T^{lep} are functions of lepton p_T and \cancel{E}_T . The modeling of lepton p_T is described above. To emulate \cancel{E}_T , one needs to apply both a scale shift and smearing to the generated \cancel{E}_T value. The \cancel{E}_T scale factor is $\cancel{E}_T(\text{reco})/\cancel{E}_T(\text{gen}) = 0.94$. The value of $\sigma(\cancel{E}_T(\text{reco})/\cancel{E}_T(\text{gen}))$ is about 0.2 at $\cancel{E}_T = 100$ GeV. It falls linearly to about 0.06 at $\cancel{E}_T = 400$ GeV, and it remains at 0.06 for $\cancel{E}_T > 400$ GeV.

In the ANN method, the preselection requirements on H_T and \cancel{E}_T are 400 and 100 GeV, respectively. The signal regions are specified by $350 < \cancel{E}_T < 500$ GeV and $\cancel{E}_T > 500$ GeV together with $z_{\text{ANN}} > 0.4$, where z_{ANN} is a function [48] of n_{jets} , H_T , $\Delta\phi(j_1, j_2)$, and M_T . The efficiency turn-on curve for $z_{\text{ANN}} > 0.4$ is approximated by the parameter values $\epsilon_{\text{plateau}} = 0.98$, $x_{\text{thresh}} = 0.41$, and $\sigma = 0.1$.

With these additional procedures, the emulation of the efficiencies for the L_P and ANN methods is found to be accurate to within $\sim 15\%$, as for the LS method.

Table 13: Efficiency-model parameters for $x \equiv H_T$.

Threshold	$\epsilon_{\text{plateau}}$	$x_{\text{thresh}}[\text{GeV}]$	σ [GeV]
$H_T \geq 400 \text{ GeV}$	1.00	396	65
$H_T \geq 500 \text{ GeV}$	1.00	502	66
$H_T \geq 750 \text{ GeV}$	1.00	760	68
$H_T \geq 1000 \text{ GeV}$	1.00	1013	80

Table 14: Efficiency-model parameters for $x \equiv \cancel{E}_T$.

Threshold	$\epsilon_{\text{plateau}}$	$x_{\text{thresh}} [\text{GeV}]$	σ [GeV]
$\cancel{E}_T \geq 100 \text{ GeV}$	1.00	103	41
$\cancel{E}_T \geq 250 \text{ GeV}$	0.99	266	41
$\cancel{E}_T \geq 350 \text{ GeV}$	0.98	375	45
$\cancel{E}_T \geq 450 \text{ GeV}$	0.97	485	48
$\cancel{E}_T \geq 500 \text{ GeV}$	0.94	537	44
$\cancel{E}_T \geq 550 \text{ GeV}$	0.96	597	59

10 Summary

Using a sample of proton-proton collisions at $\sqrt{s} = 7 \text{ TeV}$ corresponding to an integrated luminosity of 4.98 fb^{-1} , we have performed a search for an excess of events with a single, isolated high- p_T lepton, at least three jets, and large missing transverse momentum. To provide a robust and redundant determination of the SM backgrounds, three methods are used, each of which relies primarily on control samples in the data.

The Lepton Spectrum (LS) method exploits the relationship between two key observables, the lepton p_T distribution and the \cancel{E}_T distribution. In the dominant SM background processes, which have a single, isolated lepton, this connection arises from the fact that the lepton and neutrino are produced together in the two-body decay of the W boson, regardless of whether the W is produced in $t\bar{t}$ or W +jets events. In many SUSY models, however, the \cancel{E}_T is associated with the production of two neutralinos, which decouples \cancel{E}_T from the lepton p_T spectrum. Smaller backgrounds arising from $t\bar{t}$ dilepton events, from $\tau \rightarrow \ell$ decays in $t\bar{t}$ or W +jets events, and from QCD multijet processes are also estimated using control samples in the data. In the sample investigated with this method, at least four jets are required, which helps to suppress the background from W +jets events. Nine signal regions are considered, specified by three thresholds on H_T and three bins of \cancel{E}_T . The observed yields in each region are consistent with the background estimates based on control samples in the data.

The Lepton Projection (L_P) method exploits information on the W -boson polarization in $t\bar{t}$ and W +jets events. The dimensionless L_P variable itself is sensitive to the helicity angle of the lepton from W decay, but it also provides discrimination between signal and background through the ratio of the lepton p_T and the \cancel{E}_T values, which is small in SUSY-like events. The S_T^{lep} variable maps out a diagonal line in the plane of lepton p_T vs. \cancel{E}_T and reflects the W transverse momentum for the boosted W boson. The L_P distributions are studied in bins of S_T^{lep} , and H_T , and at least three jets are required. In each signal region, the data are in agreement with expectations from the SM.

The artificial neural network (ANN) method provides a means to obtain the \cancel{E}_T distribution of background events in data by constructing a neural network variable z_{ANN} , which has a very small correlation with \cancel{E}_T . This variable also provides strong discrimination between signal and background events, so that the background regions do not suffer from large signal contamination in the models considered. A key element of the z_{ANN} variable is the transverse mass of the lepton- \cancel{E}_T system, but additional variables, such as the number of observed jets, play a role as well. In the ANN analysis, no excess of events is observed in the signal regions with respect to the SM background prediction.

Because these methods probe extreme kinematic regions of the background phase space, the use of redundant approaches provides confidence in the results. Although the LS and L_P methods both make use of information on the W -boson polarization in the background, they are based on different kinematic variables and have different signal regions. The LS method breaks the background into several pieces (single lepton, $\tau \rightarrow \ell$, dilepton, and QCD) and provides a direct background prediction for the \cancel{E}_T distribution. In contrast, the L_P method defines a powerful kinematic variable that is used to obtain a global background prediction by extrapolating an overall background shape from a control region into the signal region. The ANN method similarly uses a global approach to estimating the background. The neural-net variable incorporates information used in neither of the other two methods.

The results from each method are interpreted in the context of both the CMSSM and a so-called simplified model, T3w, which has a minimal SUSY particle spectrum. The CMSSM limits exclude gluino masses up to approximately 1.3 TeV in the part of the parameter space in which $m_0 < 800$ GeV, but the bound gradually weakens for larger values of m_0 . For the T3w simplified model, we obtain cross section upper limits as a function of gluino mass. Finally, we provide an approximate model of our signal efficiency that can be used in conjunction with a simple PYTHIA simulation to determine whether other models can be probed by these data.

Acknowledgements

We congratulate our colleagues in the CERN accelerator departments for the excellent performance of the LHC and thank the technical and administrative staffs at CERN and at other CMS institutes for their contributions to the success of the CMS effort. In addition, we gratefully acknowledge the computing centres and personnel of the Worldwide LHC Computing Grid for delivering so effectively the computing infrastructure essential to our analyses. Finally, we acknowledge the enduring support for the construction and operation of the LHC and the CMS detector provided by the following funding agencies: the Austrian Federal Ministry of Science and Research; the Belgian Fonds de la Recherche Scientifique, and Fonds voor Wetenschappelijk Onderzoek; the Brazilian Funding Agencies (CNPq, CAPES, FAPERJ, and FAPESP); the Bulgarian Ministry of Education, Youth and Science; CERN; the Chinese Academy of Sciences, Ministry of Science and Technology, and National Natural Science Foundation of China; the Colombian Funding Agency (COLCIENCIAS); the Croatian Ministry of Science, Education and Sport; the Research Promotion Foundation, Cyprus; the Ministry of Education and Research, Recurrent financing contract SF0690030s09 and European Regional Development Fund, Estonia; the Academy of Finland, Finnish Ministry of Education and Culture, and Helsinki Institute of Physics; the Institut National de Physique Nucléaire et de Physique des Particules / CNRS, and Commissariat à l'Énergie Atomique et aux Énergies Alternatives / CEA, France; the Bundesministerium für Bildung und Forschung, Deutsche Forschungsgemeinschaft, and Helmholtz-Gemeinschaft Deutscher Forschungszentren, Germany; the General Secretariat for Research and Technology, Greece; the National Scientific

Research Foundation, and National Office for Research and Technology, Hungary; the Department of Atomic Energy and the Department of Science and Technology, India; the Institute for Studies in Theoretical Physics and Mathematics, Iran; the Science Foundation, Ireland; the Istituto Nazionale di Fisica Nucleare, Italy; the Korean Ministry of Education, Science and Technology and the World Class University program of NRF, Republic of Korea; the Lithuanian Academy of Sciences; the Mexican Funding Agencies (CINVESTAV, CONACYT, SEP, and UASLP-FAI); the Ministry of Science and Innovation, New Zealand; the Pakistan Atomic Energy Commission; the Ministry of Science and Higher Education and the National Science Centre, Poland; the Fundação para a Ciência e a Tecnologia, Portugal; JINR (Armenia, Belarus, Georgia, Ukraine, Uzbekistan); the Ministry of Education and Science of the Russian Federation, the Federal Agency of Atomic Energy of the Russian Federation, Russian Academy of Sciences, and the Russian Foundation for Basic Research; the Ministry of Science and Technological Development of Serbia; the Secretaría de Estado de Investigación, Desarrollo e Innovación and Programa Consolider-Ingenio 2010, Spain; the Swiss Funding Agencies (ETH Board, ETH Zurich, PSI, SNF, UniZH, Canton Zurich, and SER); the National Science Council, Taipei; the Thailand Center of Excellence in Physics, the Institute for the Promotion of Teaching Science and Technology of Thailand and the National Science and Technology Development Agency of Thailand; the Scientific and Technical Research Council of Turkey, and Turkish Atomic Energy Authority; the Science and Technology Facilities Council, UK; the US Department of Energy, and the US National Science Foundation.

Individuals have received support from the Marie-Curie programme and the European Research Council (European Union); the Leventis Foundation; the A. P. Sloan Foundation; the Alexander von Humboldt Foundation; the Belgian Federal Science Policy Office; the Fonds pour la Formation à la Recherche dans l'Industrie et dans l'Agriculture (FRIA-Belgium); the Agentschap voor Innovatie door Wetenschap en Technologie (IWT-Belgium); the Ministry of Education, Youth and Sports (MEYS) of Czech Republic; the Council of Science and Industrial Research, India; the Compagnia di San Paolo (Torino); and the HOMING PLUS programme of Foundation for Polish Science, cofinanced from European Union, Regional Development Fund.

References

- [1] CMS Collaboration, "Search for supersymmetry in pp collisions at $\sqrt{s} = 7$ TeV in events with a single lepton, jets, and missing transverse momentum", *JHEP* **08** (2011) 156, doi:10.1007/JHEP08(2011)156, arXiv:1107.1870.
- [2] S. P. Martin, "A Supersymmetry primer", (1997). arXiv:hep-ph/9709356.
- [3] J. Wess and B. Zumino, "Supergauge Transformations in Four-Dimensions", *Nucl. Phys. B* **70** (1974) 39, doi:10.1016/0550-3213(74)90355-1.
- [4] H. P. Nilles, "Supersymmetry, Supergravity and Particle Physics", *Phys. Rept.* **110** (1984) 1, doi:10.1016/0370-1573(84)90008-5.
- [5] H. E. Haber and G. L. Kane, "The Search for Supersymmetry: Probing Physics Beyond the Standard Model", *Phys. Rept.* **117** (1985) 75, doi:10.1016/0370-1573(85)90051-1.
- [6] R. Barbieri, S. Ferrara, and C. A. Savoy, "Gauge Models with Spontaneously Broken Local Supersymmetry", *Phys. Lett. B* **119** (1982) 343, doi:10.1016/0370-2693(82)90685-2.

- [7] S. Dawson, E. Eichten, and C. Quigg, "Search for Supersymmetric Particles in Hadron - Hadron Collisions", *Phys. Rev. D* **31** (1985) 1581, doi:10.1103/PhysRevD.31.1581.
- [8] G. R. Farrar and P. Fayet, "Phenomenology of the production, decay, and detection of new hadronic states associated with supersymmetry", *Phys. Lett. B* **76** (1978) 575, doi:10.1016/0370-2693(78)90858-4.
- [9] J. L. Feng, "Dark Matter Candidates from Particle Physics and Methods of Detection", *Ann. Rev. Astron. Astrophys.* **48** (2010) 495, doi:10.1146/annurev-astro-082708-101659, arXiv:1003.0904.
- [10] G. L. Kane et al., "Study of constrained minimal supersymmetry", *Phys. Rev. D* **49** (1994) 6173, doi:10.1103/PhysRevD.49.6173, arXiv:hep-ph/9312272.
- [11] A. H. Chamseddine, R. L. Arnowitt, and P. Nath, "Locally Supersymmetric Grand Unification", *Phys. Rev. Lett.* **49** (1982) 970, doi:10.1103/PhysRevLett.49.970.
- [12] N. Arkani-Hamed et al., "MARMOSSET: The Path from LHC Data to the New Standard Model via On-Shell Effective Theories", (2007). arXiv:hep-ph/0703088.
- [13] J. Alwall, P. Schuster, and N. Toro, "Simplified Models for a First Characterization of New Physics at the LHC", *Phys. Rev. D* **79** (2009) 075020, doi:10.1103/PhysRevD.79.075020, arXiv:0810.3921.
- [14] J. Alwall et al., "Model-Independent Jets plus Missing Energy Searches", *Phys. Rev. D* **79** (2009) 015005, doi:10.1103/PhysRevD.79.015005, arXiv:0809.3264.
- [15] LHC New Physics Working Group Collaboration, "Simplified Models for LHC New Physics Searches", *J. Phys. G* **39** (2012) 105005, doi:10.1088/0954-3899/39/10/105005, arXiv:1105.2838.
- [16] CMS Collaboration, "Search for supersymmetry in final states with a single lepton, b-quark jets, and missing transverse energy in proton-proton collisions at $\sqrt{s} = 7$ TeV", (2012). arXiv:1211.3143. Submitted to *Phys. Rev. D*.
- [17] ATLAS Collaboration, "Search for supersymmetry using final states with one lepton, jets, and missing transverse momentum with the ATLAS detector in $\sqrt{s} = 7$ TeV pp collisions", *Phys. Rev. Lett.* **106** (2011) 131802, doi:10.1103/PhysRevLett.106.131802, arXiv:1102.2357.
- [18] ATLAS Collaboration, "Search for supersymmetry in final states with jets, missing transverse momentum and one isolated lepton in $\sqrt{s} = 7$ TeV pp collisions using 1 fb⁻¹ of ATLAS data", *Phys. Rev. D* **85** (2012) 012006, doi:10.1103/PhysRevD.85.012006, arXiv:1109.6606.
- [19] ATLAS Collaboration, "Further search for supersymmetry at $\sqrt{s} = 7$ TeV in final states with jets, missing transverse momentum and isolated leptons with the ATLAS detector", *Phys. Rev. D* **86** (2012) 092002, doi:10.1103/PhysRevD.86.092002, arXiv:1208.4688.
- [20] CMS Collaboration, "Search for Physics Beyond the Standard Model in Opposite-Sign Dilepton Events at $\sqrt{s} = 7$ TeV", *JHEP* **06** (2011) 026, doi:10.1007/JHEP06(2011)026, arXiv:1103.1348.

- [21] CMS Collaboration, “Measurement of the Polarization of W Bosons with Large Transverse Momenta in W+Jets Events at the LHC”, *Phys. Rev. Lett.* **107** (2011) 021802, doi:10.1103/PhysRevLett.107.021802, arXiv:1104.3829.
- [22] CMS Collaboration, “The CMS experiment at the CERN LHC”, *JINST* **3** (2008) S08004, doi:10.1088/1748-0221/3/08/S08004.
- [23] CMS Collaboration, “Particle-Flow Event Reconstruction in CMS and Performance for Jets, Taus, and E_T^{miss} ”, CMS Physics Analysis Summary CMS-PAS-PFT-09-001, (2009).
- [24] CMS Collaboration, “Commissioning of the Particle-Flow Reconstruction in Minimum-Bias and Jet Events from pp Collisions at 7 TeV”, CMS Physics Analysis Summary CMS-PAS-PFT-10-002, (2010).
- [25] GEANT4 Collaboration, “GEANT4—a simulation toolkit”, *Nucl. Instrum. Meth. A* **506** (2003) 250, doi:10.1016/S0168-9002(03)01368-8.
- [26] T. Sjöstrand, S. Mrenna, and P. Z. Skands, “PYTHIA 6.4 physics and manual”, *JHEP* **05** (2006) 026, doi:10.1088/1126-6708/2006/05/026, arXiv:hep-ph/0603175.
- [27] R. Field, “Early LHC Underlying Event Data — Findings and Surprises”, (2010). arXiv:1010.3558.
- [28] J. Alwall et al., “MadGraph 5: going beyond”, *JHEP* **06** (2011) 128, doi:10.1007/JHEP06(2011)128, arXiv:1106.0522.
- [29] S. Frixione, P. Nason, and C. Oleari, “Matching NLO QCD computations with Parton Shower simulations: the POWHEG method”, *JHEP* **11** (2007) 070, doi:10.1088/1126-6708/2007/11/070, arXiv:0709.2092.
- [30] CMS Collaboration, “CMS technical design report, volume II: Physics performance”, *J. Phys. G* **34** (2007) 995, doi:10.1088/0954-3899/34/6/S01.
- [31] CMS Collaboration, “The fast simulation of the CMS detector at LHC”, *J. Phys. Conf. Ser.* **331** (2011) 032049, doi:10.1088/1742-6596/331/3/032049.
- [32] A. Czarnecki, J. G. Korner, and J. H. Piclum, “Helicity fractions of W bosons from top quark decays at NNLO in QCD”, *Phys. Rev. D* **81** (2010) 111503, doi:10.1103/PhysRevD.81.111503, arXiv:1005.2625.
- [33] ATLAS Collaboration, “Measurement of the W boson polarization in top quark decays with the ATLAS detector”, *JHEP* **06** (2012) 088, doi:10.1007/JHEP06(2012)088, arXiv:1205.2484.
- [34] ATLAS Collaboration, “Measurement of the polarisation of W bosons produced with large transverse momentum in pp collisions at $\sqrt{s} = 7$ TeV with the ATLAS experiment”, *Eur. Phys. J. C* **72** (2012) 2001, doi:10.1140/epjc/s10052-012-2001-6, arXiv:1203.2165.
- [35] M. L. Mangano et al., “ALPGEN, a generator for hard multiparton processes in hadronic collisions”, *JHEP* **07** (2003) 001, doi:10.1088/1126-6708/2003/07/001, arXiv:hep-ph/0206293.
- [36] Z. Bern et al., “Left-Handed W Bosons at the LHC”, *Phys. Rev. D* **84** (2011) 034008, doi:10.1103/PhysRevD.84.034008, arXiv:1103.5445.

- [37] M. Cacciari, G. P. Salam, and G. Soyez, “The Anti-k(t) jet clustering algorithm”, *JHEP* **04** (2008) 063, doi:10.1088/1126-6708/2008/04/063, arXiv:0802.1189.
- [38] CMS Collaboration, “Determination of Jet Energy Calibration and Transverse Momentum Resolution in CMS”, *JINST* **6** (2011) P11002, doi:10.1088/1748-0221/6/11/P11002, arXiv:1107.4277.
- [39] CMS Collaboration, “Performance of CMS muon reconstruction in pp collision events at $\sqrt{s} = 7$ TeV”, *JINST* **7** (2012) P10002, doi:10.1088/1748-0221/7/10/P10002, arXiv:1206.4071.
- [40] CMS Collaboration, “Electron Reconstruction and Identification at $\sqrt{s} = 7$ TeV”, CMS Physics Analysis Summary CMS-PAS-EGM-10-004, (2010).
- [41] V. Pavlunin, “Modeling missing transverse energy in V+jets at CERN LHC”, *Phys. Rev. D* **81** (2010) 035005, doi:10.1103/PhysRevD.81.035005, arXiv:0906.5016.
- [42] P. Speckmayer et al., “The toolkit for multivariate data analysis, TMVA 4”, *J. Phys. Conf. Ser.* **219** (2010) 032057, doi:10.1088/1742-6596/219/3/032057.
- [43] CMS Collaboration, “Measuring Electron Efficiencies at CMS with Early Data”, CMS Physics Analysis Summary CMS-PAS-EGM-07-001, (2008).
- [44] CMS Collaboration, “Absolute Calibration of the Luminosity Measurement at CMS: Winter 2012 Update”, CMS Physics Analysis Summary CMS-PAS-SMP-12-008, (2012).
- [45] T. Junk, “Confidence level computation for combining searches with small statistics”, *Nucl. Instrum. Meth. A* **434** (1999) 435, doi:10.1016/S0168-9002(99)00498-2, arXiv:hep-ex/9902006.
- [46] M. Krämer et al., “Supersymmetry production cross sections in pp collisions at $\sqrt{s} = 7$ TeV”, (2012). arXiv:1206.2892.
- [47] K. Matchev and R. Remington, “Updated templates for the interpretation of LHC results on supersymmetry in the context of mSUGRA”, (2012). arXiv:1202.6580.
- [48] See supplementary material at [URL will be inserted by journal] for a C++ function that evaluates the artificial neural network based on the values of the four input variables.

A The CMS Collaboration

Yerevan Physics Institute, Yerevan, Armenia

S. Chatrchyan, V. Khachatryan, A.M. Sirunyan, A. Tumasyan

Institut für Hochenergiephysik der OeAW, Wien, Austria

W. Adam, E. Aguilo, T. Bergauer, M. Dragicevic, J. Erö, C. Fabjan¹, M. Friedl, R. Frühwirth¹, V.M. Ghete, J. Hammer, N. Hörmann, J. Hrubec, M. Jeitler¹, W. Kiesenhofer, V. Knünz, M. Krammer¹, I. Krätschmer, D. Liko, I. Mikulec, M. Pernicka[†], B. Rahbaran, C. Rohringer, H. Rohringer, R. Schöfbeck, J. Strauss, A. Taurok, W. Waltenberger, G. Walzel, E. Widl, C.-E. Wulz¹

National Centre for Particle and High Energy Physics, Minsk, Belarus

V. Mossolov, N. Shumeiko, J. Suarez Gonzalez

Universiteit Antwerpen, Antwerpen, Belgium

M. Bansal, S. Bansal, T. Cornelis, E.A. De Wolf, X. Janssen, S. Luyckx, L. Mucibello, S. Ochesanu, B. Roland, R. Rougny, M. Selvaggi, Z. Staykova, H. Van Haevermaet, P. Van Mechelen, N. Van Remortel, A. Van Spillbeeck

Vrije Universiteit Brussel, Brussel, Belgium

F. Blekman, S. Blyweert, J. D'Hondt, R. Gonzalez Suarez, A. Kalogeropoulos, M. Maes, A. Olbrechts, W. Van Doninck, P. Van Mulders, G.P. Van Onsem, I. Villella

Université Libre de Bruxelles, Bruxelles, Belgium

B. Clerbaux, G. De Lentdecker, V. Dero, A.P.R. Gay, T. Hreus, A. Léonard, P.E. Marage, A. Mohammadi, T. Reis, L. Thomas, G. Vander Marcken, C. Vander Velde, P. Vanlaer, J. Wang

Ghent University, Ghent, Belgium

V. Adler, K. Beernaert, A. Cimmino, S. Costantini, G. Garcia, M. Grunewald, B. Klein, J. Lellouch, A. Marinov, J. McCartin, A.A. Ocampo Rios, D. Ryckbosch, N. Strobbe, F. Thyssen, M. Tytgat, P. Verwilligen, S. Walsh, E. Yazgan, N. Zaganidis

Université Catholique de Louvain, Louvain-la-Neuve, Belgium

S. Basegmez, G. Bruno, R. Castello, L. Ceard, C. Delaere, T. du Pree, D. Favart, L. Forthomme, A. Giammanco², J. Hollar, V. Lemaître, J. Liao, O. Militaru, C. Nuttens, D. Pagano, A. Pin, K. Piotrkowski, N. Schul, J.M. Vizan Garcia

Université de Mons, Mons, Belgium

N. Belyi, T. Caebergs, E. Daubie, G.H. Hammad

Centro Brasileiro de Pesquisas Físicas, Rio de Janeiro, Brazil

G.A. Alves, M. Correa Martins Junior, T. Martins, M.E. Pol, M.H.G. Souza

Universidade do Estado do Rio de Janeiro, Rio de Janeiro, Brazil

W.L. Aldá Júnior, W. Carvalho, A. Custódio, E.M. Da Costa, D. De Jesus Damiao, C. De Oliveira Martins, S. Fonseca De Souza, D. Matos Figueiredo, L. Mundim, H. Nogima, W.L. Prado Da Silva, A. Santoro, L. Soares Jorge, A. Sznajder

Universidade Estadual Paulista ^a, Universidade Federal do ABC ^b, São Paulo, Brazil

T.S. Anjos^b, C.A. Bernardes^b, F.A. Dias^{a,3}, T.R. Fernandez Perez Tomei^a, E.M. Gregores^b, C. Lagana^a, F. Marinho^a, P.G. Mercadante^b, S.F. Novaes^a, Sandra S. Padula^a

Institute for Nuclear Research and Nuclear Energy, Sofia, Bulgaria

V. Genchev⁴, P. Iaydjiev⁴, S. Piperov, M. Rodozov, S. Stoykova, G. Sultanov, V. Tcholakov, R. Trayanov, M. Vutova

University of Sofia, Sofia, Bulgaria

A. Dimitrov, R. Hadjiiska, V. Kozhuharov, L. Litov, B. Pavlov, P. Petkov

Institute of High Energy Physics, Beijing, China

J.G. Bian, G.M. Chen, H.S. Chen, C.H. Jiang, D. Liang, S. Liang, X. Meng, J. Tao, J. Wang, X. Wang, Z. Wang, H. Xiao, M. Xu, J. Zang, Z. Zhang

State Key Lab. of Nucl. Phys. and Tech., Peking University, Beijing, China

C. Asawatrangkuldee, Y. Ban, Y. Guo, W. Li, S. Liu, Y. Mao, S.J. Qian, H. Teng, D. Wang, L. Zhang, W. Zou

Universidad de Los Andes, Bogota, Colombia

C. Avila, J.P. Gomez, B. Gomez Moreno, A.F. Osorio Oliveros, J.C. Sanabria

Technical University of Split, Split, Croatia

N. Godinovic, D. Lelas, R. Plestina⁵, D. Polic, I. Puljak⁴

University of Split, Split, Croatia

Z. Antunovic, M. Kovac

Institute Rudjer Boskovic, Zagreb, Croatia

V. Brigljevic, S. Duric, K. Kadija, J. Luetic, S. Morovic

University of Cyprus, Nicosia, Cyprus

A. Attikis, M. Galanti, G. Mavromanolakis, J. Mousa, C. Nicolaou, F. Ptochos, P.A. Razis

Charles University, Prague, Czech Republic

M. Finger, M. Finger Jr.

Academy of Scientific Research and Technology of the Arab Republic of Egypt, Egyptian Network of High Energy Physics, Cairo, Egypt

Y. Assran⁶, S. Elgammal⁷, A. Ellithi Kamel⁸, M.A. Mahmoud⁹, A. Radi^{10,11}

National Institute of Chemical Physics and Biophysics, Tallinn, Estonia

M. Kadastik, M. Müntel, M. Raidal, L. Rebane, A. Tiko

Department of Physics, University of Helsinki, Helsinki, Finland

P. Eerola, G. Fedi, M. Voutilainen

Helsinki Institute of Physics, Helsinki, Finland

J. Härkönen, A. Heikkinen, V. Karimäki, R. Kinnunen, M.J. Kortelainen, T. Lampén, K. Lassila-Perini, S. Lehti, T. Lindén, P. Luukka, T. Mäenpää, T. Peltola, E. Tuominen, J. Tuominiemi, E. Tuovinen, D. Ungaro, L. Wendland

Lappeenranta University of Technology, Lappeenranta, Finland

K. Banzuzi, A. Karjalainen, A. Korpela, T. Tuuva

DSM/IRFU, CEA/Saclay, Gif-sur-Yvette, France

M. Besancon, S. Choudhury, M. Dejardin, D. Denegri, B. Fabbro, J.L. Faure, F. Ferri, S. Ganjour, A. Givernaud, P. Gras, G. Hamel de Monchenault, P. Jarry, E. Locci, J. Malcles, L. Millischer, A. Nayak, J. Rander, A. Rosowsky, I. Shreyber, M. Titov

Laboratoire Leprince-Ringuet, Ecole Polytechnique, IN2P3-CNRS, Palaiseau, France

S. Baffioni, F. Beaudette, L. Benhabib, L. Bianchini, M. Bluj¹², C. Broutin, P. Busson, C. Charlot, N. Daci, T. Dahms, M. Dalchenko, L. Dobrzynski, R. Granier de Cassagnac, M. Haguenaer, P. Miné, C. Mironov, I.N. Naranjo, M. Nguyen, C. Ochando, P. Paganini, D. Sabes, R. Salerno, Y. Sirois, C. Veelken, A. Zabi

Institut Pluridisciplinaire Hubert Curien, Université de Strasbourg, Université de Haute Alsace Mulhouse, CNRS/IN2P3, Strasbourg, France

J.-L. Agram¹³, J. Andrea, D. Bloch, D. Bodin, J.-M. Brom, M. Cardaci, E.C. Chabert, C. Collard, E. Conte¹³, F. Drouhin¹³, C. Ferro, J.-C. Fontaine¹³, D. Gelé, U. Goerlach, P. Juillot, A.-C. Le Bihan, P. Van Hove

Centre de Calcul de l'Institut National de Physique Nucleaire et de Physique des Particules, CNRS/IN2P3, Villeurbanne, France

F. Fassi, D. Mercier

Université de Lyon, Université Claude Bernard Lyon 1, CNRS-IN2P3, Institut de Physique Nucléaire de Lyon, Villeurbanne, France

S. Beauceron, N. Beaupere, O. Bondu, G. Boudoul, J. Chasserat, R. Chierici⁴, D. Contardo, P. Depasse, H. El Mamouni, J. Fay, S. Gascon, M. Gouzevitch, B. Ille, T. Kurca, M. Lethuillier, L. Mirabito, S. Perries, L. Sgandurra, V. Sordini, Y. Tschudi, P. Verdier, S. Viret

Institute of High Energy Physics and Informatization, Tbilisi State University, Tbilisi, Georgia

Z. Tsamalaidze¹⁴

RWTH Aachen University, I. Physikalisches Institut, Aachen, Germany

G. Anagnostou, C. Autermann, S. Beranek, M. Edelhoff, L. Feld, N. Heracleous, O. Hindrichs, R. Jussen, K. Klein, J. Merz, A. Ostapchuk, A. Perieanu, F. Raupach, J. Sammet, S. Schael, D. Sprenger, H. Weber, B. Wittmer, V. Zhukov¹⁵

RWTH Aachen University, III. Physikalisches Institut A, Aachen, Germany

M. Ata, J. Caudron, E. Dietz-Laursonn, D. Duchardt, M. Erdmann, R. Fischer, A. Güth, T. Hebbeker, C. Heidemann, K. Hoepfner, D. Klingebiel, P. Kreuzer, M. Merschmeyer, A. Meyer, M. Olschewski, P. Papacz, H. Pieta, H. Reithler, S.A. Schmitz, L. Sonnenschein, J. Steggemann, D. Teyssier, M. Weber

RWTH Aachen University, III. Physikalisches Institut B, Aachen, Germany

M. Bontenackels, V. Cherepanov, Y. Erdogan, G. Flügge, H. Geenen, M. Geisler, W. Haj Ahmad, F. Hoehle, B. Kargoll, T. Kress, Y. Kuessel, J. Lingemann⁴, A. Nowack, L. Perchalla, O. Pooth, P. Sauerland, A. Stahl

Deutsches Elektronen-Synchrotron, Hamburg, Germany

M. Aldaya Martin, J. Behr, W. Behrenhoff, U. Behrens, M. Bergholz¹⁶, A. Bethani, K. Borras, A. Burgmeier, A. Cakir, L. Calligaris, A. Campbell, E. Castro, F. Costanza, D. Dammann, C. Diez Pardos, G. Eckerlin, D. Eckstein, G. Flucke, A. Geiser, I. Glushkov, P. Gunnellini, S. Habib, J. Hauk, G. Hellwig, H. Jung, M. Kasemann, P. Katsas, C. Kleinwort, H. Kluge, A. Knutsson, M. Krämer, D. Krücker, E. Kuznetsova, W. Lange, W. Lohmann¹⁶, B. Lutz, R. Mankel, I. Marfin, M. Marienfeld, I.-A. Melzer-Pellmann, A.B. Meyer, J. Mnich, A. Mussgiller, S. Naumann-Emme, O. Novgorodova, J. Olzem, H. Perrey, A. Petrukhin, D. Pitzl, A. Raspereza, P.M. Ribeiro Cipriano, C. Riedl, E. Ron, M. Rosin, J. Salfeld-Nebgen, R. Schmidt¹⁶, T. Schoerner-Sadenius, N. Sen, A. Spiridonov, M. Stein, R. Walsh, C. Wissing

University of Hamburg, Hamburg, Germany

V. Blobel, J. Draeger, H. Enderle, J. Erfle, U. Gebbert, M. Görner, T. Hermanns, R.S. Höing, K. Kaschube, G. Kaussen, H. Kirschenmann, R. Klanner, J. Lange, B. Mura, F. Nowak, T. Peiffer, N. Pietsch, D. Rathjens, C. Sander, H. Schettler, P. Schleper, E. Schlieckau, A. Schmidt, M. Schröder, T. Schum, M. Seidel, J. Sibille¹⁷, V. Sola, H. Stadie, G. Steinbrück, J. Thomsen, L. Vanelderden

Institut für Experimentelle Kernphysik, Karlsruhe, Germany

C. Barth, J. Berger, C. Böser, T. Chwalek, W. De Boer, A. Descroix, A. Dierlamm, M. Feindt, M. Guthoff⁴, C. Hackstein, F. Hartmann, T. Hauth⁴, M. Heinrich, H. Held, K.H. Hoffmann, U. Husemann, I. Katkov¹⁵, J.R. Komaragiri, P. Lobelle Pardo, D. Martschei, S. Mueller, Th. Müller, M. Niegel, A. Nürnberg, O. Oberst, A. Oehler, J. Ott, G. Quast, K. Rabbertz, F. Ratnikov, N. Ratnikova, S. Röcker, F.-P. Schilling, G. Schott, H.J. Simonis, F.M. Stober, D. Troendle, R. Ulrich, J. Wagner-Kuhr, S. Wayand, T. Weiler, M. Zeise

Institute of Nuclear Physics "Demokritos", Aghia Paraskevi, Greece

G. Daskalakis, T. Gerasis, S. Kesisoglou, A. Kyriakis, D. Loukas, I. Manolakos, A. Markou, C. Markou, C. Mavrommatis, E. Ntomari

University of Athens, Athens, Greece

L. Gouskos, T.J. Mertzimekis, A. Panagiotou, N. Saoulidou

University of Ioánnina, Ioánnina, Greece

I. Evangelou, C. Foudas, P. Kokkas, N. Manthos, I. Papadopoulos, V. Patras

KFKI Research Institute for Particle and Nuclear Physics, Budapest, Hungary

G. Bencze, C. Hajdu, P. Hidas, D. Horvath¹⁸, F. Sikler, V. Veszpremi, G. Vesztergombi¹⁹

Institute of Nuclear Research ATOMKI, Debrecen, Hungary

N. Beni, S. Czellar, J. Molnar, J. Palinkas, Z. Szillasi

University of Debrecen, Debrecen, Hungary

J. Karancsi, P. Raics, Z.L. Trocsanyi, B. Ujvari

Panjab University, Chandigarh, India

S.B. Beri, V. Bhatnagar, N. Dhingra, R. Gupta, M. Kaur, M.Z. Mehta, N. Nishu, L.K. Saini, A. Sharma, J.B. Singh

University of Delhi, Delhi, India

Ashok Kumar, Arun Kumar, S. Ahuja, A. Bhardwaj, B.C. Choudhary, S. Malhotra, M. Naimuddin, K. Ranjan, V. Sharma, R.K. Shivpuri

Saha Institute of Nuclear Physics, Kolkata, India

S. Banerjee, S. Bhattacharya, S. Dutta, B. Gomber, Sa. Jain, Sh. Jain, R. Khurana, S. Sarkar, M. Sharan

Bhabha Atomic Research Centre, Mumbai, India

A. Abdulsalam, R.K. Choudhury, D. Dutta, S. Kailas, V. Kumar, P. Mehta, A.K. Mohanty⁴, L.M. Pant, P. Shukla

Tata Institute of Fundamental Research - EHEP, Mumbai, India

T. Aziz, S. Ganguly, M. Guchait²⁰, M. Maity²¹, G. Majumder, K. Mazumdar, G.B. Mohanty, B. Parida, K. Sudhakar, N. Wickramage

Tata Institute of Fundamental Research - HECR, Mumbai, India

S. Banerjee, S. Dugad

Institute for Research in Fundamental Sciences (IPM), Tehran, Iran

H. Arfaei²², H. Bakhshiansohi, S.M. Etesami²³, A. Fahim²², M. Hashemi, H. Hesari, A. Jafari, M. Khakzad, M. Mohammadi Najafabadi, S. Paktinat Mehdiabadi, B. Safarzadeh²⁴, M. Zeinali

INFN Sezione di Bari ^a, Università di Bari ^b, Politecnico di Bari ^c, Bari, Italy

M. Abbrescia^{a,b}, L. Barbone^{a,b}, C. Calabria^{a,b,4}, S.S. Chhibra^{a,b}, A. Colaleo^a, D. Creanza^{a,c}, N. De

Filippis^{a,c,4}, M. De Palma^{a,b}, L. Fiore^a, G. Iaselli^{a,c}, G. Maggi^{a,c}, M. Maggi^a, B. Marangelli^{a,b}, S. My^{a,c}, S. Nuzzo^{a,b}, N. Pacifico^{a,b}, A. Pompili^{a,b}, G. Pugliese^{a,c}, G. Selvaggi^{a,b}, L. Silvestris^a, G. Singh^{a,b}, R. Venditti^{a,b}, G. Zito^a

INFN Sezione di Bologna ^a, Università di Bologna ^b, Bologna, Italy

G. Abbiendi^a, A.C. Benvenuti^a, D. Bonacorsi^{a,b}, S. Braibant-Giacomelli^{a,b}, L. Brigliadori^{a,b}, P. Capiluppi^{a,b}, A. Castro^{a,b}, F.R. Cavallo^a, M. Cuffiani^{a,b}, G.M. Dallavalle^a, F. Fabbri^a, A. Fanfani^{a,b}, D. Fasanella^{a,b,4}, P. Giacomelli^a, C. Grandi^a, L. Guiducci^{a,b}, S. Marcellini^a, G. Masetti^a, M. Meneghelli^{a,b,4}, A. Montanari^a, F.L. Navarria^{a,b}, F. Odorici^a, A. Perrotta^a, F. Primavera^{a,b}, A.M. Rossi^{a,b}, T. Rovelli^{a,b}, G.P. Siroli^{a,b}, R. Travaglini^{a,b}

INFN Sezione di Catania ^a, Università di Catania ^b, Catania, Italy

S. Albergo^{a,b}, G. Cappello^{a,b}, M. Chiorboli^{a,b}, S. Costa^{a,b}, R. Potenza^{a,b}, A. Tricomi^{a,b}, C. Tuve^{a,b}

INFN Sezione di Firenze ^a, Università di Firenze ^b, Firenze, Italy

G. Barbagli^a, V. Ciulli^{a,b}, C. Civinini^a, R. D'Alessandro^{a,b}, E. Focardi^{a,b}, S. Frosali^{a,b}, E. Gallo^a, S. Gonzi^{a,b}, M. Meschini^a, S. Paoletti^a, G. Sguazzoni^a, A. Tropiano^{a,b}

INFN Laboratori Nazionali di Frascati, Frascati, Italy

L. Benussi, S. Bianco, S. Colafranceschi²⁵, F. Fabbri, D. Piccolo

INFN Sezione di Genova ^a, Università di Genova ^b, Genova, Italy

P. Fabbricatore^a, R. Musenich^a, S. Tosi^{a,b}

INFN Sezione di Milano-Bicocca ^a, Università di Milano-Bicocca ^b, Milano, Italy

A. Benaglia^{a,b}, F. De Guio^{a,b}, L. Di Matteo^{a,b,4}, S. Fiorendi^{a,b}, S. Gennai^{a,4}, A. Ghezzi^{a,b}, S. Malvezzi^a, R.A. Manzoni^{a,b}, A. Martelli^{a,b}, A. Massironi^{a,b,4}, D. Menasce^a, L. Moroni^a, M. Paganoni^{a,b}, D. Pedrini^a, S. Ragazzi^{a,b}, N. Redaelli^a, S. Sala^a, T. Tabarelli de Fatis^{a,b}

INFN Sezione di Napoli ^a, Università di Napoli 'Federico II' ^b, Università della Basilicata (Potenza) ^c, Università G. Marconi (Roma) ^d, Napoli, Italy

S. Buontempo^a, C.A. Carrillo Montoya^a, N. Cavallo^{a,c}, A. De Cosa^{a,b,4}, O. Dogangun^{a,b}, F. Fabozzi^{a,c}, A.O.M. Iorio^{a,b}, L. Lista^a, S. Meola^{a,d,26}, M. Merola^a, P. Paolucci^{a,4}

INFN Sezione di Padova ^a, Università di Padova ^b, Università di Trento (Trento) ^c, Padova, Italy

P. Azzi^a, N. Bacchetta^{a,4}, D. Bisello^{a,b}, A. Branca^{a,b,4}, R. Carlin^{a,b}, P. Checchia^a, T. Dorigo^a, U. Dosselli^a, F. Gasparini^{a,b}, U. Gasparini^{a,b}, A. Gozzelino^a, K. Kanishchev^{a,c}, S. Lacaprara^a, I. Lazzizzera^{a,c}, M. Margoni^{a,b}, A.T. Meneguzzo^{a,b}, J. Pazzini^{a,b}, N. Pozzobon^{a,b}, P. Ronchese^{a,b}, F. Simonetto^{a,b}, E. Torassa^a, M. Tosi^{a,b}, S. Vanini^{a,b}, P. Zotto^{a,b}, G. Zumerle^{a,b}

INFN Sezione di Pavia ^a, Università di Pavia ^b, Pavia, Italy

M. Gabusi^{a,b}, S.P. Ratti^{a,b}, C. Riccardi^{a,b}, P. Torre^{a,b}, P. Vitulo^{a,b}

INFN Sezione di Perugia ^a, Università di Perugia ^b, Perugia, Italy

M. Biasini^{a,b}, G.M. Bilei^a, L. Fanò^{a,b}, P. Lariccia^{a,b}, G. Mantovani^{a,b}, M. Menichelli^a, A. Nappi^{a,b,†}, F. Romeo^{a,b}, A. Saha^a, A. Santocchia^{a,b}, A. Spiezia^{a,b}, S. Taroni^{a,b}

INFN Sezione di Pisa ^a, Università di Pisa ^b, Scuola Normale Superiore di Pisa ^c, Pisa, Italy

P. Azzurri^{a,c}, G. Bagliesi^a, J. Bernardini^a, T. Boccali^a, G. Broccolo^{a,c}, R. Castaldi^a, R.T. D'Agnolo^{a,c,4}, R. Dell'Orso^a, F. Fiori^{a,b,4}, L. Foà^{a,c}, A. Giassi^a, A. Kraan^a, F. Ligabue^{a,c}, T. Lomtadze^a, L. Martini^{a,27}, A. Messineo^{a,b}, F. Palla^a, A. Rizzi^{a,b}, A.T. Serban^{a,28}, P. Spagnolo^a, P. Squillacioti^{a,4}, R. Tenchini^a, G. Tonelli^{a,b}, A. Venturi^a, P.G. Verdini^a

INFN Sezione di Roma ^a, Università di Roma ^b, Roma, Italy

L. Barone^{a,b}, F. Cavallari^a, D. Del Re^{a,b}, M. Diemoz^a, C. Fanelli^{a,b}, M. Grassi^{a,b,4}, E. Longo^{a,b}, P. Meridiani^{a,4}, F. Micheli^{a,b}, S. Nourbakhsh^{a,b}, G. Organtini^{a,b}, R. Paramatti^a, S. Rahatlou^{a,b}, M. Sigamani^a, L. Soffi^{a,b}

INFN Sezione di Torino ^a, Università di Torino ^b, Università del Piemonte Orientale (Novara) ^c, Torino, Italy

N. Amapane^{a,b}, R. Arcidiacono^{a,c}, S. Argiro^{a,b}, M. Arneodo^{a,c}, C. Biino^a, N. Cartiglia^a, M. Costa^{a,b}, N. Demaria^a, C. Mariotti^{a,4}, S. Maselli^a, E. Migliore^{a,b}, V. Monaco^{a,b}, M. Musich^{a,4}, M.M. Obertino^{a,c}, N. Pastrone^a, M. Pelliccioni^a, A. Potenza^{a,b}, A. Romero^{a,b}, M. Ruspa^{a,c}, R. Sacchi^{a,b}, A. Solano^{a,b}, A. Staiano^a, A. Vilela Pereira^a

INFN Sezione di Trieste ^a, Università di Trieste ^b, Trieste, Italy

S. Belforte^a, V. Candolise^{a,b}, M. Casarsa^a, F. Cossutti^a, G. Della Ricca^{a,b}, B. Gobbo^a, M. Marone^{a,b,4}, D. Montanino^{a,b,4}, A. Penzo^a, A. Schizzi^{a,b}

Kangwon National University, Chunchon, Korea

S.G. Heo, T.Y. Kim, S.K. Nam

Kyungpook National University, Daegu, Korea

S. Chang, D.H. Kim, G.N. Kim, D.J. Kong, H. Park, S.R. Ro, D.C. Son, T. Son

Chonnam National University, Institute for Universe and Elementary Particles, Kwangju, Korea

J.Y. Kim, Zero J. Kim, S. Song

Korea University, Seoul, Korea

S. Choi, D. Gyun, B. Hong, M. Jo, H. Kim, T.J. Kim, K.S. Lee, D.H. Moon, S.K. Park

University of Seoul, Seoul, Korea

M. Choi, J.H. Kim, C. Park, I.C. Park, S. Park, G. Ryu

Sungkyunkwan University, Suwon, Korea

Y. Cho, Y. Choi, Y.K. Choi, J. Goh, M.S. Kim, E. Kwon, B. Lee, J. Lee, S. Lee, H. Seo, I. Yu

Vilnius University, Vilnius, Lithuania

M.J. Bilinskas, I. Grigelionis, M. Janulis, A. Juodagalvis

Centro de Investigacion y de Estudios Avanzados del IPN, Mexico City, Mexico

H. Castilla-Valdez, E. De La Cruz-Burelo, I. Heredia-de La Cruz, R. Lopez-Fernandez, R. Magaña Villalba, J. Martínez-Ortega, A. Sanchez-Hernandez, L.M. Villasenor-Cendejas

Universidad Iberoamericana, Mexico City, Mexico

S. Carrillo Moreno, F. Vazquez Valencia

Benemerita Universidad Autonoma de Puebla, Puebla, Mexico

H.A. Salazar Ibarguen

Universidad Autónoma de San Luis Potosí, San Luis Potosí, Mexico

E. Casimiro Linares, A. Morelos Pineda, M.A. Reyes-Santos

University of Auckland, Auckland, New Zealand

D. Krofcheck

University of Canterbury, Christchurch, New Zealand

A.J. Bell, P.H. Butler, R. Doesburg, S. Reucroft, H. Silverwood

National Centre for Physics, Quaid-I-Azam University, Islamabad, Pakistan

M. Ahmad, M.H. Ansari, M.I. Asghar, J. Butt, H.R. Hoorani, S. Khalid, W.A. Khan, T. Khurshid, S. Qazi, M.A. Shah, M. Shoaib

National Centre for Nuclear Research, Swierk, Poland

H. Bialkowska, B. Boimska, T. Frueboes, R. Gokieli, M. Górski, M. Kazana, K. Nawrocki, K. Romanowska-Rybinska, M. Szleper, G. Wrochna, P. Zalewski

Institute of Experimental Physics, Faculty of Physics, University of Warsaw, Warsaw, Poland

G. Brona, K. Bunkowski, M. Cwiok, W. Dominik, K. Doroba, A. Kalinowski, M. Konecki, J. Krolikowski

Laboratório de Instrumentação e Física Experimental de Partículas, Lisboa, Portugal

N. Almeida, P. Bargassa, A. David, P. Faccioli, P.G. Ferreira Parracho, M. Gallinaro, J. Seixas, J. Varela, P. Vischia

Joint Institute for Nuclear Research, Dubna, Russia

I. Belotelov, P. Bunin, I. Golutvin, V. Karjavin, V. Konoplyanikov, G. Kozlov, A. Lanev, A. Malakhov, P. Moisenz, V. Palichik, V. Perelygin, M. Savina, S. Shmatov, S. Shulha, V. Smirnov, A. Volodko, A. Zarubin

Petersburg Nuclear Physics Institute, Gatchina (St. Petersburg), Russia

S. Evstyukhin, V. Golovtsov, Y. Ivanov, V. Kim, P. Levchenko, V. Murzin, V. Oreshkin, I. Smirnov, V. Sulimov, L. Uvarov, S. Vavilov, A. Vorobyev, An. Vorobyev

Institute for Nuclear Research, Moscow, Russia

Yu. Andreev, A. Dermenev, S. Gninenko, N. Golubev, M. Kirsanov, N. Krasnikov, V. Matveev, A. Pashenkov, D. Tlisov, A. Toropin

Institute for Theoretical and Experimental Physics, Moscow, Russia

V. Epshteyn, M. Erofeeva, V. Gavrilo, M. Kossov, N. Lychkovskaya, V. Popov, G. Safronov, S. Semenov, V. Stolin, E. Vlasov, A. Zhokin

Moscow State University, Moscow, Russia

A. Belyaev, E. Boos, M. Dubinin³, L. Dudko, A. Ershov, A. Gribushin, V. Klyukhin, O. Kodolova, I. Lokhtin, A. Markina, S. Obraztsov, M. Perfilov, S. Petrushanko, A. Popov, L. Sarycheva[†], V. Savrin, A. Snigirev

P.N. Lebedev Physical Institute, Moscow, Russia

V. Andreev, M. Azarkin, I. Dremin, M. Kirakosyan, A. Leonidov, G. Mesyats, S.V. Rusakov, A. Vinogradov

State Research Center of Russian Federation, Institute for High Energy Physics, Protvino, Russia

I. Azhgirey, I. Bayshev, S. Bitioukov, V. Grishin⁴, V. Kachanov, D. Konstantinov, V. Krychkin, V. Petrov, R. Ryutin, A. Sobol, L. Tourtchanovitch, S. Troshin, N. Tyurin, A. Uzunian, A. Volkov

University of Belgrade, Faculty of Physics and Vinca Institute of Nuclear Sciences, Belgrade, Serbia

P. Adzic²⁹, M. Djordjevic, M. Ekmedzic, D. Krpic²⁹, J. Milosevic

Centro de Investigaciones Energéticas Medioambientales y Tecnológicas (CIEMAT), Madrid, Spain

M. Aguilar-Benitez, J. Alcaraz Maestre, P. Arce, C. Battilana, E. Calvo, M. Cerrada, M. Chamizo Llatas, N. Colino, B. De La Cruz, A. Delgado Peris, D. Domínguez Vázquez, C. Fernandez

Bedoya, J.P. Fernández Ramos, A. Ferrando, J. Flix, M.C. Fouz, P. Garcia-Abia, O. Gonzalez Lopez, S. Goy Lopez, J.M. Hernandez, M.I. Josa, G. Merino, J. Puerta Pelayo, A. Quintario Olmeda, I. Redondo, L. Romero, J. Santaolalla, M.S. Soares, C. Willmott

Universidad Autónoma de Madrid, Madrid, Spain

C. Albajar, G. Codispoti, J.F. de Trocóniz

Universidad de Oviedo, Oviedo, Spain

H. Brun, J. Cuevas, J. Fernandez Menendez, S. Folgueras, I. Gonzalez Caballero, L. Lloret Iglesias, J. Piedra Gomez

Instituto de Física de Cantabria (IFCA), CSIC-Universidad de Cantabria, Santander, Spain

J.A. Brochero Cifuentes, I.J. Cabrillo, A. Calderon, S.H. Chuang, J. Duarte Campderros, M. Felcini³⁰, M. Fernandez, G. Gomez, J. Gonzalez Sanchez, A. Graziano, C. Jorda, A. Lopez Virto, J. Marco, R. Marco, C. Martinez Rivero, F. Matorras, F.J. Munoz Sanchez, T. Rodrigo, A.Y. Rodríguez-Marrero, A. Ruiz-Jimeno, L. Scodellaro, I. Vila, R. Vilar Cortabitarte

CERN, European Organization for Nuclear Research, Geneva, Switzerland

D. Abbaneo, E. Auffray, G. Auzinger, M. Bachtis, P. Baillon, A.H. Ball, D. Barney, J.F. Benitez, C. Bernet⁵, G. Bianchi, P. Bloch, A. Bocci, A. Bonato, C. Botta, H. Breuker, T. Camporesi, G. Cerminara, T. Christiansen, J.A. Coarasa Perez, D. D'Enterria, A. Dabrowski, A. De Roeck, S. Di Guida, M. Dobson, N. Dupont-Sagorin, A. Elliott-Peisert, B. Frisch, W. Funk, G. Georgiou, M. Giffels, D. Gigi, K. Gill, D. Giordano, M. Girone, M. Giunta, F. Glege, R. Gomez-Reino Garrido, P. Govoni, S. Gowdy, R. Guida, M. Hansen, P. Harris, C. Hartl, J. Harvey, B. Hegner, A. Hinzmann, V. Innocente, P. Janot, K. Kaadze, E. Karavakis, K. Kousouris, P. Lecoq, Y.-J. Lee, P. Lenzi, C. Lourenço, N. Magini, T. Mäki, M. Malberti, L. Malgeri, M. Mannelli, L. Masetti, F. Meijers, S. Mersi, E. Meschi, R. Moser, M.U. Mozer, M. Mulders, P. Musella, E. Nesvold, T. Orimoto, L. Orsini, E. Palencia Cortezon, E. Perez, L. Perrozzi, A. Petrilli, A. Pfeiffer, M. Pierini, M. Pimiä, D. Piparo, G. Polese, L. Quertenmont, A. Racz, W. Reece, J. Rodrigues Antunes, G. Rolandi³¹, C. Rovelli³², M. Rovere, H. Sakulin, F. Santanastasio, C. Schäfer, C. Schwick, I. Segoni, S. Sekmen, A. Sharma, P. Siegrist, P. Silva, M. Simon, P. Sphicas³³, D. Spiga, A. Tsiros, G.I. Veres¹⁹, J.R. Vlimant, H.K. Wöhri, S.D. Worm³⁴, W.D. Zeuner

Paul Scherrer Institut, Villigen, Switzerland

W. Bertl, K. Deiters, W. Erdmann, K. Gabathuler, R. Horisberger, Q. Ingram, H.C. Kaestli, S. König, D. Kotlinski, U. Langenegger, F. Meier, D. Renker, T. Rohe

Institute for Particle Physics, ETH Zurich, Zurich, Switzerland

L. Bäni, P. Bortignon, M.A. Buchmann, B. Casal, N. Chanon, A. Deisher, G. Dissertori, M. Dittmar, M. Donegà, M. Dünser, J. Eugster, K. Freudenreich, C. Grab, D. Hits, P. Lecomte, W. Lustermann, A.C. Marini, P. Martinez Ruiz del Arbol, N. Mohr, F. Moortgat, C. Nägeli³⁵, P. Nef, F. Nessi-Tedaldi, F. Pandolfi, L. Pape, F. Pauss, M. Peruzzi, F.J. Ronga, M. Rossini, L. Sala, A.K. Sanchez, A. Starodumov³⁶, B. Stieger, M. Takahashi, L. Tauscher[†], A. Thea, K. Theofilatos, D. Treille, C. Urscheler, R. Wallny, H.A. Weber, L. Wehrli

Universität Zürich, Zurich, Switzerland

C. Amsler³⁷, V. Chiochia, S. De Visscher, C. Favaro, M. Ivova Rikova, B. Millan Mejias, P. Otiougova, P. Robmann, H. Snoek, S. Tuppen, M. Verzetti

National Central University, Chung-Li, Taiwan

Y.H. Chang, K.H. Chen, C.M. Kuo, S.W. Li, W. Lin, Z.K. Liu, Y.J. Lu, D. Mekterovic, A.P. Singh, R. Volpe, S.S. Yu

National Taiwan University (NTU), Taipei, Taiwan

P. Bartalini, P. Chang, Y.H. Chang, Y.W. Chang, Y. Chao, K.F. Chen, C. Dietz, U. Grundler, W.-S. Hou, Y. Hsiung, K.Y. Kao, Y.J. Lei, R.-S. Lu, D. Majumder, E. Petrakou, X. Shi, J.G. Shiu, Y.M. Tzeng, X. Wan, M. Wang

Chulalongkorn University, Bangkok, Thailand

B. Asavapibhop, N. Srimanobhas

Cukurova University, Adana, Turkey

A. Adiguzel, M.N. Bakirci³⁸, S. Cerci³⁹, C. Dozen, I. Dumanoglu, E. Eskut, S. Girgis, G. Gokbulut, E. Gurpinar, I. Hos, E.E. Kangal, T. Karaman, G. Karapinar⁴⁰, A. Kayis Topaksu, G. Onengut, K. Ozdemir, S. Ozturk⁴¹, A. Polatoz, K. Sogut⁴², D. Sunar Cerci³⁹, B. Tali³⁹, H. Topakli³⁸, L.N. Vergili, M. Vergili

Middle East Technical University, Physics Department, Ankara, Turkey

I.V. Akin, T. Aliev, B. Bilin, S. Bilmis, M. Deniz, H. Gamsizkan, A.M. Guler, K. Ocalan, A. Ozpineci, M. Serin, R. Sever, U.E. Surat, M. Yalvac, E. Yildirim, M. Zeyrek

Bogazici University, Istanbul, Turkey

E. Gülmez, B. Isildak⁴³, M. Kaya⁴⁴, O. Kaya⁴⁴, S. Ozkorucuklu⁴⁵, N. Sonmez⁴⁶

Istanbul Technical University, Istanbul, Turkey

K. Cankocak

National Scientific Center, Kharkov Institute of Physics and Technology, Kharkov, Ukraine

L. Levchuk

University of Bristol, Bristol, United Kingdom

J.J. Brooke, E. Clement, D. Cussans, H. Flacher, R. Frazier, J. Goldstein, M. Grimes, G.P. Heath, H.F. Heath, L. Kreczko, S. Metson, D.M. Newbold³⁴, K. Nirunpong, A. Poll, S. Senkin, V.J. Smith, T. Williams

Rutherford Appleton Laboratory, Didcot, United Kingdom

L. Basso⁴⁷, K.W. Bell, A. Belyaev⁴⁷, C. Brew, R.M. Brown, D.J.A. Cockerill, J.A. Coughlan, K. Harder, S. Harper, J. Jackson, B.W. Kennedy, E. Olaiya, D. Petyt, B.C. Radburn-Smith, C.H. Shepherd-Themistocleous, I.R. Tomalin, W.J. Womersley

Imperial College, London, United Kingdom

R. Bainbridge, G. Ball, R. Beuselinck, O. Buchmuller, D. Colling, N. Cripps, M. Cutajar, P. Dauncey, G. Davies, M. Della Negra, W. Ferguson, J. Fulcher, D. Futyan, A. Gilbert, A. Guneratne Bryer, G. Hall, Z. Hatherell, J. Hays, G. Iles, M. Jarvis, G. Karapostoli, L. Lyons, A.-M. Magnan, J. Marrouche, B. Mathias, R. Nandi, J. Nash, A. Nikitenko³⁶, A. Papageorgiou, J. Pela, M. Pesaresi, K. Petridis, M. Pioppi⁴⁸, D.M. Raymond, S. Rogerson, A. Rose, M.J. Ryan, C. Seez, P. Sharp[†], A. Sparrow, M. Stoye, A. Tapper, M. Vazquez Acosta, T. Virdee, S. Wakefield, N. Wardle, T. Whyntie

Brunel University, Uxbridge, United Kingdom

M. Chadwick, J.E. Cole, P.R. Hobson, A. Khan, P. Kyberd, D. Leggat, D. Leslie, W. Martin, I.D. Reid, P. Symonds, L. Teodorescu, M. Turner

Baylor University, Waco, USA

K. Hatakeyama, H. Liu, T. Scarborough

The University of Alabama, Tuscaloosa, USA

O. Charaf, C. Henderson, P. Rumerio

Boston University, Boston, USA

A. Avetisyan, T. Bose, C. Fantasia, A. Heister, J. St. John, P. Lawson, D. Lazic, J. Rohlf, D. Sperka, L. Sulak

Brown University, Providence, USA

J. Alimena, S. Bhattacharya, D. Cutts, Z. Demiragli, A. Ferapontov, A. Garabedian, U. Heintz, S. Jabeen, G. Kukartsev, E. Laird, G. Landsberg, M. Luk, M. Narain, D. Nguyen, M. Segala, T. Sinthuprasith, T. Speer, K.V. Tsang

University of California, Davis, Davis, USA

R. Breedon, G. Breto, M. Calderon De La Barca Sanchez, S. Chauhan, M. Chertok, J. Conway, R. Conway, P.T. Cox, J. Dolen, R. Erbacher, M. Gardner, R. Houtz, W. Ko, A. Kopecky, R. Lander, O. Mall, T. Miceli, D. Pellett, F. Ricci-Tam, B. Rutherford, M. Searle, J. Smith, M. Squires, M. Tripathi, R. Vasquez Sierra, R. Yohay

University of California, Los Angeles, USA

V. Andreev, D. Cline, R. Cousins, J. Duris, S. Erhan, P. Everaerts, C. Farrell, J. Hauser, M. Ignatenko, C. Jarvis, C. Plager, G. Rakness, P. Schlein[†], P. Traczyk, V. Valuev, M. Weber

University of California, Riverside, Riverside, USA

J. Babb, R. Clare, M.E. Dinardo, J. Ellison, J.W. Gary, F. Giordano, G. Hanson, G.Y. Jeng⁴⁹, H. Liu, O.R. Long, A. Luthra, H. Nguyen, S. Paramesvaran, J. Sturdy, S. Sumowidagdo, R. Wilken, S. Wimpenny

University of California, San Diego, La Jolla, USA

W. Andrews, J.G. Branson, G.B. Cerati, S. Cittolin, D. Evans, F. Golf, A. Holzner, R. Kelley, M. Lebourgeois, J. Letts, I. Macneill, B. Mangano, S. Padhi, C. Palmer, G. Petrucciani, M. Pieri, M. Sani, V. Sharma, S. Simon, E. Sudano, M. Tadel, Y. Tu, A. Vartak, S. Wasserbaech⁵⁰, F. Würthwein, A. Yagil, J. Yoo

University of California, Santa Barbara, Santa Barbara, USA

D. Barge, R. Bellan, C. Campagnari, M. D'Alfonso, T. Danielson, K. Flowers, P. Geffert, J. Incandela, C. Justus, P. Kalavase, S.A. Koay, D. Kovalskyi, V. Krutelyov, S. Lowette, N. Mccoll, V. Pavlunin, F. Rebassoo, J. Ribnik, J. Richman, R. Rossin, D. Stuart, W. To, C. West

California Institute of Technology, Pasadena, USA

A. Apresyan, A. Bornheim, Y. Chen, E. Di Marco, J. Duarte, M. Gataullin, Y. Ma, A. Mott, H.B. Newman, C. Rogan, M. Spiropulu, V. Timciuc, J. Veverka, R. Wilkinson, S. Xie, Y. Yang, R.Y. Zhu

Carnegie Mellon University, Pittsburgh, USA

B. Akgun, V. Azzolini, A. Calamba, R. Carroll, T. Ferguson, Y. Iiyama, D.W. Jang, Y.F. Liu, M. Paulini, H. Vogel, I. Vorobiev

University of Colorado at Boulder, Boulder, USA

J.P. Cumalat, B.R. Drell, W.T. Ford, A. Gaz, E. Luiggi Lopez, J.G. Smith, K. Stenson, K.A. Ulmer, S.R. Wagner

Cornell University, Ithaca, USA

J. Alexander, A. Chatterjee, N. Eggert, L.K. Gibbons, B. Heltsley, A. Khukhunaishvili, B. Kreis, N. Mirman, G. Nicolas Kaufman, J.R. Patterson, A. Ryd, E. Salvati, W. Sun, W.D. Teo, J. Thom, J. Thompson, J. Tucker, J. Vaughan, Y. Weng, L. Winstrom, P. Wittich

Fairfield University, Fairfield, USA

D. Winn

Fermi National Accelerator Laboratory, Batavia, USA

S. Abdullin, M. Albrow, J. Anderson, L.A.T. Bauerdick, A. Beretvas, J. Berryhill, P.C. Bhat, I. Bloch, K. Burkett, J.N. Butler, V. Chetluru, H.W.K. Cheung, F. Chlebana, V.D. Elvira, I. Fisk, J. Freeman, Y. Gao, D. Green, O. Gutsche, J. Hanlon, R.M. Harris, J. Hirschauer, B. Hooberman, S. Jindariani, M. Johnson, U. Joshi, B. Kilminster, B. Klima, S. Kunori, S. Kwan, C. Leonidopoulos, J. Linacre, D. Lincoln, R. Lipton, J. Lykken, K. Maeshima, J.M. Marraffino, S. Maruyama, D. Mason, P. McBride, K. Mishra, S. Mrenna, Y. Musienko⁵¹, C. Newman-Holmes, V. O'Dell, O. Prokofyev, E. Sexton-Kennedy, S. Sharma, W.J. Spalding, L. Spiegel, L. Taylor, S. Tkaczyk, N.V. Tran, L. Uplegger, E.W. Vaandering, R. Vidal, J. Whitmore, W. Wu, F. Yang, F. Yumiceva, J.C. Yun

University of Florida, Gainesville, USA

D. Acosta, P. Avery, D. Bourilkov, M. Chen, T. Cheng, S. Das, M. De Gruttola, G.P. Di Giovanni, D. Dobur, A. Drozdetskiy, R.D. Field, M. Fisher, Y. Fu, I.K. Furic, J. Gartner, J. Hugon, B. Kim, J. Konigsberg, A. Korytov, A. Kropivnitskaya, T. Kypreos, J.F. Low, K. Matchev, P. Milenovic⁵², G. Mitselmakher, L. Muniz, M. Park, R. Remington, A. Rinkevicius, P. Sellers, N. Skhirtladze, M. Snowball, J. Yelton, M. Zakaria

Florida International University, Miami, USA

V. Gaultney, S. Hewamanage, L.M. Lebolo, S. Linn, P. Markowitz, G. Martinez, J.L. Rodriguez

Florida State University, Tallahassee, USA

T. Adams, A. Askew, J. Bochenek, J. Chen, B. Diamond, S.V. Gleyzer, J. Haas, S. Hagopian, V. Hagopian, M. Jenkins, K.F. Johnson, H. Prosper, V. Veeraraghavan, M. Weinberg

Florida Institute of Technology, Melbourne, USA

M.M. Baarmand, B. Dorney, M. Hohlmann, H. Kalakhety, I. Vodopiyarov

University of Illinois at Chicago (UIC), Chicago, USA

M.R. Adams, I.M. Anghel, L. Apanasevich, Y. Bai, V.E. Bazterra, R.R. Betts, I. Bucinskaite, J. Callner, R. Cavanaugh, O. Evdokimov, L. Gauthier, C.E. Gerber, D.J. Hofman, S. Khalatyan, F. Lacroix, M. Malek, C. O'Brien, C. Silkworth, D. Strom, P. Turner, N. Varelas

The University of Iowa, Iowa City, USA

U. Akgun, E.A. Albayrak, B. Bilki⁵³, W. Clarida, F. Duru, J.-P. Merlo, H. Mermerkaya⁵⁴, A. Mestvirishvili, A. Moeller, J. Nachtman, C.R. Newsom, E. Norbeck, Y. Onel, F. Ozok⁵⁵, S. Sen, P. Tan, E. Tiras, J. Wetzel, T. Yetkin, K. Yi

Johns Hopkins University, Baltimore, USA

B.A. Barnett, B. Blumenfeld, S. Bolognesi, D. Fehling, G. Giurgiu, A.V. Gritsan, Z.J. Guo, G. Hu, P. Maksimovic, S. Rappoccio, M. Swartz, A. Whitbeck

The University of Kansas, Lawrence, USA

P. Baringer, A. Bean, G. Benelli, R.P. Kenny Iii, M. Murray, D. Noonan, S. Sanders, R. Stringer, G. Tinti, J.S. Wood, V. Zhukova

Kansas State University, Manhattan, USA

A.F. Barfuss, T. Bolton, I. Chakaberia, A. Ivanov, S. Khalil, M. Makouski, Y. Maravin, S. Shrestha, I. Svintradze

Lawrence Livermore National Laboratory, Livermore, USA

J. Gronberg, D. Lange, D. Wright

University of Maryland, College Park, USA

A. Baden, M. Boutemeur, B. Calvert, S.C. Eno, J.A. Gomez, N.J. Hadley, R.G. Kellogg, M. Kirn,

T. Kolberg, Y. Lu, M. Marionneau, A.C. Mignerey, K. Pedro, A. Skuja, J. Temple, M.B. Tonjes, S.C. Tonwar, E. Twedt

Massachusetts Institute of Technology, Cambridge, USA

A. Apyan, G. Bauer, J. Bendavid, W. Busza, E. Butz, I.A. Cali, M. Chan, V. Dutta, G. Gomez Ceballos, M. Goncharov, K.A. Hahn, Y. Kim, M. Klute, K. Krajczar⁵⁶, P.D. Luckey, T. Ma, S. Nahn, C. Paus, D. Ralph, C. Roland, G. Roland, M. Rudolph, G.S.F. Stephans, F. Stöckli, K. Sumorok, K. Sung, D. Velicanu, E.A. Wenger, R. Wolf, B. Wyslouch, M. Yang, Y. Yilmaz, A.S. Yoon, M. Zanetti

University of Minnesota, Minneapolis, USA

S.I. Cooper, B. Dahmes, A. De Benedetti, G. Franzoni, A. Gude, S.C. Kao, K. Klapoetke, Y. Kubota, J. Mans, N. Pastika, R. Rusack, M. Sasseville, A. Singovsky, N. Tambe, J. Turkewitz

University of Mississippi, Oxford, USA

L.M. Cremaldi, R. Kroeger, L. Perera, R. Rahmat, D.A. Sanders

University of Nebraska-Lincoln, Lincoln, USA

E. Avdeeva, K. Bloom, S. Bose, D.R. Claes, A. Dominguez, M. Eads, J. Keller, I. Kravchenko, J. Lazo-Flores, H. Malbouisson, S. Malik, G.R. Snow

State University of New York at Buffalo, Buffalo, USA

A. Godshalk, I. Iashvili, S. Jain, A. Kharchilava, A. Kumar

Northeastern University, Boston, USA

G. Alverson, E. Barberis, D. Baumgartel, M. Chasco, J. Haley, D. Nash, D. Trocino, D. Wood, J. Zhang

Northwestern University, Evanston, USA

A. Anastassov, A. Kubik, L. Lusito, N. Mucia, N. Odell, R.A. Ofierzynski, B. Pollack, A. Pozdnyakov, M. Schmitt, S. Stoynev, M. Velasco, S. Won

University of Notre Dame, Notre Dame, USA

L. Antonelli, D. Berry, A. Brinkerhoff, K.M. Chan, M. Hildreth, C. Jessop, D.J. Karmgard, J. Kolb, K. Lannon, W. Luo, S. Lynch, N. Marinelli, D.M. Morse, T. Pearson, M. Planer, R. Ruchti, J. Slaunwhite, N. Valls, M. Wayne, M. Wolf

The Ohio State University, Columbus, USA

B. Bylsma, L.S. Durkin, C. Hill, R. Hughes, K. Kotov, T.Y. Ling, D. Puigh, M. Rodenburg, C. Vuosalo, G. Williams, B.L. Winer

Princeton University, Princeton, USA

N. Adam, E. Berry, P. Elmer, D. Gerbaudo, V. Halyo, P. Hebda, J. Hegeman, A. Hunt, P. Jindal, D. Lopes Pegna, P. Lujan, D. Marlow, T. Medvedeva, M. Mooney, J. Olsen, P. Piroué, X. Quan, A. Raval, B. Safdi, H. Saka, D. Stickland, C. Tully, J.S. Werner, A. Zuranski

University of Puerto Rico, Mayaguez, USA

E. Brownson, A. Lopez, H. Mendez, J.E. Ramirez Vargas

Purdue University, West Lafayette, USA

E. Alagoz, V.E. Barnes, D. Benedetti, G. Bolla, D. Bortoletto, M. De Mattia, A. Everett, Z. Hu, M. Jones, O. Koybasi, M. Kress, A.T. Laasanen, N. Leonardo, V. Maroussov, P. Merkel, D.H. Miller, N. Neumeister, I. Shipsey, D. Silvers, A. Svyatkovskiy, M. Vidal Marono, H.D. Yoo, J. Zablocki, Y. Zheng

Purdue University Calumet, Hammond, USA

S. Guragain, N. Parashar

Rice University, Houston, USA

A. Adair, C. Boulahouache, K.M. Ecklund, F.J.M. Geurts, W. Li, B.P. Padley, R. Redjimi, J. Roberts, J. Zabel

University of Rochester, Rochester, USA

B. Betchart, A. Bodek, Y.S. Chung, R. Covarelli, P. de Barbaro, R. Demina, Y. Eshaq, T. Ferbel, A. Garcia-Bellido, P. Goldenzweig, J. Han, A. Harel, D.C. Miner, D. Vishnevskiy, M. Zielinski

The Rockefeller University, New York, USA

A. Bhatti, R. Ciesielski, L. Demortier, K. Goulios, G. Lungu, S. Malik, C. Mesropian

Rutgers, the State University of New Jersey, Piscataway, USA

S. Arora, A. Barker, J.P. Chou, C. Contreras-Campana, E. Contreras-Campana, D. Duggan, D. Ferencek, Y. Gershtein, R. Gray, E. Halkiadakis, D. Hidas, A. Lath, S. Panwalkar, M. Park, R. Patel, V. Rekovic, J. Robles, K. Rose, S. Salur, S. Schnetzer, C. Seitz, S. Somalwar, R. Stone, S. Thomas, M. Walker

University of Tennessee, Knoxville, USA

G. Cerizza, M. Hollingsworth, S. Spanier, Z.C. Yang, A. York

Texas A&M University, College Station, USA

R. Eusebi, W. Flanagan, J. Gilmore, T. Kamon⁵⁷, V. Khotilovich, R. Montalvo, I. Osipenkov, Y. Pakhotin, A. Perloff, J. Roe, A. Safonov, T. Sakuma, S. Sengupta, I. Suarez, A. Tatarinov, D. Toback

Texas Tech University, Lubbock, USA

N. Akchurin, J. Damgov, C. Dragoiu, P.R. Duderu, C. Jeong, K. Kovitanggoon, S.W. Lee, T. Libeiro, Y. Roh, I. Volobouev

Vanderbilt University, Nashville, USA

E. Appelt, A.G. Delannoy, C. Florez, S. Greene, A. Gurrola, W. Johns, P. Kurt, C. Maguire, A. Melo, M. Sharma, P. Sheldon, B. Snook, S. Tuo, J. Velkovska

University of Virginia, Charlottesville, USA

M.W. Arenton, M. Balazs, S. Boutle, B. Cox, B. Francis, J. Goodell, R. Hirosky, A. Ledovskoy, C. Lin, C. Neu, J. Wood

Wayne State University, Detroit, USA

S. Gollapinni, R. Harr, P.E. Karchin, C. Kottachchi Kankanamge Don, P. Lamichhane, A. Sakharov

University of Wisconsin, Madison, USA

M. Anderson, D.A. Belknap, L. Borrello, D. Carlsmith, M. Cepeda, S. Dasu, E. Friis, L. Gray, K.S. Grogg, M. Grothe, R. Hall-Wilton, M. Herndon, A. Hervé, P. Klabbers, J. Klukas, A. Lanaro, C. Lazaridis, J. Leonard, R. Loveless, A. Mohapatra, I. Ojalvo, F. Palmonari, G.A. Pierro, I. Ross, A. Savin, W.H. Smith, J. Swanson

†: Deceased

1: Also at Vienna University of Technology, Vienna, Austria

2: Also at National Institute of Chemical Physics and Biophysics, Tallinn, Estonia

3: Also at California Institute of Technology, Pasadena, USA

4: Also at CERN, European Organization for Nuclear Research, Geneva, Switzerland

- 5: Also at Laboratoire Leprince-Ringuet, Ecole Polytechnique, IN2P3-CNRS, Palaiseau, France
- 6: Also at Suez Canal University, Suez, Egypt
- 7: Also at Zewail City of Science and Technology, Zewail, Egypt
- 8: Also at Cairo University, Cairo, Egypt
- 9: Also at Fayoum University, El-Fayoum, Egypt
- 10: Also at British University in Egypt, Cairo, Egypt
- 11: Now at Ain Shams University, Cairo, Egypt
- 12: Also at National Centre for Nuclear Research, Swierk, Poland
- 13: Also at Université de Haute-Alsace, Mulhouse, France
- 14: Also at Joint Institute for Nuclear Research, Dubna, Russia
- 15: Also at Moscow State University, Moscow, Russia
- 16: Also at Brandenburg University of Technology, Cottbus, Germany
- 17: Also at The University of Kansas, Lawrence, USA
- 18: Also at Institute of Nuclear Research ATOMKI, Debrecen, Hungary
- 19: Also at Eötvös Loránd University, Budapest, Hungary
- 20: Also at Tata Institute of Fundamental Research - HECR, Mumbai, India
- 21: Also at University of Visva-Bharati, Santiniketan, India
- 22: Also at Sharif University of Technology, Tehran, Iran
- 23: Also at Isfahan University of Technology, Isfahan, Iran
- 24: Also at Plasma Physics Research Center, Science and Research Branch, Islamic Azad University, Tehran, Iran
- 25: Also at Facoltà Ingegneria, Università di Roma, Roma, Italy
- 26: Also at Università degli Studi Guglielmo Marconi, Roma, Italy
- 27: Also at Università degli Studi di Siena, Siena, Italy
- 28: Also at University of Bucharest, Faculty of Physics, Bucuresti-Magurele, Romania
- 29: Also at Faculty of Physics of University of Belgrade, Belgrade, Serbia
- 30: Also at University of California, Los Angeles, USA
- 31: Also at Scuola Normale e Sezione dell'INFN, Pisa, Italy
- 32: Also at INFN Sezione di Roma; Università di Roma, Roma, Italy
- 33: Also at University of Athens, Athens, Greece
- 34: Also at Rutherford Appleton Laboratory, Didcot, United Kingdom
- 35: Also at Paul Scherrer Institut, Villigen, Switzerland
- 36: Also at Institute for Theoretical and Experimental Physics, Moscow, Russia
- 37: Also at Albert Einstein Center for Fundamental Physics, Bern, Switzerland
- 38: Also at Gaziosmanpasa University, Tokat, Turkey
- 39: Also at Adiyaman University, Adiyaman, Turkey
- 40: Also at Izmir Institute of Technology, Izmir, Turkey
- 41: Also at The University of Iowa, Iowa City, USA
- 42: Also at Mersin University, Mersin, Turkey
- 43: Also at Ozyegin University, Istanbul, Turkey
- 44: Also at Kafkas University, Kars, Turkey
- 45: Also at Suleyman Demirel University, Isparta, Turkey
- 46: Also at Ege University, Izmir, Turkey
- 47: Also at School of Physics and Astronomy, University of Southampton, Southampton, United Kingdom
- 48: Also at INFN Sezione di Perugia; Università di Perugia, Perugia, Italy
- 49: Also at University of Sydney, Sydney, Australia
- 50: Also at Utah Valley University, Orem, USA
- 51: Also at Institute for Nuclear Research, Moscow, Russia

52: Also at University of Belgrade, Faculty of Physics and Vinca Institute of Nuclear Sciences, Belgrade, Serbia

53: Also at Argonne National Laboratory, Argonne, USA

54: Also at Erzincan University, Erzincan, Turkey

55: Also at Mimar Sinan University, Istanbul, Istanbul, Turkey

56: Also at KFKI Research Institute for Particle and Nuclear Physics, Budapest, Hungary

57: Also at Kyungpook National University, Daegu, Korea